HAWASSA UNIVERSITY

SCHOOL OF POSTGRAGUATE STUDIES

COLLEGE OF NATURAL AND COMPUTATIONAL SCIENCES

DEPARTMENT OF CHEMISTRY

BIOSYNTHESIZED NITROGEN-ZINC-CODOPED COPPER OXIDE NANOPARTICLES FOR PHOTOCATALYTIC DEGRADATION OF METHYLENE BLUE

MSc THESIS

BY:

YOHANNES SHUKA JARA

ADVISOR: Dr. ENDALE TSEGAYE (PhD)

JUNE, 2024

HAWASSA, ETHIOPIA

BIOSYNTHESIZED NITROGEN-ZINC-CODOPED COPPER OXIDE NANOPARTICLES FOR PHOTOCATALYTIC DEGRADATION OF METHYLENE BLUE

BY

YOHANNES SHUKA JARA

ADVISOR: Dr. ENDALE TSEGAYE (PhD)

A THESIS SUBMITTED TO THE DEPARTMENT OF CHEMISTRY, COLLEGE OF NATURAL AND COMPUTATIONAL SCIENCES, SCHOOL OF GRADUATE STUDIES OF THE HAWASSA UNIVERSITY IN PARTIAL FULFILLMENT OF THE REQUIREMENTS FOR THE DEGREE OF MASTER OF SCIENCE IN PHYSICAL CHEMISTRY

JUNE, 2024

HAWASSA, ETHIOPIA

DECLARATION

I hereby declare that this MSc Thesis entitled "**Biosynthesized Nitrogen-Zinc-Codoped Copper Oxide Nanoparticles for Photocatalytic Degradation of Methylene Blue**" is my original work. I have followed all ethical principles of scholarship in the preparation, data collection, data analysis and completion of this thesis. All scholarly matter that is included in the thesis has been given recognition through citation. I affirm that I have cited and referenced all sources used in this document. This thesis is submitted in partial fulfilment of the requirement for a master degree of science in Physical Chemistry from the School of Postgraduate Studies of Hawassa University. The thesis is deposited in the Hawassa University Library and is made available to borrowers under the rules of the library. I solemnly declare that this thesis has not been submitted to any other institution anywhere for the award of any academic degree, diploma or certificate.

YOHANNES SHUKA JARA _____ _____

Student Name Signature Date

This MSc thesis has been submitted for examination with my approval as thesis advisor.

Dr. Endale Tsegaye (PhD) _____ _____

Advisor Name Signature Date

ADVISORS' APPROVAL SHEET

SCHOOL OF GRADUATE STUDIES

HAWASSA UNIVERSITY

This is to certify that the thesis entitled **"Biosynthesized Nitrogen-Zinc-Codoped Copper Oxide Nanoparticles for Photocatalytic Degradation of Methylene Blue"** submitted in partial fulfilment of the requirements for the degree of Master's with specialization in Physical Chemistry, the Graduate Program of the Chemistry Department/School of Natural and Computational Sciences, and has been carried out by **YOHANNES SHUKA**, ID No; **GPChmR/0009/15**, under my supervision. I have read and evaluated this thesis, which is complies with the regulations of the university and meets the required standards with respect to originality and quality. Therefore I recommend that the student has fulfilled the requirements and hence hereby can submit the thesis to the department with my approval as a university advisor.

Dr. Endale Tsegaye (PhD)	_____	_____
Advisor Name	Signature	Date

EXAMINERS' APPROVAL SHEET

SCHOOL OF POSTGRAGUATE STUDIES

HAWASSA UNIVERSITY

We, the undersigned, members of the Board of Examiners of the final Thesis open defense by **YOHANNES SHUKA** have read and evaluated his thesis entitled **"Biosynthesized Nitrogen-Zinc-Codoped Copper Oxide Nanoparticles for Photocatalytic Degradation of Methylene Blue"** and examined the candidate. This is, therefore, to certify that the thesis has been accepted in partial fulfilment of the requirements for the Degree of Masters of Science in Physical Chemistry.

_____	_____	_____
Name of Advisor	Signature	Date
_____	_____	_____
Name of Chairperson	Signature	Date
_____	_____	_____
Name of Internal examiner	Signature	Date
_____	_____	_____
Name of External examiner	Signature	Date
_____	_____	_____
SGS Approval	Signature	Date

Signature Date Final approval and acceptance of the thesis is contingent upon the submission of the final copy of the thesis to the School of Graduate Studies (SGS) through the Department/School Graduate Committee (DGC/SGC) of the candidate's department.

Stamp of SGS Date: _____

ACKNOWLEDGEMENTS

Above all, I would like to thank my Almighty God for his Endless Love and Blessing me with all the treasures of wisdom and knowledge of LORD Christ Jesus, for his leadership and protections throughout not only in my academic journey but all my work.

I extend my heartfelt appreciation to my esteemed advisor, Dr. Endale Tsegaye (PhD), for his exceptional mentorship. His invaluable guidance, insightful advice, and unwavering support have been instrumental in the successful completion of this thesis. His approachability and patience have instilled in me the confidence to navigate the challenges of research and scholarship.

Special recognition goes to Prof. Sisay Tadesse (PhD), Dr. Adelaw Estifanos (PhD, Asso. Prof), and Mr. Teshome Abute (Asst. Prof) for their insightful teachings, guidance and the knowledge they have imparted upon me. Their expertise and dedication have greatly influenced my intellectual development and shaped my understanding of the field.

I am deeply indebted to Mr. Tilahun Tumiso, who is expert of spectroscopic instruments and lab analyst for unwavering support during lab session, and to my cherished friends Mr. Amanuel Abraham, Mr. Kifle Jilio, and Mr. Tesfaye Tariku, for their unwavering love and support. Their presence has made my campus life a truly unforgettable experience. Their encouragement and camaraderie have been a constant source of motivation and inspiration, propelling me forward even during the most challenging times.

I am eternally grateful to my family, special Mr. Zeleke Chutulo and Zinash Shuka, for their unwavering prayers, support, and encouragement. Their belief in me has been an inexhaustible source of strength and determination throughout my educational pursuits.

Finally, I extend my sincere gratitude to Madda Walabu University for providing me with the financial support to pursue my Master's degree in Physical Chemistry. Their investment in my education has made this achievement possible, and I am committed to using the knowledge and skills I have acquired to make a meaningful contribution to the field and to society as a whole.

DEDICATION

This thesis is dedicated to the memory of my beloved mother, Getare Sama, and my dear brother Pawulos Muluken, who are now at rest.

TABLE OF CONTENTS

TITLES **PAGE**

LIST OF TABLES

LIST OF FIGURES

LIST OF APPENDICES

LIST OF ACRONYMS AND ABBREVIATIONS

CuO NPs	Copper oxide nanoparticles
Cb	Conduction band
E_g	Energy band gap
FT-IR	Fourier Transforms Infrared Spectroscopy
JCPDS	Joint Committee for Powder X-ray Diffraction Standard
LMB	Leucomethyene blue
MB	Methylene blue
MNPs/MONPs	Metal or Metal oxide nanoparticles
MOFs	Metal organic frameworks
MOSC	Metal oxide semiconductor
N-CuO NPs	Nitrogen doped copper oxide nanoparticles
NPs	Nanoparticles
n-type	Negative type dopant (e^- donor)
N-Zn-CuO NPs	Nitrogen and Zinc codoped copper oxide nanoparticles
PA	*Pycnostachys abyssinica*
p-type	Positive type dopant (e^- acceptor)
ROS	Reactive Oxygen species
SEM	Scanning Electron Microscopy
SPR	Surface Plasmon Resonance
UV–Vis	Ultraviolet Visible Spectroscopy
Vb	Valance band
XRD	X-ray Diffraction Spectroscopy
Zn-CuO NPs	Zinc doped copper oxide

ABSTRACT

Herein, nitrogen-zinc-codoped copper nanoparticles (N-Zn-CuO NPs) was successfully synthesized by using Pycnostachys Abyssinica Fresen plant leaf extract as a bioreducing and capping agent for the photocatalytic degradation of methylene blue under natural sunlight irradiation. Additionally, pure CuO NPs, N-CuO NPs, and Zn-CuO NPs were also biosynthesized for comparison. Characterization techniques of UV-Vis, XRD, SEM, FT-IR revealed that N-Zn-codoping narrowed the band gap (1.72 to1.07 eV), reduced the crystallite size (25 to11.23 nm), distortion of monoclinic crystal lattice (rhombus and diamond like shape with an average diameter of 2.25 µm to irregular shape with an average size of 2.75 µm), and towards redshift of the Cu-O characteristic peaks (617 to 529 cm^{-1}) of CuO NPs, respectively, confirmed the successful incorporation of dopants into CuO NPs. The effects of key parameters on the photocatalytic degradation efficiency of all biosynthesised NPs were investigated. The optimal conditions with maximum degradation for N-Zn-CuO NPs were determined to be 3% dopant concentration for both N and Zn, 120 mg of photocatalyst dosage, pH of solution at 11, 20 ppm of Initial dye concentration and 30 minutes of reaction time. Photocatalytic activity towards methylene blue (MB) dye degradation under 30 minutes exposure to sunlight was 99.75% for N-Zn-CuO NPs, outperforming pure CuO NPs (95.76%), N-CuO NPs (97.93%), and Zn-CuO NPs (98.26%) under optimal conditions. The enhanced photocatalytic performance of N-Zn-CuO NPs is attributed to their tailored optical properties, leading to improved charge separation and reduced recombination. Kinetic studies revealed a strong fit (R^2=0.99799) with the BMG kinetic model for N-Zn-CuO NPs, indicating surface-mediated degradation of MB. Furthermore, the nanocatalysts exhibited excellent reusability and stability over four cycles. This finding highlights the potential of biosynthesized N-Zn-CuO NPs as highly efficient, simple, eco-friendly and sustainable solutions for the degradation organic pollutants.

***Keywords**: Biosynthesis, Doping and codoping, Methylene blue, N-Zn-codoped CuO NPs, Photocatalytic degradation, Pycnostachys Abyssinica*

CHAPTER ONE

INTRODUCTION

1.1. Background of the Study

One of the major challenges confronting the world today is the widespread pollution resulting from the rapid expansion of industrial and agricultural activities, which discharge a range of inorganic, organic, and organometallic pollutants. Persistent organic pollutants, particularly those associated with organic dyes, pose significant health and environmental risks [1, 2]. Despite their widespread use across multiple industries, such as textiles, cosmetics, leather tans, paper, pharmaceuticals, plastics, and educational laboratories. organic dyes are highly toxic to humans and other living organisms if not handled or disposed properly [3]. An estimated 15% of textile dyes are released into the environment as effluents, directly or indirectly impacting ecosystems [4]. Azo dyes, which constitute more than 50% of all industrial dyes produced globally, are particularly problematic. The azo groups (N = N-) responsible for their colouration are detectable in textile effluent at low concentrations and can cause mutagenic and carcinogenic effects [5]. These dyes have complex water constitutions, great chemical stability, and poor biodegradability [6].
Methylene blue (MB), an aromatic amine organic dye and reactive azo dye commonly used in textile coloring, is highly toxic to humans, terrestrial life, and aquatic life. Exposure can cause cyanosis, vomiting, eye irritation [2], confusion, nausea [7], increased heart rate, quadriplegia, shock, jaundice, tissue necrosis, and harm to aquatic ecosystems and marine vegetation [8]. Given the hazardous nature of organic dyes and their negative impact on photosynthetic activity, it is essential to remove them from wastewater before releasing them back into the natural environment. The innovating of sustainable methods for degrading dyes is a challenge for researchers and has received much attention [9].

Over the last three decades, various techniques have been employed to treat polluted air and aqueous systems, including adsorption, flocculation, chemical oxidation, coagulation, ozonolysis, ion exchange methods, and the use of metal and metal oxide nanoparticles (MONPs) and metal organic frameworks (MOFs) [10]. However, these methods have limitations such as incomplete pollutant removal, slow process rates, high energy and material consumption, high costs, and the production of secondary pollutants or large amounts of sludge that require further disposal. Nanoscience and nanotechnology have

explored several new applications in biomedical, material science, and environmental remediation due to the active surface phenomenon, enhanced surface area, morphology, catalytic activity, thermal and electrical conductivity, biological properties, and optical characteristics of MONPs compared to those of bulk materials [11]. Recently, the biogenic synthesis of MONPs for photocatalytic degradation using a semiconductor photocatalyst has gained significant attention for applications in environmental remediation due to its cost-effectiveness, simplicity, inability to generate secondary pollutants, and green approach for successfully degrading dyes [9, 12]. Unfortunately, commonly used photocatalysts (ZnO and TiO_2) exhibit good absorption in the UV region of solar light, which constitutes only 5% of the total radiation [13]. To increase the photoresponsiveness of photocatalysts to the visible region, researchers have adopted various strategies, such as doping with metal or nonmetal impurities, codoping, combining different metal oxides (composites), and sensitization [14]. Additional, choosing a metal oxide with short band gap like CuO is also effective strategy to enhance photocatalytic performance.

Among MONPs, CuO nanoparticles are p-type semiconductors with numerous applications due to their abundance, cost-effectiveness, stability, narrow band gap, and eco-friendliness [15]. CuO is widely used in supercapacitors [16], batteries [17], electrochemical corrosion inhibition [18], photocatalytic reactions, biological applications [19], and adsorption technology [20]. CuO is preferred over Cu_2O for photocatalytic applications due to its superior stability and lower band gap (1.7 eV), which can be tuned by suitable metal doping to utilize a wide range of visible radiation [1, 26]. The most effective approach is to dope suitable metal cations and nonmetal anions into the CuO lattice, which reduces the band gap and alters the electrical, optical, and structural properties of metal oxides.

Doping is one modification that enhances the photoresponsiveness of a photocatalyst to the visible region by creating new energy levels that reduce the band gap between the valence band and conduction band [13]. The incorporation of dopants, either metal ions or nonmetallic ions, into the MONP crystal lattice is an excellent method for increasing its photocatalytic activity [22]. Each type of dopant has a unique impact on the crystal lattice of the semiconductor. Metal dopants improve the morphology, surface area, photocatalytic performance, and electronic and magnetic properties of photocatalytic semiconductors. Nonmetal dopants can improve the photocatalytic utilization of solar energy, charge

separation efficiency, and recombination of the e−/h+ charge by hybridizing with a photocatalyst oxide or replacing the oxygen-deficient site in the photocatalyst oxide, which acts as a blocker for reoxidation [23]. Anionic doping involves nonmetals occupying anionic positions of oxygen. Nonmetallic elements (such as sulfur, nitrogen, and carbon) and anions (F^-, PO_4^{3-}, Cl^-, etc.) have lower electronegativity and atomic radii similar to those of oxygen atoms and have been successfully used as modifying agents for the photocatalytic activity of MONPs [16, 17].

Codoping is a promising strategy that can be used for effectively tuning dopant populations, electronic properties, and magnetic properties by increasing the valence band edge and lowering the conduction band edge [25]. The use of cation–anion codoping of carbon and molybdenum can significantly improve the photocatalytic activity in the visible range to approximately four times greater than that of materials doped with only one type of ion [26].

Researchers have evaluated the photocatalytic efficiency of CuO nanoparticles using various strategies, such as metal doping with Ni [21], Ce [1], Zn [27], NiO [28], Co [29], nonmetal doping with Cl [30], and S [23]; binary metal codoping with Ce-Zn [13], Ag-Zn [31], Ag-Mo [32], Ag-Ni [33]; metal-nonmetal codoping with Ag-Fe [34]; Composites such as rGO/ZnO/CuO [2] and ZnO/CuO [35] have been used as catalysts for energy, medical, and environmental applications via different physical and chemical synthesis methods, such as microwave-assisted sol-gel techniques [36], electrospinning-hydrothermal techniques [37], electrochemical deposition processes [38], coprecipitation methods [39], combustion methods [40], probe-sonicated/sonochemical methods [41], laser ablation methods [42], photoreduction methods, microplasma–liquid interactions, and ball milling methods [43]. However, these physiochemical methods have drawbacks. To overcome this problem, the green synthesis of CuO NPs using biological resources such as plants, bacteria, algae, and fungi has gained attention due to their easy availability, low cost, low toxicity, and capacity for large-scale synthesis of stable, controlled-sized and shaped NPs [9]. Plant extracts naturally act as reducing, stabilizing, and capping agents for the synthesis of NPs [3].

Pycnostachys abyssinica Fresen, commonly known as "Olomuwa" in the Wolaita language, is a medicinal plant native to Ethiopia and belongs to the Lamiaceae family

[44]. Recently reported work by literature [44], investigated the extract of the root of *Pycnostachys abyssinica* Fresen and revealed the presence of alkaloids, flavonoids, glycosides, phenols, terpenoids, tannins, steroids, and acidic compounds. Similarly, other studies by Dubale *et al.*, [45], and Getahun [46] have demonstrated the indigenous medicinal application and abundance of phytochemicals in the parts (leaf, root and steam) of *Pycnostachys Abyssinica* Fresen, which have shown potential as reducing and stabilizing agents for synthesizing semiconductors based on MONPs [47, 48]. Despite the recognized medicinal properties of *Pycnostachys abyssinica* Fresen, its pharmacological and environmental effects have not been fully explored. Hence, this study aims to promote the use of this plant for environmental applications by employing a green method to synthesize N-Zn-codoped nanoparticles.

1.2. Statement of the Problem

In today's world, the imbalanced growth of industrialization and waste management has caused widespread environmental pollution, posing a risk to the survival of life. Rapid urbanization and industrialization result in the release of more than a hundred tons of chemical pollutants daily, including inorganic, organic, organometallic compounds, and persistent organic dyes, often without proper treatment [4, 49]. Special, these pollutants are highly toxic to ecosystems [48], the risk is high in Africa developing countries due to inadequate waste management practices and the lack of economical technologies [50]. In fact, last two decades, researchers have designed and applied various strategies to develop sustainable methods, such as green synthesis of metal and metal oxide nanoparticles for the photocatalytic degradation of toxic pollutants for environmental remediation, offering an alternative to conventional methods [9, 10]. However, these methods are often limited in terms of photocatalytic degradation efficiency due to their insufficient meeting of the required physiochemical properties for the targeted application [13]. To overpass this limitation and explore the full potential of metal/metal oxide nanoparticles, semiconductor modification through various techniques such as doping and codoping has emerged as an innovative approach [51].

With this in mind, this study aimed to biosynthesize a highly efficient photocatalyst by employing band gap engineering on metal oxide semiconductor surfaces with suitable dopants and to enhance the photocatalytic degradation efficiency of methylene blue in a simple, cost-effective, eco-friendly, sustainable and green approach method for environmental remediation.

Herein, N-Zn-co-doped copper oxide nanoparticles were synthesized using the leaf extract of *Pycnostachys abyssinica* Fresen as a bioreducing, stabilizing, and capping agent due to richness of the phytochemicals it produces. To the best of my knowledge, the biosynthesis of N-Zn-codoped CuO nanoparticles using the leaf extract of Pycnostachys abyssinica Fresen by a simple green method has never been reported. Additionally, the band gap engineering of CuO semiconductors using electron donor (nitrogen) and electron acceptor (zinc) codopants in a green method was considered novel and the best modification of both physicochemical properties to enhance degradation efficiency. Moreover, this method could be more suitable for solar light on a metal oxide surface with efficient photocatalytic properties than undoped and single-doped materials.

1.3. Objectives

1.3.1. General Objective

The main objective of this study was to investigate the photocatalytic activity of biosynthesized N-Zn-codoped CuO nanoparticles for the degradation of methylene blue under natural sunlight irradiation.

1.3.2. Specific Objectives

- To biosynthesize pure, N-doped, Zn-doped, and N-Zn-codoped CuO nanoparticles using the leaf extract of *Pycnostachys abyssinica* and characterize using XRD, UV-Vis, SEM, and FT-IR techniques.
- To evaluate the kinetics and effect of key parameters (dopant concentration, pH, initial dye concentration, catalyst dosage, temperature, and reaction time) on the photocatalytic degradation of methylene blue under natural sunlight irradiation.
- To investigate and compare the photocatalytic degradation efficiency of biosynthesized pure, metal-doped, nonmetal-doped, and codoped CuO nanoparticles for the degradation of methylene blue under natural sunlight irradiation.

1.4. Significance of the Study

This study reports the photocatalytic activity of biosynthesized N-Zn-codoped CuO nanoparticles for degradation of the methylene blue under natural sunlight, using the plant leaf extract of *Pycnostachys abyssinica* Fresen as a bioreducing and capping agent. Additionally, the study explores the potential of semiconductor modification with sustainable dopants to enhance the photocatalytic degradation efficiency of organic pollutants through innovative and green methods. The key significance of this study lies in its contributions to the field of environmental science and sustainable materials; the study highlights the detrimental impact of industrial pollutants, particularly dyes, on ecosystems, it presents a simple, eco-friendly method for treating industrial effluents before their release into the environment, promoting water reuse and conservation. The study explores the potential of semiconductor modification with sustainable dopants to enhance photocatalytic efficiency, contributing to the development of innovative and greener methods for pollutant degradation. It showcases the potential of *Pycnostachys abyssinica* Fresen as a valuable bioresource for synthesizing nanomaterials with environmental applications.

Overall, this study advances our understanding of green synthesis methods for photocatalytic materials and their potential applications in environmental remediation.

CHAPTER TWO

LITERACTURE REVIEW

2.1. Historical Background of Nanoparticles

The use of nanoparticles can be traced back to ancient civilizations, such as Egyptians and the Chinese, who used gold, silver, platinum, and palladium nanoparticles in various applications. European artisans also unknowingly manipulated materials at the nanoscale level, using gold and silver nanoparticles for colouring glass and porcelain. These early practices laid the foundation for the field of nanoscience [49, 50]. The formal study of nanoscience began in the mid-20th century with the development of electron microscopy, enabling scientists to visualize and manipulate materials at the nanoscale. In 1959, Physicist Richard Feynman's lecture at the California Institute of Technology proposed the idea of manipulating individual atoms and molecules, sparking interest in nanotechnology [54]. The invention of scanning tunnelling microscopy and atomic force microscopy in the 1980s further advanced nanoscale research. These instruments allowed for manipulation and study of materials at the atomic and molecular level, fuelling interest in nanoscience and nanotechnology [55]. The Japanese scientist Norio Taniguchi coined the term "nanotechnology" in 1974, and the first international conference on nanotechnology was held in Tokyo in 1986. This conference served as a platform for scientists to discuss the potential of working at the nanoscale, fostering further research and collaboration in the field [56]. Since then, nanoscience has continued to flourish, with groundbreaking discoveries in areas such as nanoparticles, nanomaterials, nanoelectronics, and nanomedicine (state in Table 1). Currently, nanoscience holds immense potential for applications in medicine, electronics, energy, environmental science, and materials science.

2.2. Types of Nanoparticles

Nanoparticles are classified on the basis of size, morphology, and physical and chemical properties. Such are [57]; Carbon-based nanoparticles - primarily consist of carbon nanotubes and fullerenes, Ceramic or inorganic nanoparticles - composed of oxides, carbides, carbonates, and phosphates, Semiconductor nanoparticles or quantum dots - exhibit characteristics of both metals and nonmetals, Polymeric nanoparticles - are organic nanoparticles that exist in the form of nano-spheres and nano-capsules, Lipid nanoparticles

-have a solid lipid core and contain soluble lipophilic molecules. They have a spherical shape and a diameter ranging from 10-100 nm, and Metal nanoparticles - are synthesized from metallic precursors and can vary in form, including nanosized metals, metal oxides, metal sulphides, and metal phosphates.

Table 1: Step revolution of nanotechnology

The revolution steps of nanoscience, nanoparticle, and nanotechnology include:

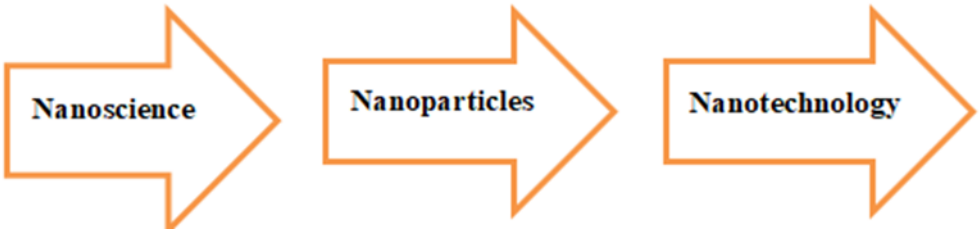

Nanoscience is the study of materials and phenomena at the nanoscale, typically involving the manipulation and characterization of structures and devices with dimensions in the range of 1-100 nanometres.	**Nanoparticles** are the result of the development of techniques to create and manipulate particles at the nanoscale, which has led to the discovery of unique properties & potential applications in various fields.	**Nanotechnology** is the application of nanoscale materials and devices to create new technologies and products that have improved performance [48]

2.3. Metal Nanoparticles

Metal nanoparticles are prepared from metallic precursors and can be nanosized to various metal-based nanoparticles. Metal nanoparticles (MNPs) are tiny particles of metals such as silver (Ag), copper (Cu), titanium (Ti), zinc (Zn), cerium (Ce), and iron (Fe), …etc. have dimensions on the nanometre scale and have at least one structured component with dimensions less than 100 nm. The unique properties of metal nanoparticles, such as a large fraction of surface atoms, large surface energy, spatial confinement, and reduced morphology, make them significantly different from the corresponding bulk materials. These unique properties of nanoparticles make them applicable in the fields of catalysis, agriculture, electronics, biomedical analysis, and even ground water purification [57].

Similar to MNPs in terms of their properties and applications, metal oxide nanoparticles (MONPs) are composed of metal atoms bonded to oxygen atoms to form an oxide

compound. Examples of MONPs include silver oxide (AgO_2 NPs), zinc oxide (ZnO NPs), copper oxide (CuO NPs), and titanium dioxide (TiO_2) NPs [58]. MONPs can exhibit unique physical and chemical properties compared to those of metal nanoparticles due to their limited size, high density of corner or edge surface sites, and presence of oxygen atoms in their structure. For example, MONPs often exhibit enhanced catalytic activity compared to that of pure MNPs due to the presence of oxygen, which can act as a promoter or cocatalyst in various reactions [59].

Metal-based nanoparticles are increasingly being used in various fields due to their exceptional physicochemical properties, which can be controlled through strategic design. In addition to MNPs and MONPS, some of the most commonly applied nanoparticles based on strategic design include but are not limited to [58]; Metallo-organic frameworks (MOFs) composed of zinc, copper, manganese, etc., Metal-sulfide NPs (MsNPs) include copper sulfide NPs, silver sulfide NPs, ferrous sulfide NPs, etc., Spinel ferrite magnetic (SFMNPs) include iron oxide ferrite (Fe_3O_4/ferrite NPs), copper ferrite ($CuFe_2O_4$ NPs), manganese ferrite (Mn-Fe_2O_4 NPs), etc., Metal doped/bimetallic/alloy NPs (DMNPs) include iron–platinum NPs, iron–cobalt NPs (FeCo NPs), iron–nickel NPs, copper–nickel NPs, silver–iron NPs, etc., and Metal or Nonmetal Doped, Codoped and composited metal oxide NPs such as zinc oxide-silver NPs (ZnO-Ag NPs), Nitrogn-zinc oxide NPs (N-ZnO NPs), silver-nitrogen coded titanium oxide NPs (Ag-N-co-doped TiO_2 NPs), and zinc oxide-copper oxide nanocomposites (ZnO/CuO NCs).

Currently, due to the physicochemical properties and the application of metal-based nanoparticles in many fields of science, the scientific community has made extensive efforts to develop a novel and sustainable route for producing nanoparticles.

2.4. Methods for the Synthesis of Metal Nanoparticles

The preparation of these nanoparticles typically involves a reducing and stabilizing agent, with biocompatible agents such as biodegradable polymers and enzymes being preferred for reliable stabilization and surface functionalization [60]. NPs can be produced through physical, chemical, and biological methods (Figure 3), with the two major synthesis approaches being top-down and bottom-up (Figure 1). The top-down approach, which involves the use of physical and chemical means to reduce bulk material into nanosized particles, was previously widely used but is now less preferred due to its high material and energy requirements. In contrast, the bottom-up approach is now the preferred method for

nanoparticle synthesis at laboratory scales. This approach involves a homogeneous system in which catalysts, such as reducing agents and enzymes, produce nanostructures that are restricted by catalyst properties, reaction media, and conditions, e.g., solvents and stabilizers [48].

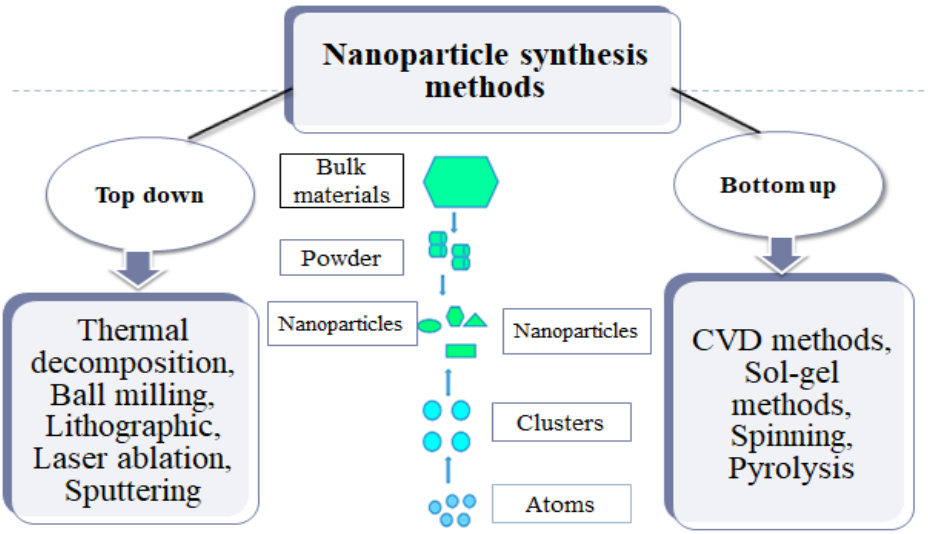

Figure 1: Summary of the top-down and bottom-up approaches for synthesizing green nanoparticles

The top-down approach typically results in crystalline samples, such as small single crystals or polycrystalline materials formed from previous "thermodynamically" starting materials. In a crystalline solid, a thermodynamically formed product usually complies with the ideal crystal structure of the specific compound. On the other hand, the bottom-up route results in the formation of minute particles from crystalline areas that do not correspond to the ideal lattice (defect structure). These structures are difficult to illustrate and are typical kinetic products, meaning that they do not have sufficient time for ideal crystal growth [61].

2.4.1. Physical Method for the Synthesis of Nanoparticles

The physical methods used for the synthesis of nanoparticles via a top-down approach include thermal decomposition, arc discharge, diffusion, UV irradiation, sonochemistry, laser ablation, and radiolysis (Figure 3). During the physical synthesis process, evaporization of metal atoms occurs, followed by condensation on various supports, in which the metallic atoms are rearranged and aggregated as small clusters of metallic nanoparticles [62]. Using physical approaches, we can obtain nanoparticles with high purity and a definite shape. However, these processes usually require highly sophisticated

instruments, chemicals and radiative heating as well as high power consumption, which leads to high operating costs [63].

2.4.2. Chemical Method for the Synthesis of Nanoparticles

Another approach for synthesizing nanoparticles is chemical methods. Metallic precursors, stabilizing agents, and reducing agents such as sodium citrate, $NaBH_4$, and elemental hydrogen are utilized to reduce metal ions into nanosized particles. The synthesis process typically involves two steps: nucleation and growth. Chemical methods (Figure 3) commonly include sol-gel techniques, chemical precipitation, and colloidal synthesis depending on the reaction mixture conditions, and metal ions can either favour nucleation or aggregation, leading to the formation of small clusters of metals [62]. Stabilizing agents such as synthetic or natural polymers such as cellulose, natural rubber, chitosan, and copolymer micelles are also employed. These agents are hydrophobic and necessitate the addition of organic solvents such as ethane, dimethyl formaldehyde, toluene, and chloroform. However, these chemicals have toxic and nonbiodegradable properties, limiting their scalability. Additionally, some toxic chemicals can contaminate the surface of nanoparticles, rendering them unsuitable for certain biomedical applications. To overcome the limitations of physical and chemical methods, scientists and researchers are actively exploring alternative processes for metal nanoparticle synthesis [64].

2.4.3. Biological Method for the Synthesis of Nanoparticles

Biological approaches have been found to be more eco-friendly, with green synthesis using microbes, enzymes, vitamin substrates, and plant phytochemicals. This method has been shown to be the most efficient, biocompatible, and safe and is the most common method used for the synthesis of nanoparticles [65]. The biosynthesis of nanoparticles is more unique and reliable not only because of their lower toxicity than some physicochemical production methods but also because they can be used to produce large quantities of nanoparticles that have good morphology, shape, and size and are free of combination.

2.4.4. Green Synthesis of the Nanoparticles

The process of synthesizing stable nanoparticles via biological methods is referred to as green nanobiotechnology. Basically, the green synthesis of nanoparticles follows the ***"Twelve principles of Green Chemistry***", which helps in the design and manufacture of different environmentally friendly chemical products and reduces the impact on human

health; additionally, these products are produced through regulation, control, clean up, and remediation processes until their eco-friendliness is directly enhanced.

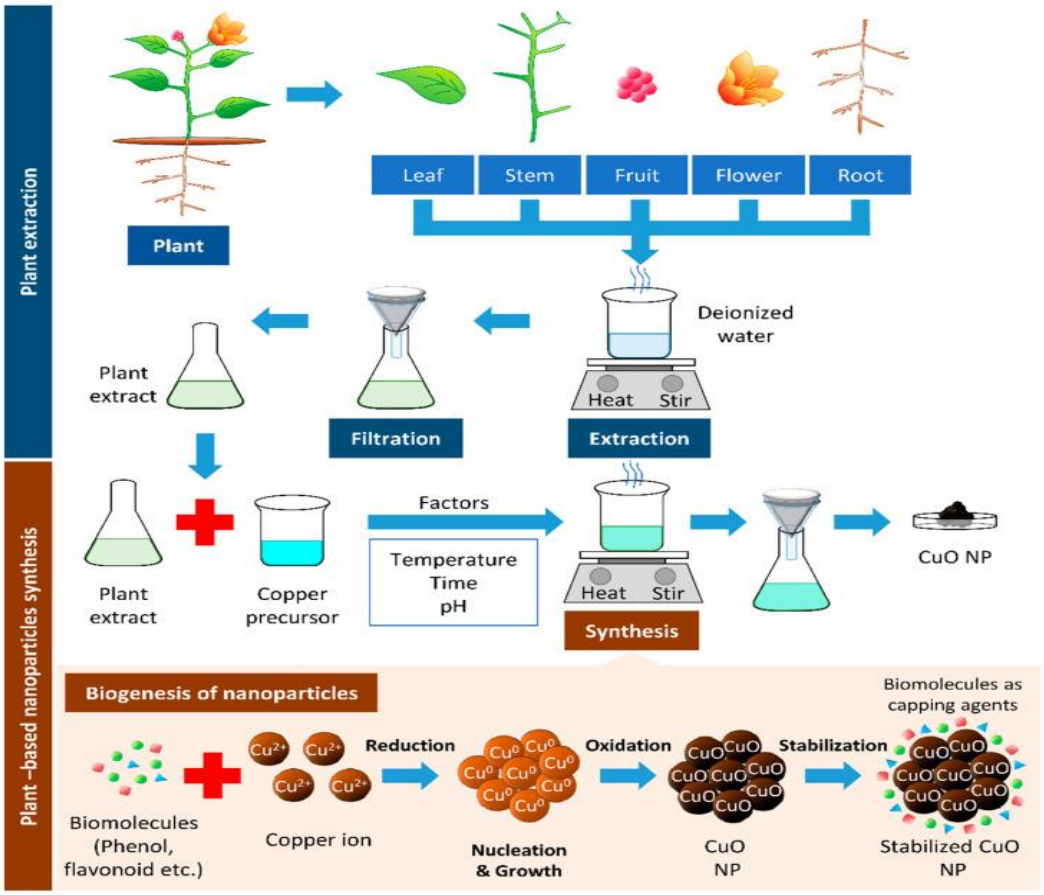

Figure 2: Schematic diagrams showing the general steps for plant-assisted nanoparticle synthesis (adapted from [66])

Some basic principles of "***green synthesis***'' can thus be explained by several components, such as prevention/minimization of waste, reduction of derivatives/pollution, and the use of safer (or nontoxic) solvent auxiliaries as well as renewable feedstock [64]. The use of plant extracts is a simple and efficient method for the large-scale production of green metal nanoparticles. The synthesis process depends on factors such as solvent, temperature, pressure, and pH. The plant extracts shown in Figure 2 contain effective phytochemicals such as ketones, aldehydes, flavones, amides, terpenoids, glycosides, tannins, steroids and carboxylic acids that can reduce metal salts into nanoparticles, making them a popular choice for green synthesis [66].

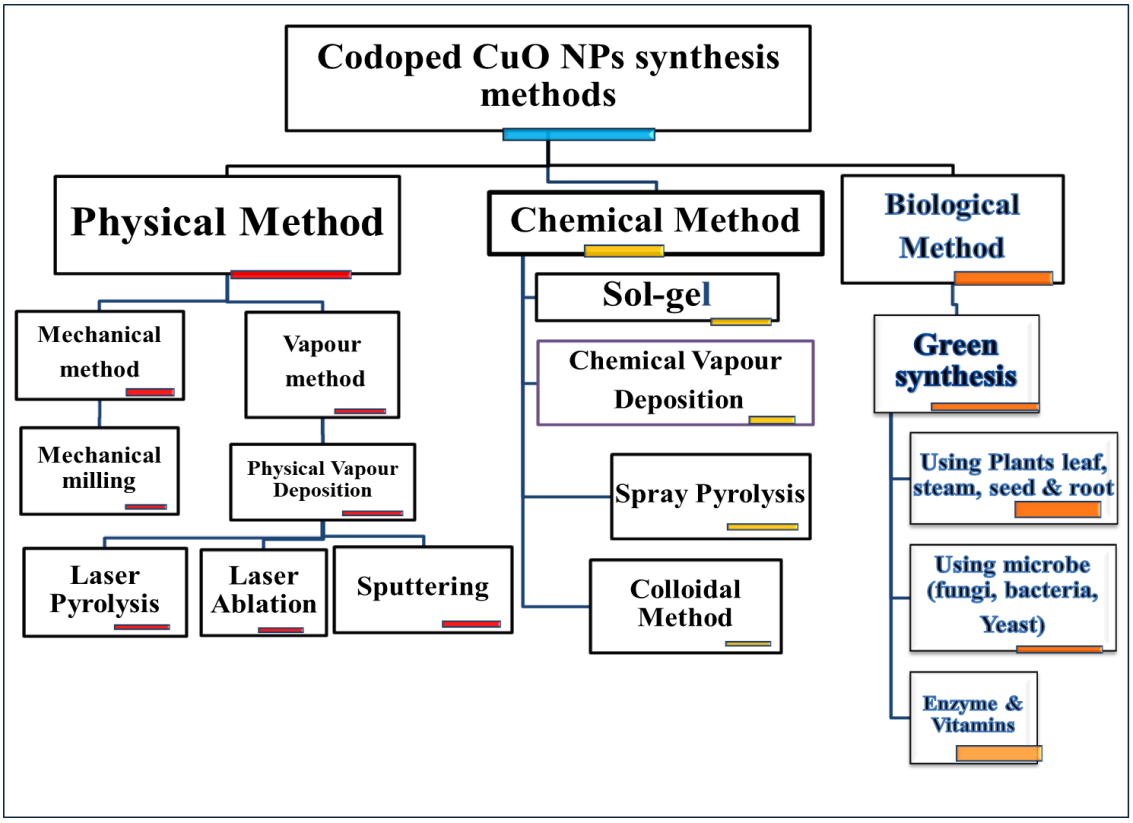

Figure 3: Summarization diagram of metal nanoparticle synthesis methods

2.5. *Pycnostachys Abyssinica* Fresen

The Lamiaceae family is commonly found in temperate regions and consists of approximately 3500 species across over 200 genera. In Ethiopia, there are 41 genera within this family. The genus *Pycnostachys*, which belongs to the Lamiaceae family, is native to tropical Africa and South Africa, including Madagascar [44]. In Ethiopia, there are six species of *Pycnostachys*. Among these species, *Pycnostachys abyssinica* Fresen., *Pycnostachys recurvata Ryding, and Pycnostachys sp*. Mesfin & Kagnew (code no. GY 2249) are recognized as endemic species [67]. *Pycnostachys abyssinica* Fresen, commonly known as "Olomuwa" in the Wolaita language, is a medicinal plant that is extensively utilized. *Pycnostachys abyssinica* Fresen is a plant (Figure 4) that typically grows to a height of one to two metres. It has an erect stem that is straight with branches arising from the base. The leaves of the plant are large, ovate, and serrated. They are arranged in opposite pairs along the stem and have a green upper side and a dense covering of fine hairs on the bottom. The flowers of *Pycnostachys abyssinica* are small, tubular, and arranged in dense spikes at the top of the stem. They have a pale lavender or lilac color and are surrounded by leaf-like bracts. The plant blooms from October to December and attracts bees and other pollinators.

Herbal medicines are used by approximately 80% of the global population, especially in rural areas of developing nations, as reported by the World Health Organization [68]. The aromatic medicinal plant Pycnostachys Abyssinica is widely used in traditional Ethiopian medicine because of its anthelmintic, antidiabetic, antimicrobial, antiviral, antioxidant, antibacterial, insect repellent, and molluscicidal properties. Recent research has investigated its phytochemical composition—alkaloids, flavonoids, glycosides, phenols, terpenoids, tannins, steroids, and acidic compounds [67, 46, 44]; its biological activities—antimicrobial, antioxidant, anti-inflammatory, and antimalarial activities [67, 69, 45, 70]; and its ethnopharmacological applications [71, 72], which have been scarcely investigated, particularly concerning the Ethiopian variety of the species.

Figure 4: Pycnostachys abyssinica plant (photo captured by Yohannes S. on 10 Jan 2023)

The active compounds found in plants have been shown to increase the size, structure, and stability of synthesized nanoparticles. One such example is flavonoids, which are a class of polyphenolic chemicals that can effectively bind to metal ions and reduce them to nanoparticles [73].

2.6. Characterization of Metal Nanomaterials

The characterization of nanoparticles involves various physical and chemical analysis techniques [48], including UV–Vis spectroscopy, Fourier transform infrared spectroscopy (FT-IR), scanning electron microscopy (SEM), X-ray diffraction (XRD), atomic force

microscopy (AFM), dynamic light scattering (DLS), surface-enhanced Raman spectroscopy (SERS), atomic absorption spectroscopy (AAS), energy dispersive spectroscopy (EDS), X-ray photoelectron spectroscopy (XPS), and high-angle annular dark-field (HAADF).

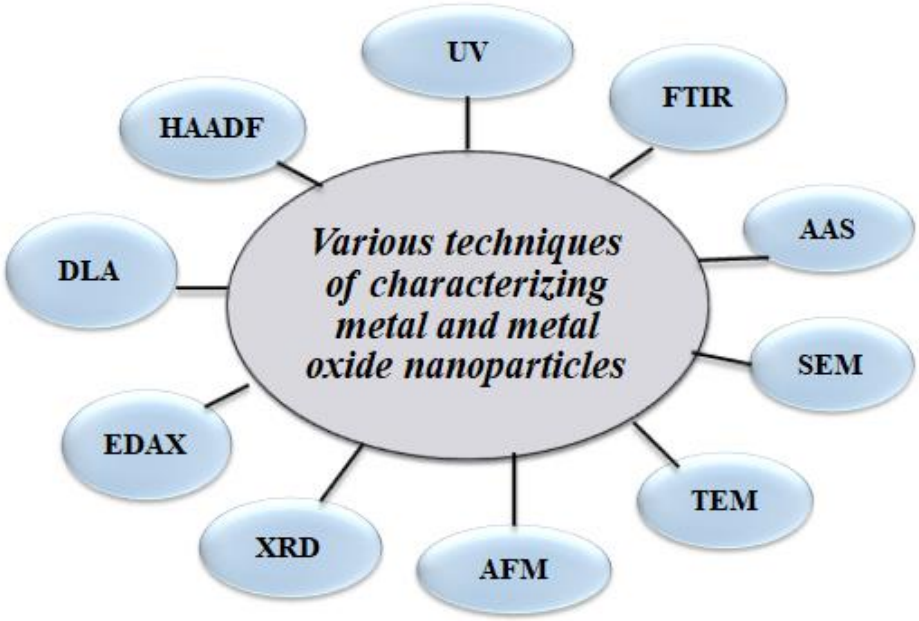

Figure 5: Summary of the various techniques for characterizing metal and metal oxide nanoparticles

These techniques (Figure 5) provide information on the elemental composition, structure, and concentration, and when combined, they offer a more comprehensive understanding of the nanoparticles [74].

2.7. Applications of Metal Nanoparticles

Metallic nanoparticles are known for their unique and specific properties, such as conductivity, catalytic properties, biocompatibility, high surface area-to-volume ratio and density. Therefore, the produced metallic nanoparticles have a wide variety of applications (Figure 6) in medicine, drug delivery, sensors, cosmetics, agriculture, biomedical sciences, catalysis, light emitters, optics, electronics, food, environmental remediation and so on [57].

Currently, metal-based green synthesized nanoparticles (GNPs) generated via biological methods have received considerable attention from researchers and have been widely applied in all fields due to their very important therapeutic properties and substantial beneficial effects in biomedicine; reduced harmful environmental effects and high

fertilizer use in agriculture; heavy metal detoxification; and elimination of harmful emissions such as carbon dioxide, nitrous oxide, and methane in environmental remediation [75]. As the different parts of plant roots, stems, leaves, seeds, and fruits contain many phytochemical substances; the green synthesis of metallic nanoparticles is cost effective, nontoxic, and eco-friendly and is more efficient than other biological methods for sustainable application in all fields.

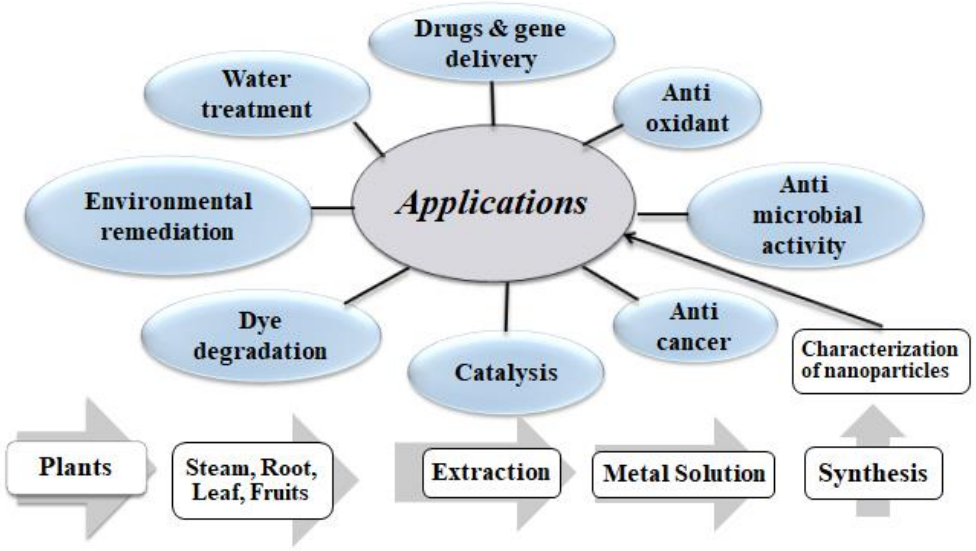

Figure 6: Green syntheses of metal and metal oxide nanoparticles and their applications

2.8. Photocatalytic Degradation of Organic Dyes

2.8.1. Organic Dyes and their Sources

Organic dyes are complex aromatic compounds that provide color, intensity, solubility, fastness, and substantiveness. Unlike most organic compounds, organic dyes are colored because they absorb light in the visible spectrum (400–700 nm); have at least one chromophore (color-bearing group), such as azo (-N=N-), carbonyl (>C=O), nitro ($-NO_2$), or imine (-C=N-), a conjugated system; and exhibit resonance of electrons [76]. The chromophores (Figure 7) in organic dyes are a group of atoms, which are highly conjugated systems of alternating single and double bonds that absorb certain wavelengths of light, resulting in the appearance of color [5].

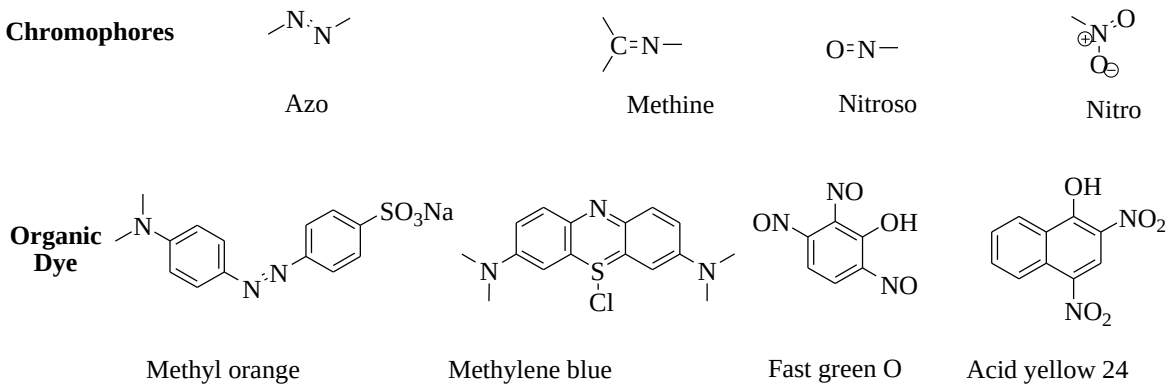

Figure 7: Some chromophoric groups present in organic dyes

Organic dyes are classified (Figure 8, left) on structural bases as basic dyes, acidic dyes, azo dyes, disperse dyes, and anthraquinone-based and metal complex dyes [77].

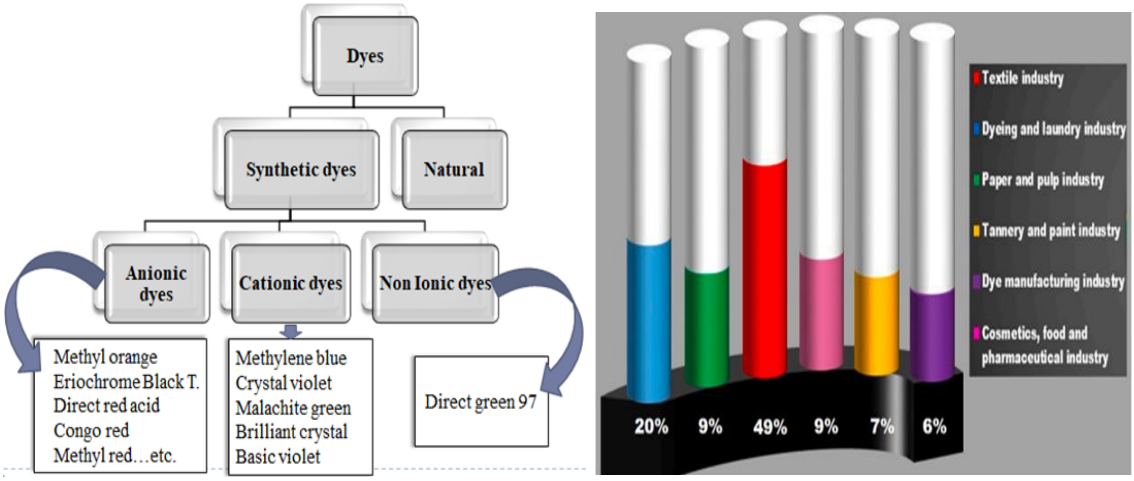

Figure 8: Classification of dyes (left) and sources of notorious dye runoff (right)

Approximately 49% of the total dyes are lost (Figure 8 right) among the total dyes produced worldwide during the dyeing processes of textile runoff. In addition, a number of dyes reach drinking water. These dyes discharged to the environment can adhere to surfaces through solution, covalent bonds, complexes with salts or metals, physical adsorption, or mechanical retention and cause serious disorder in ecosystems [78].

2.8.2. The Toxic Effects of Organic Dyes on Ecosystems

Many organic dyes like to heavy metals such as lead, mercury, chromium, and cadmium can accumulate in the body and cause damage to the nervous system, kidneys, and other organs; aromatic amines (azo and nitro compounds) have been found to be carcinogenic and can cause adverse effects on the skin, respiratory system, and other organs. Other toxic compounds found in organic dyes may include benzene, formaldehyde, and various

organic solvents, which can have harmful effects on human health and the environment [79]. These dyes can cause harm to the environment by altering the physical and chemical properties of soil, deteriorating water bodies, and harming flora and fauna [77]. It was observed that the toxic nature of dyes causes death to soil microorganisms, which in turn affects agricultural productivity. The presence of very small amounts of Azo dyes in water (< lppm) is highly visible. This affects aesthetic transparency and water-gas solubility, reducing light penetration through water, decreasing photosynthetic activity, causing oxygen deficiency and deregulating the biological cycles of aquatic biota.

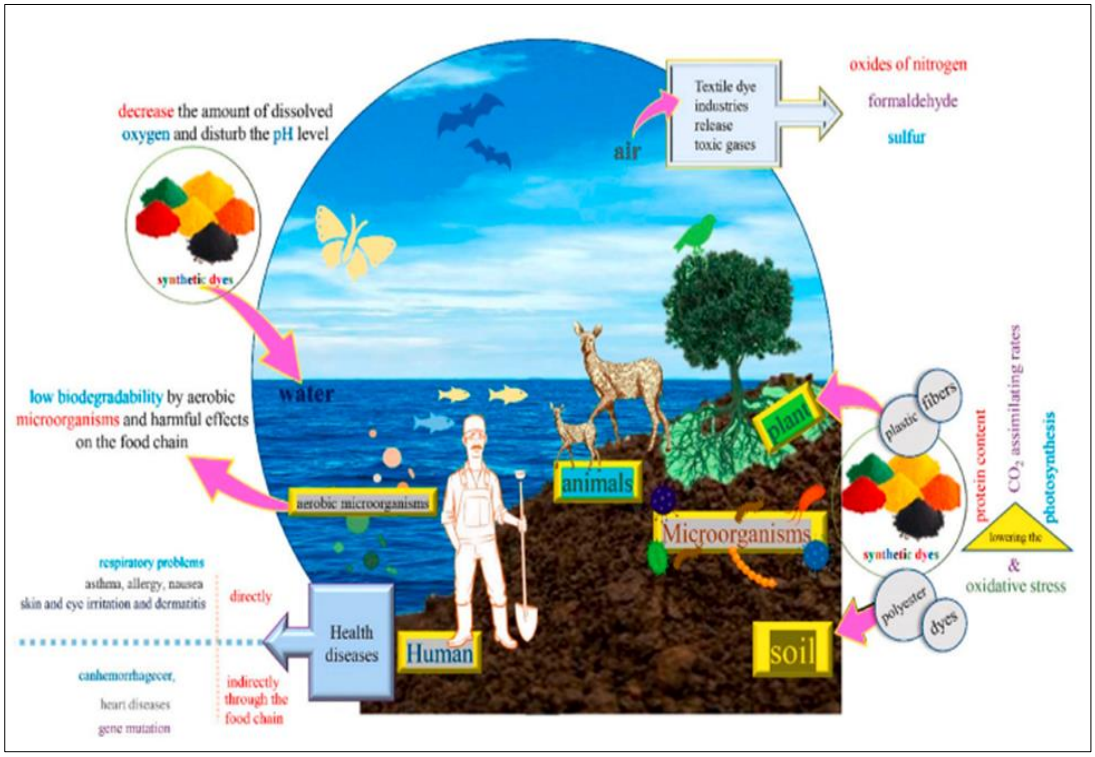

Figure 9: Ecological impacts of dye effluents

Furthermore, these long-lasting dyes can cause severe allergic reactions and genetic mutations leading to cancerous growth, increase the biological oxygen demand in water bodies, inhibit the growth of photosynthetic organisms, and damage the ecological system and essential environmental connections [80, 78], as depicted in Figure 9.

Methylene blue (MB), as shown in Figure 10, is an aromatic amine organic dye. The negative impact of organic dyes on ecosystems is evident in the case of the cationic dye methylene blue (MB), which is commonly used in various industries, such as dyeing, coloring, and coating. This dye has been found to cause harmful effects in humans, including cyanosis, vomiting, increased heart rate, paralysis, shock, jaundice, and tissue necrosis. Furthermore, wastewater containing methylene blue can block sunlight from

penetrating water, leading to reduced photosynthetic function in plants and harm to aquatic and marine ecosystems [5, 2].

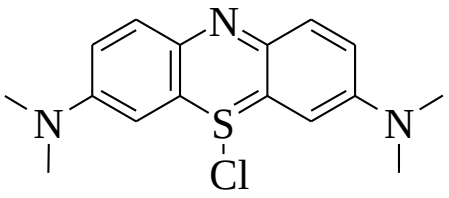

Figure 10: Chemical structure of methylene blue

2.8.3. Photocatalysis and Photocatalyst

Photocatalysis is the process of emitting light to semiconductors, generally metal oxides, which activate and accelerate chemical reactions by moving electrons from the valence band to the conduction band. Photocatalysts are semiconductor materials that absorb light; they act as catalysts, generating electron-hole pairs [14]. This type of reaction (Figure 11, left) is accelerated by the absorption of a photon with enough energy, equal to or greater than the band-gap energy (E_{bg}) of the catalyst. This absorption causes charge separation by promoting an electron from the valence band to the conduction band, creating a hole (h^+) in the valence band. This band-to-band excitation produces oxidative valence band holes (h^+_{vb}) and reductive conduction band electrons (e^-_{cb}) [81]. A photo-excited electron is utilized to reduce an acceptor, while a hole is utilized to oxidize donor molecules. The significance of photocatalysis lies in the fact that it offers both oxidation and reduction environments simultaneously.

Semiconductors (Figure 11, right) are capable of conducting electricity even at room temperature in the presence of light and hence work as photocatalysts. Metal oxides such as AgO_2, ZnO, CuO, TiO_2, MgO, SiO_2, CeO_2, and Fe_2O_3 can soon act as semiconductors because they have a band gap between their valence and conduction bands, light absorption properties, the required electronic structure, and charge transport characteristics [82]. Most metal oxide photocatalysts have a wide band gap (E_{bg}) and are 96% active in the UV region and only 4% responsive to semiconductors in the visible region. To overcome this problem and enhance photocatalytic activity, different modification methods have been applied to the surface of semiconductors.

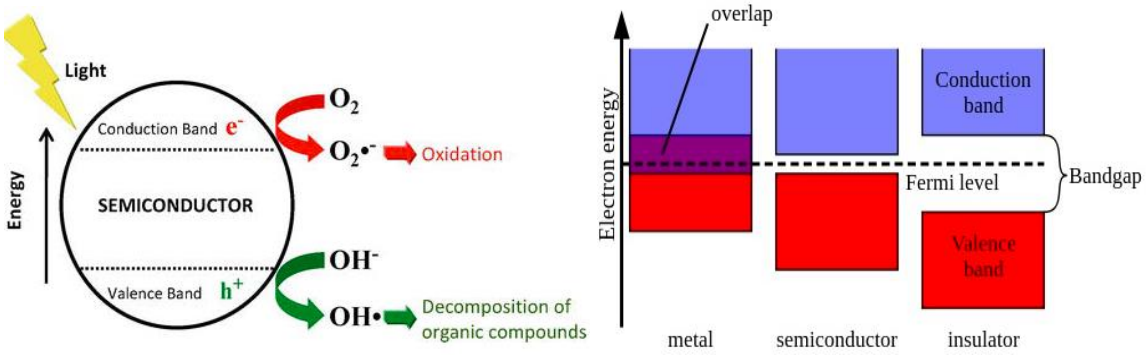

Figure 11: Photocatalysis reaction (**left**) and conduction properties of the materials (**right**)

2.8.4. Modification of the Photocatalyst Semiconductor

All semiconductors do not have suitable band gaps or band alignments for efficient application and are modified by various strategic techniques (Table 2) to enhance their performance by controlling their physiochemical properties to introduce specific functionalities for targeted applications such as photodegradation [51].

Table 2: Techniques involved in semiconductor modifications

Modification method	**Techniques**	**Reasons for modification**
Doping with metal and/or nonmetal	Reduces the band gap by formation of localized state just above the valence band or just below the conduction band by adding dopant impurities in semiconductor	↓ It avoids electron-hole recombination, ↓ Provides enhanced surface area and pore size ↓ High crystalline state and smaller size ↓ Extends sensitivity towards a broad range of spectrum e.g. N-TiO_2, Ni-ZnO
Codoping with bimetal or metal/nonmetal or binonmetal	Reduces the band gap by formation of localized state just above the valence band and just below the conduction band by adding combinations of donor and acceptor species at once	↓ Raising the Vb edge & lowering the Cb edge ↓ Towards a broad range of solar spectrum ↓ Solving carrier recombination solubility limit, and Increases the electron injection efficiency ↓ Possesses stability under a long duration of irradiation ↓ Controlled the morphology and final crystal phases e.g. N-F-codoped TiO_2; Ga-Cu-codoped ZnS
Coupled MOS (Composites of MOs)	Inserting electron from small band gap semiconductor to a large band gap semiconductor coupling them on surface	↓ Develop to the synergistic effect and reduction in charge recombination ↓ Smaller crystal size, and spongy microstructure with low agglomeration ↓ A stronger response to visible light e.g. $FeTiO_3/TiO_2$; TiO_2/SnO_2; ZnO/Ag_2S
Substitution	Substituting one metal by another metal with hiving same valence	↓ Shifting CB edge to the lower side e.g. $CaFe_2O_4$-$MgFe_2O_4$
Sensitization	Surface modification with photosensitizers (synthetic, natural, self-sensitizer)	↓ Inject & transfer electrons to the conduction band ↓ Enhance the photosensitivity of the semiconductor ↓ Good size and morphology e.g. Self (CdSe, CdTe), natural (plant extract); synthetic (and organic dye and substrates)

For example, as the percentage of surface atoms on NPs increases, they become more reactive but less stable, leading to a strong tendency to undergo agglomeration. Surface modification of metal oxide NPs can be achieved through physical (physisorption with surfactants or macromolecules) or chemical (covalent grafting of modifiers) routes to prevent this problem [83]. Metal oxide semiconductors can be modified using post-modification or in situ methods. Post-modification involves modifying preformed MONPs with modifier molecules, while in situ methods involve adding stabilizers or surface-modifying agents such as metal and nonmetal dopants, polymers, and inorganic and organic oxides during NP formation to prevent aggregation and control particle size and shape. This method is more complex than post-modification, but it offers better control over the properties of the MOS [84, 85]. Based on both modification methods (Figure 12), the photocatalytic performance of a semiconductor can be enhanced in five basic ways: 1) by the formation of a localized state just above the valence band (**A**), 2) by the use of a semiconductor with a low band gap (**B**), 3) by the formation of a localized state just below the conduction band (**C**), 4) by the formation of a colour centre in the band gap (**D**), and 5) by surface modification (**E**).

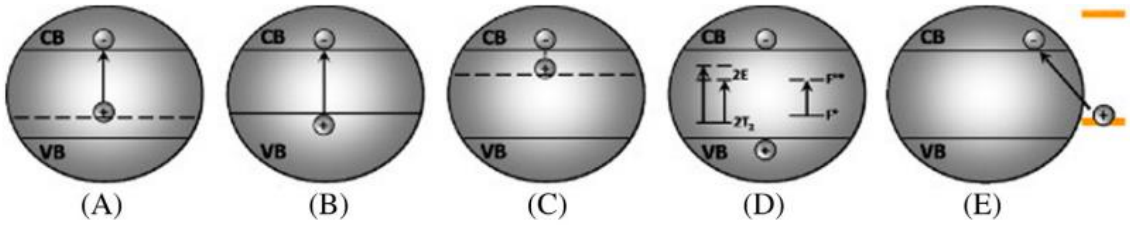

Figure 12*:* Modification techniques for metal oxide semiconductors (adopted from [14])

These modifications play a vital role in controlling the physiochemical properties of semiconductors, including enhancing their stability, improving their dispersibility in different solvents or matrices, redesigning their size and shape, and meeting specific requirements for targeted applications such as drug delivery, imaging, sensing, catalysis, and photodegradation.

2.8.5. CuO Semiconductor

Cu is a multipurpose 3d transition metal with diverse physical and chemical properties. Its ability to access various oxidation states (Cu^0, Cu^I, Cu^{II}, and Cu^{III}) allows for reactions through both one- and two-electron pathways, making Cu-based materials highly reactive and adaptable [86]. In the field of materials research, metal oxide semiconductors (MOSs) have been a fascinating topic. Among various MOSs, copper oxide (CuO) is a particularly

popular choice due to its intriguing structural, chemical, optical, and electrical characteristics. CuO is a black powder that is insoluble in water. It is one of the hardest materials due to its high melting temperature (1,326 °C) and boiling point (approximately 2,330 °C). CuO has a unique crystal structure that consists of copper ions and oxygen ions arranged in a monoclinic lattice. Unlike other MOSs, which crystallize in a cubic rock salt structure with possible rhombohedral distortions, CuO has a lower-symmetry monoclinic cell. This crystal structure endows CuO with unique physiochemical properties, such as high thermal stability, high electrical conductivity, and excellent catalytic activity [87]. It is a p-type semiconductor with an indirect energy band gap (Eg) of 1.2 eV-1.9 eV, which makes it suitable for use in solar cells and optical, photovoltaic and other optoelectronic devices [15] and has excellent solar light absorbance.

In recent years, it has been used as a base material for several applications, including solar energy cells [88], optoelectronics [16], catalysis [17], biosensors, supercapacitors [18], lithium-ion batteries, electrochemical sensors, fuel cells [19], gas sensors, hydrogen storage devices, and photocatalysis [20]. CuO is also known for its ability to absorb and desorb gases, making it an excellent material for gas sensors [87]. CuO has been extensively studied for its potential use in biomedical applications and can be used as an effective drug delivery agent, antibacterial agent, antimicrobial agent, and cancer treatment agent due to its ability to induce cancer cell apoptosis [89].

2.8.6. Doping and Codoping of CuO NPs

Like other semiconductors, CuO NPs do not have a suitable band gap or band alignment to exhibit on-stand efficiency. However, doping copper oxides with metals and nonmetals can be an effective approach for adjusting the band gap to an optimal range for efficient photocatalysis [90].

When metal oxides are doped with impurities, they can become either n-type or p-type semiconductors (Figure 13). The impurity level can act as either an acceptor or a donor, depending on its energy position relative to the valence band and conduction band. If the dopant impurity level is located near the valence band, it can accept an electron from the valence band, creating a localized hole, which results in a ***p-type*** dopant. On the other hand, if the impurity level is located near the conduction band, it can supply/donate an electron to the conduction band, creating additional mobile electron charge carriers, which results in an ***n-type*** dopant. Sometimes, both p-type and n-type dopants are introduced

simultaneously, resulting in a p-n junction or "codoping" of the dopants in different regions of the semiconductor material [18, 91].

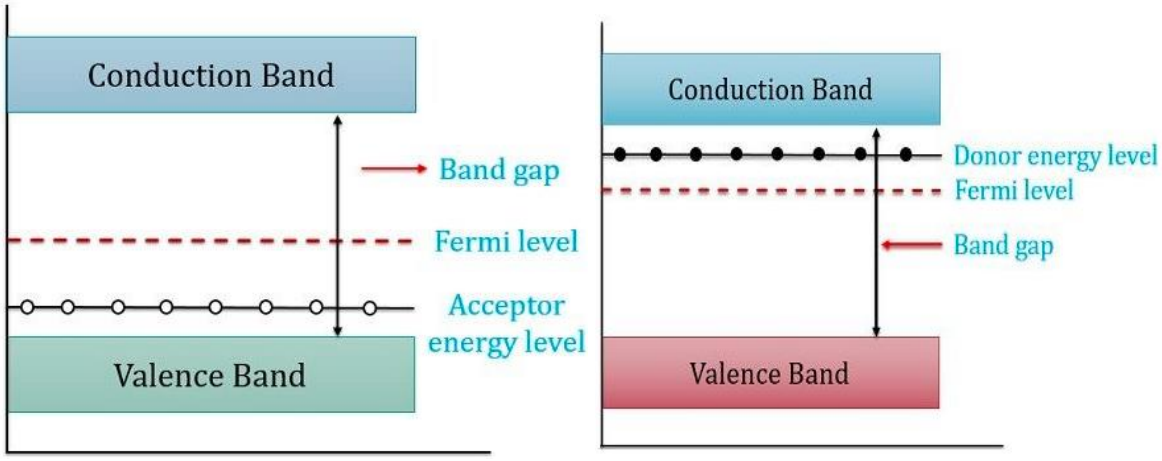

Figure 13: Energy level diagram of p-type (**left**) and n-type semiconductors (**right**)

It is important and necessary to manipulate the energy band gap of CuO to customize its light absorption capacity for a specific application, given that it is categorized as a wide bandgap semiconductor with an energy band gap extending to 1.2 eV -1.9 eV. The photodegradation and photocatalytic activities of CuO semiconductors can be enhanced by increasing the band gap through the incorporation of suitable foreign materials known as dopants (such as Fe, Co, N, Zn, F, Ni, and Ag) at appropriate concentrations. The incorporated dopants frequently stretch and distort the monoclinic crystal structure of CuO semiconductors and ultimately shrink or widen the energy gap of the semiconductor [92].

Nonmetal doping has been found to be a promising approach for shifting the absorption edge. Various nonmetals have been explored for single-element doping or codoping with other elements. The success of this strategy depends on the dopant selection and synthesis method, which determine the chemical state, amount, and position of the nonmetal. The anionic dopant must have a lower electronegativity than oxygen to create a new valence band at a higher energy level. The dopant should also have a similar size to the lattice oxygen atoms to avoid altering the intrinsic properties of the semiconductor. Nitrogen is the best option due to its similar anionic radius and lower EN than oxygen [93]. This improves their optical properties and makes them ideal for applications such as optoelectronic devices, photovoltaic, and photo electrochemical cells.

Metal dopants in metal oxide semiconductors can enhance their photocatalytic activity through various mechanisms. These include the formation of impurity energy levels that act as trap states for charge carriers, modification of the electronic structure to create new

energy bands or shift existing ones, facilitation of charge separation by introducing new energy levels that act as charge trapping sites, and creation of oxygen vacancy defects that serve as active sites for redox reactions during photocatalysis [94]. Codoping CuO NPs with nonmetals and metals increases their photocatalytic activity.

2.9. Experimental Parameters for Photocatalytic Degradation

The experimental parameters for photocatalytic degradation included the type of photocatalyst used, the concentration and type of pollutant, the pH of the solution, the intensity and wavelength of the light source, the reaction time, and the temperature. Optimization of these parameters is essential to achieve maximum efficiency and cost-effectiveness in photocatalytic degradation.

2.9.1. Types of Photocatalysts used and Doses

The type of photocatalyst used affects photocatalytic degradation by influencing factors such as the bandgap energy, catalytic activity, stability, specific surface area, and crystal structure. These factors determine the efficiency and effectiveness of the degradation process [95]. For example, a photocatalyst with a high surface area will have more active sites for reactions to occur, while a stable photocatalyst will be able to maintain its activity over a longer period of time. Different photocatalysts have different bandgap energies, which means that they are more or less effective at absorbing different wavelengths of light and affecting electron-hole pair generation and subsequent reactions [96]. Therefore, careful consideration of the photocatalyst is essential for achieving optimal results in photocatalytic degradation. In addition, the photocatalytic degradation efficiency of dyes increases as the photocatalyst dosage increases to the optimum point due to an increase in the number of hydroxyl and superoxide radicals and the number of active sites, beyond which the efficiency decreases due to light penetration inhibition, and fewer hydroxyl radicals are generated. The aggregation of nanoparticles at high catalyst doses may also contribute to a lower degradation percentage by reducing the number of active sites and producing fewer active radicals. In heterogeneous photocatalytic reactions, the photodegradation of dye is proportional to the amount of loaded catalyst and increases as a result of an increase in the amount of loaded catalyst [3].

2.9.2. Intensity and wavelength of the light source

The rate of photocatalysis is affected by the intensity and wavelength of the light source. The number of photons absorbed by the photocatalyst is determined by the light intensity, while the energy of the absorbed photons is determined by the light wavelength. The light intensity influences the pace of the photochemical process and the total pollutant transformation and destruction efficiency [97, 98]. A study on photo reduction found that the largest initial reaction rate was achieved using red wavelength light at its highest intensity, while the maximum conversion was attained using white wavelength light at its lowest intensity [99].

2.9.3. Pollutant Dye Type and Its Initial Concentration

The type of pollutant dye can affect photocatalytic degradation in several ways. First, the chemical structure and properties of a dye can determine its susceptibility to photocatalysis. Some dyes may have a greater affinity for the photocatalyst surface, while others may be more resistant to degradation due to their complex molecular structures. Second, the concentration of dye in solution can also impact photocatalytic degradation. Higher concentrations of dye may require longer exposure times or higher intensity light sources to achieve effective degradation. Additionally, the presence of other contaminants in the solution can also interfere with photocatalytic degradation of the dye [100]. As the initial dye concentration increased, more dyes became available for degradation, and this trend reached the optimum point. The decrease in degradation efficiency with increasing initial dye concentration above the optimum value is primarily due to the large amount of adsorbed dye, which may also inhibit reactions between dye molecules and reactive radicals. Since an excessive dye concentration may hinder light penetration into the solution, fewer photons can reach the photocatalyst surface. However, the degradation rate decreased with further increases in dye concentration.

2.9.4. Reaction Time

The reaction time is important to ensure complete degradation of the pollutant. The longer the reaction time is, the more time the photocatalyst has to interact with the pollutant and break it down. However, there is an optimal reaction time beyond which further exposure to light does not result in any significant increase in degradation efficiency. This is because the active sites on the photocatalyst surface may become saturated or deactivated over time, leading to a decrease in photocatalytic activity [98].

2.9.5. pH of the Solution

The pH of the solution significantly affects photocatalytic degradation because it can influence the surface charge and chemical properties of the photocatalyst and can also influence the solubility and stability of the pollutant. The optimal pH for photocatalytic degradation depends on the specific photocatalyst and pollutant being used. Generally, a neutral or slightly acidic pH is preferred for most photocatalytic reactions. At extreme pH values, the photocatalyst surface may become chemically unstable, leading to a decrease in photocatalytic activity [101]. Additionally, the pH can affect the solubility and ionization state of the pollutant, which can impact its interaction with the photocatalyst surface. Depending on the solution pH, either positive or negative charges can be formed on a surface since H^+ and OH^- are the charge-determining ions for most surfaces. Therefore, at lower pH, protonation of the catalyst creates a surface with a positive charge, making the catalyst behave as a strong Lewis acid. The anionic dye, with strongly ionized anionic groups, serves as a strong Lewis base and can be readily adsorbed on the positively charged catalyst surface [102].

2.9.6. Temperature

Temperature can also influence the rate of photocatalysis by affecting the adsorption and desorption of pollutants on the photocatalyst surface. In general, higher temperatures can increase the rate of the reaction, as they provide more energy for the photocatalytic process to occur. However, excessively high temperatures can also lead to thermal degradation of the photocatalyst and/or the pollutant, which can decrease the efficiency of the reaction. Therefore, it is important to optimize the temperature for each specific photocatalyst and pollutant to achieve maximum degradation efficiency [98, 103].

2.10. Kinetics of Photocatalytic Degradation

A kinetic study of the photocatalytic degradation reaction involves the analysis of the rate of degradation of a target pollutant under optimum conditions. This includes the determination of the reaction rate constant, reaction order, and activation energy of the photocatalytic process. The study typically involves the use of a photocatalyst material, such as a metal oxide, and a light source, such as UV light or visible light, to initiate the degradation reaction [104]. Based on the experimental data, mathematical models have been developed to describe the degradation kinetics. These models often follow rate laws such as pseudoo-zero order, pseudo-first order, pseudo-second order, and BMG kinetics,

depending on the reaction mechanism. Thus, a pseudo zero-order reaction is observed for saturation coverage on the surface of the catalyst since the catalytic degradation rate is independent of the change in dye concentration, as shown in Equation (1):

$$-\frac{d[D]}{dt} = k \tag{1}$$

Integrating the equation under the boundary conditions $[D] = [D]_o$ at $t = 0$ and $[D] = [D]_o$ at $t = t_{1/2}$ yields

$$[D]_o - [D] = k_o t \tag{2}$$

$$t_{1/2} = \frac{[D]_O}{2k} \tag{3}$$

A plot of $[D]_o$-[D] vs reaction time gives a slope equal to the zero-order rate constant (k_o). Additionally, the half-life ($t_{1/2}$) is the time required to degrade half of the initial dye concentration, which is used to quantitatively compare the degradation reactions. Therefore, the zero-order $t_{1/2}$ can be expressed by Equation (3), and it increases with the initial concentration of dye molecules.

On the other hand, at low initial concentrations of dye molecules, i.e., (K[D] + 1) = 1, a pseudo first-order rate expression is obtained, as shown in Equation (4). The equation is valid by assuming that the driving force of degradation is constantly proportional to the dye concentration.

$$-\frac{d[D]}{dt} = k_1[\mathrm{D}] \tag{4}$$

where k_l corresponds to the first-order rate constant. Integrating the equation under the two boundary conditions yields:

$$ln\frac{[D]_O}{[D]_t} = k_1 t \tag{5}$$

$$t_{\frac{1}{2}} = \frac{ln2}{k_1} = \frac{0.693}{k_1} \tag{6}$$

The linear region can be obtained from the plot of $\ln([D]_o/[D]_t)$ versus reaction time, in which the slope gives the rate constant of degradation. This model is the most common model used to represent the entire degradation process. Here, the half-life is derived from Equation (6). Obviously, the $t_{1/2}$ of the first-order model is independent of the dye concentration.

A second-order reaction in which a single reactant is involved is characterized by a chemical reaction (2[D] → products). At equilibrium, the second-order kinetics depend on the amount of dye molecules adsorbed on the catalyst surface.

$$-\frac{d[D]}{dt} = k_2[D]^2 \tag{7}$$

Similarly, by integrating the equation under the two boundary conditions, the second-order rate constant (k_2), as well as $t_{1/2}$, can be obtained. The second-order $t_{1/2}$ increases as the initial concentration decreases.

$$\frac{1}{[D]} - \frac{1}{[D]_o} = k_2 t \tag{8}$$

$$t_{\frac{1}{2}} = \frac{1}{k_2[D]_0} \tag{9}$$

The BMG kinetic model, proposed by Behnajady, Modirshahla, and Ghanbery, is a mathematical model that describes the kinetics of Fenton-based processes in the presence of aromatic mediators, reducers, and non-reducers. This model has been used to evaluate the decolorization kinetics of Bismarck Brown (BBY) dye oxidized by Fenton processes (Fe^{2+}/H_2O_2, Fe^{3+}/H_2O_2) in the presence of aromatic mediators, reducers, and non-reducers [105]. The model has been shown to be effective in describing the kinetics of BBY decolorization and has been used to investigate the effect of temperature on the oxidation of BBY by Fenton processes [106]. The BMG kinetic model indicates the effect of decomposition by products on the oxidation reaction.

The BMG model expressed by Behnajady *et al.* [105] is shown in equation (10):

$$\frac{[D]_t}{[D]_o} = 1 - \frac{t}{m+bt} \tag{10}$$

The linearized form of the BMG model in Equation (10) can be expressed as

$$\frac{t}{1-\frac{[D]}{[D]_o}} = m + bt \tag{11}$$

In this model, a plot of $t/(1 - [D]/[D]_o)$ versus t results in a straight line with an intercept m and a slope b, where m and b are two constants concerning the initial reaction rate and maximum oxidation capacity, respectively, of the BMG model. This indicates the relationship between the concentration of the organic contaminant and the reaction rate [107].

The **efficiency of photodegradation** was calculated by using equation (12).

$$Degradation\ \text{Efficiency} = \frac{A_0 - A_t}{A_0}\ x\ 100 \quad \text{or} \frac{[D]_0 - [D]_t}{[D]_0}\ x\ 100 \tag{12}$$

where A_0 is the absorbance before degradation and A_t is the absorbance of the dye at time t, on degradation OR, $[D]_o$ is the initial concentration of the dye solution (mg L^{-1}) and $[D]_t$ is the concentration of the dye solution (mg L^{-1}) after a certain amount of irradiation. The half-life of dye degradation by biosynthesized NPs is determined by taking the point where $[D]/[D]_o$ verses $(1 – [D]/[D]_o) \times 100\%$ of the curve crossover point [108].

CHAPTER THREE

MATERIALS AND METHODS

3.1. Chemicals and Reagents

In thesis study, zinc nitrate hexahydrate [$Zn(NO_3)_2.6H_2O$] (purity 99.9%, CHD, India) and urea [$CO(NH_2)_2$] (99.5%, Blulux, India) were utilized as dopant metal ion precursors for zinc and nitrogen, respectively. Copper sulfate pentahydrate ($CuSO_4.5H_2O$, 99.9% purity, Ranchem, Turkey) was used as the metal oxide precursor. Sodium hydroxide (NaOH) (99%, Shraddha Associates (GUJ), India) and hydrochloric acid (HCl) (99%, Altiras, USA) were used for pH adjustment. Methylene blue stain, [$C_{16}H_{18}ClN_3S.H_2O$] (AR, Blulux, India), a cationic dye, was chosen as the organic pollutant. Ethanol [CH_3OH] was used to wash the nanocatalyst during recycling. All chemicals and reagents used for the photocatalytic degradtion study were of analytical grade. Deionized water was used to prepare all necessary solutions for washing purposes throughout the experiment.

3.2. Equipments and Instruments

An electric grinder (national) was used for powdering, and an electronic balance (Sartorius AG, Germany) was used to measure the mass of chemicals and objects. A muffle furnace (INSIF, India, Ho) was utilized for the calcination of the biosynthesized CuO, N-CuO, Zn-CuO, and N-Zn-codoped CuO nanoparticles. A pH meter (CG 841, Germany), magnetic stirrer hot plate (INSIF, H-359), and centrifuge (Labofuge 200, Germany) were used for pH adjustment, stirring and heating, and centrifugation, respectively. Whatman no. 1 filter paper (made in India) was used to filter the extract. A desiccator (Bo MEX, USA) and a refrigerant (Standard Laboratory, Thermo Fisher Scientific Inc., USA) were used to preserve the biosynthesized nanoparticles and PA plant extract for subsequent analysis. An UV–Vis spectrophotometer (SM-1600 spectrophotometer) was utilized for absorbance measurement. Common laboratory equipment and apparatuses were used for multiple purposes.

3.3. Sample Collection Site

Fresh leaves of *Pycnostachys Abyssinica* Fresen were collected from Kawo Koyisha, Wolaita, Ethiopia. Kawo Koyisha is a district in the Wolaita Zone, which is located approximately 60 km away from Wolaita Soddo, the capital of the Wolaita Zone and

Southern Ethiopia Regional State, and is approximately 390 km from Addis Ababa, the capital of Ethiopia.

3.4. Preparation of *Pycnostachys Abyssinica* Fresen Extract

Fresh and healthy leaves of *Pycnostachys Abyssinica* (PA) Fresen plants were collected from Kawo Koyisha, Wolaita, Ethiopia, and thoroughly cleaned with running tap water to remove dust particles, followed by deionized water and air drying at room temperature to remove residual moisture. The dried leaf was ground using a mechanical grinder, followed by packing in airtight glassware. The extraction was carried out by placing 10 g of powdered *Pycnostachys Abyssinica* Fresen leaves in a 250 mL Erlenmeyer flask containing 100 mL of deionized water and boiling at 80 °C for 20 min until the color changed. Then, the plant extract was filtered twice through a Whatman filter, as shown in Figure 14. Finally, the clear PA extract was stored in tightly sealed dark containers and preserved at 4 °C for further use [109].

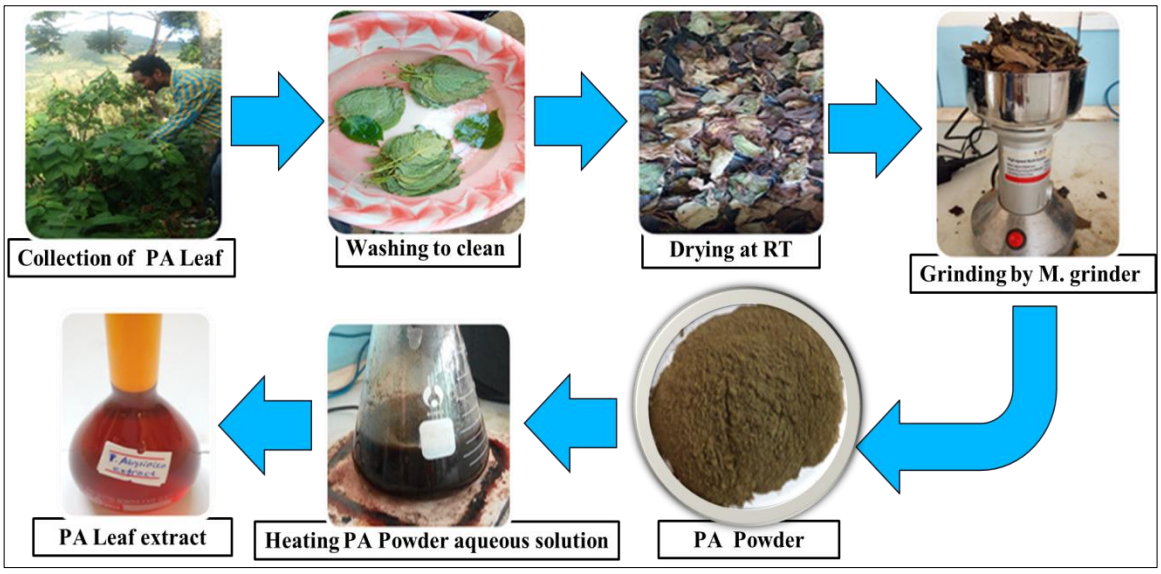

Figure 14: Flow diagram of PA leaf extract

3.5. Biosynthesis of Pure, Doped, and Codoped CuO NPs

3.5.1. Biosynthesis of CuO NPs

The experimental procedure reported in literatures [107, 108] was slightly modified to follow the biosynthesis of copper oxide nanoparticles. Briefly, 80 ml of 0.1 M $CuSO_4.5H_2O$ was measured and placed in a 500 ml beaker. Subsequently, 20 ml of PA aqueous extract was added to the beaker and thoroughly mixed using a magnetic stirrer. Next, 0.1 M sodium hydroxide was carefully added dropwise until the pH reached 8,

resulting in the appearance of a deep green color. The mixture was stirred continuously using a magnetic stirrer at 80 °C until the color was changed from deep green to dark brown and precipitate was observed. After the waiting a few minute, the precipitate at the bottom of the beaker formed a paste-like brown–black product. This product was transferred to a ceramic crucible and calcined in a preheated muffle furnace at 400 °C for 2 hours to ensure high crystallinity and eliminate organic impurities. Subsequently, the brown colored nanoproduct was allowed to cool to room temperature and ground in an agate mortar to obtain a fine nanopowder, as shown in Figure 15. Finally, the biosynthesized CuO NPs were transferred to a sample vial, labelled, and stored in a dissector for further experimentation.

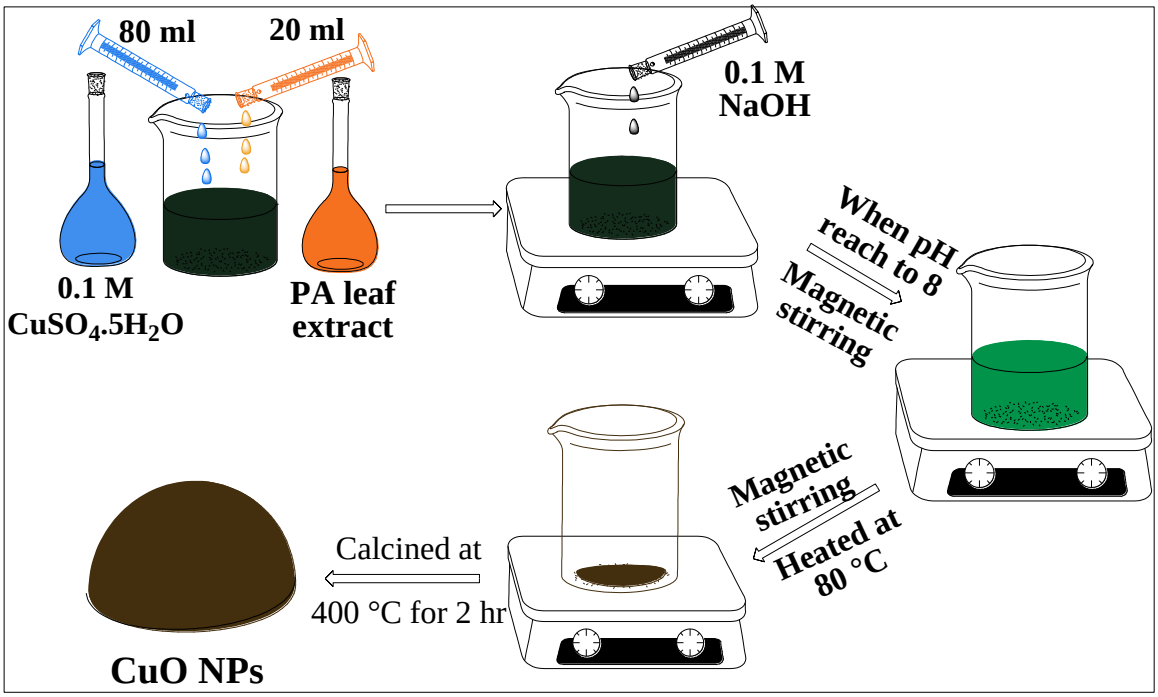

Figure 15: Flow diagram of the biosynthesis of CuO NPs

3.5.2. Biosynthesis of N-CuO NPs and Zn-CuO NPs

The dopant concentration composition for the biosynthesis of N-CuO NPs and Zn-CuO NPs, which refers to the ratio of dopant source to host copper oxide source in the biosynthesis solution, was calculated. In this case, the N and Zn dopant sources are urea and zinc nitrate, respectively, which are added to the ongoing copper oxide NPs to modify their properties. The equation "**grams of x% dopant source = x% multiplied by grams of host copper oxide source**" in 20/80 mL of PA extract/0.1 M copper sulfate biosynthesis solution was employed to determine the weight of the dopant source for the

biosynthesis of 1%, 3%, 6%, and 10% doped CuO NPs with each dopant. The calculated dopant concentration composition is presented in Table 3.

Table 3: Dopant concentration composition: gram x% dopant source = (x%)(gram of host copper oxide source in 20/80 mL of PA extract/0.1M copper sulphate biosynthesis solution)

Concentration of dopant sources (w/w %)	Concentration of dopant (gram)	Conc. composition of dopant to copper oxide (w/w)	Dopant of concentration of biosynthesized NPs
0% dopant	0	0:2	Pure CuO NPs
1% Urea	0.02	0.02:2	1% N-CuO NPs
3% Urea	0.06	0.06:2	3% N-CuO NPs
6% Urea	0.12	0.012:2	6% N-CuO NPs
10% Urea	0.2	0.2:2	10% N-CuO NPs
1% $Zn(NO_3)_2$	0.02	0.02:2	1% Zn-CuO NPs
3% $Zn(NO_3)_2$	0.06	0.06:2	3% Zn-CuO NPs
6% $Zn(NO_3)_2$	0.12	0.012:2	6% Zn-CuO NPs
6% $Zn(NO_3)_2$	0.2	0.2:2	10% Zn-CuO NPs

The procedure described in the literature [32] was slightly improved to biosynthesize nitrogen and Zinc doped copper oxide nanoparticles. Initially, 2 g (0.1 M) of $CuSO_4 \cdot 5H_2O$ was dissolved in 80 ml deionized water in a 500 ml beaker. Then, 20 ml of PA aqueous extract was added to the beaker and mixed well using a magnetic stirrer. Subsequently, 0.1 M sodium hydroxide was added dropwise until the pH reached 8, resulting in a deep green coloration. For the biosynthesis of 1% N-CuO NPs, 0.02 g of urea was added to the foregoing solution (Table 3). The mixture was stirred continuously using a magnetic stirrer at 80 °C until the color was changed from deep green to gray-brown and precipitate was observed. After the waiting a few minute, the precipitate at the bottom of the beaker formed a paste-like gray-brown product. This product was transferred to a ceramic crucible and calcined in a preheated muffle furnace at 450 °C for 2 hours to ensure high crystallinity and eliminate organic impurities. Subsequently, the gray-brown colored nanoproduct was allowed to cool to room temperature and ground in an agate mortar to obtain a fine nanopowder, as shown in Figure 16. Finally, the biosynthesized 1%N-CuO NPs were transferred to a sample vial, labelled, and stored in a dissector for further experimentation. The same procedure was used to biosynthesize 3%, 6%, and 10% N-CuO

NPs as well as 1%, 3%, 6%, and 10% Zn-CuO NPs, as per the dopant concentration ratios specified in Table 3.

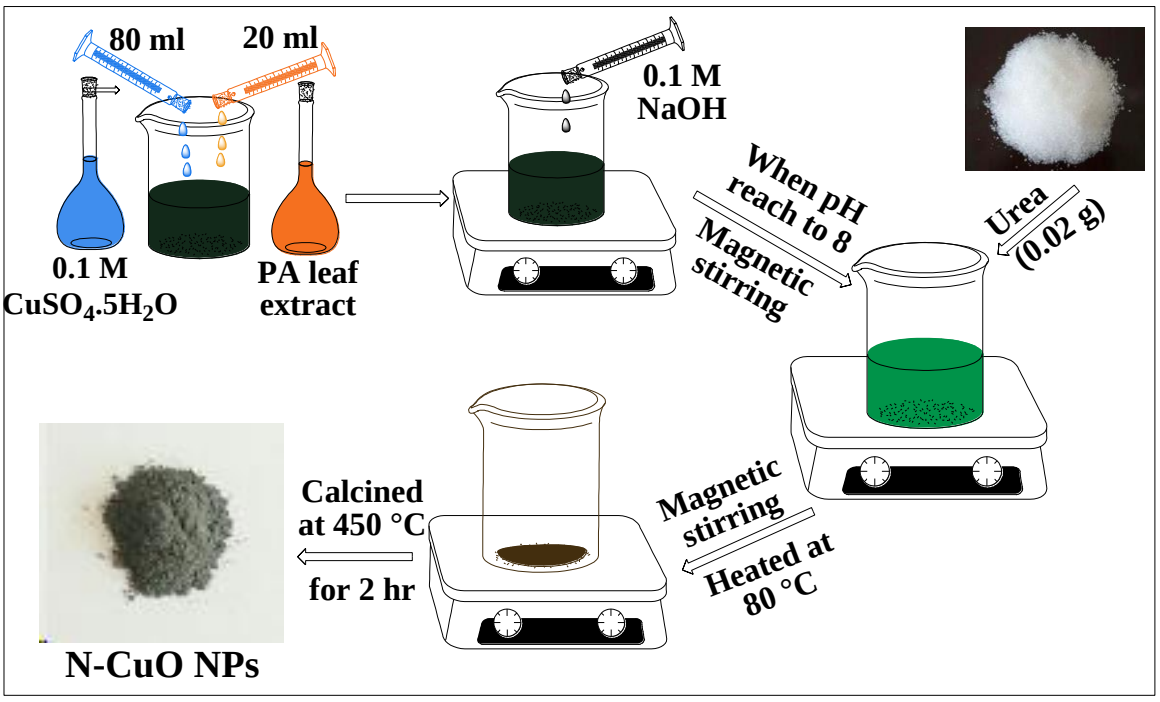

Figure 16: Flow diagram of the biosynthesis of N-CuO NPs

3.5.3. Optimization of Dopant Concentration for Codoped CuO NPs

A 50 mL solution of 5 ppm MB dye in aqueous solution was placed in eight 100 mL beakers, and 80 mg of biosynthesized 1%, 3%, 6%, and 10% N- and Zn-doped CuO nanoparticles were added to different beakers as photocatalysts. Next, the pH was adjusted to 11, and the mixture was magnetically stirred in the dark for 30 minutes. After 30 minutes, the beaker containing the mixture was exposed to direct sunlight irradiation with the highest light intensity from 11:30 a.m. to 3:00 p.m. for one hour. Following the photocatalysis reaction, the mixture was then centrifuged to remove all nanocatalysts from the solution, and the absorbance of the MB solution before and after degradation was recorded at 665 nm using a UV–Vis spectrophotometer. The degradation efficiency of the biosynthesized 1%, 3%, 6%, and 10 % N- and Zn-doped CuO nanoparticles was evaluated based on Equation 12. The best-performing dopant concentration photocatalyst was identified as 3% dopant concentration for both urea and zinc nitrate were used as the optimized dopant concentration for codopant CuO NP synthesis [111].

3.5.4. Biosynthesis of N–Zn–Codoped CuO NPs

For the synthesis of N-Zn-codoped CuO NPs, 2 g (0.1 M) of $CuSO_4 \cdot 5H_2O$ was dissolved in 80 ml deionized water in a 500 ml beaker. Then, 20 ml of PA aqueous extract was added to the beaker and mixed well using a magnetic stirrer. Subsequently, 0.1 M sodium hydroxide was added dropwise until the pH reached 8, resulting in a deep green coloration. To the foregoing solution, the optimized dopant concentration of urea (0.06 g) and zinc nitrate (0.06 g) were added. The mixture was stirred continuously using a magnetic stirrer at 80 °C until the color was changed from deep green to brown and precipitate was observed. After the waiting a few minute, the precipitate at the bottom of the beaker formed a paste-like gray-brown product. This product was transferred to a ceramic crucible and calcined in a preheated muffle furnace at 500 °C for 2 hours to ensure high crystallinity and eliminate organic impurities. Following calcination, the sample was allowed to cool and ground again in an agate mortar to obtain a fine nanopowder, as shown in Figure 17. Finally, the biosynthesized N–Zn–codoped CuO nanoparticles were transferred to a sample vial, labelled, and stored in a dissector for further experimentation.

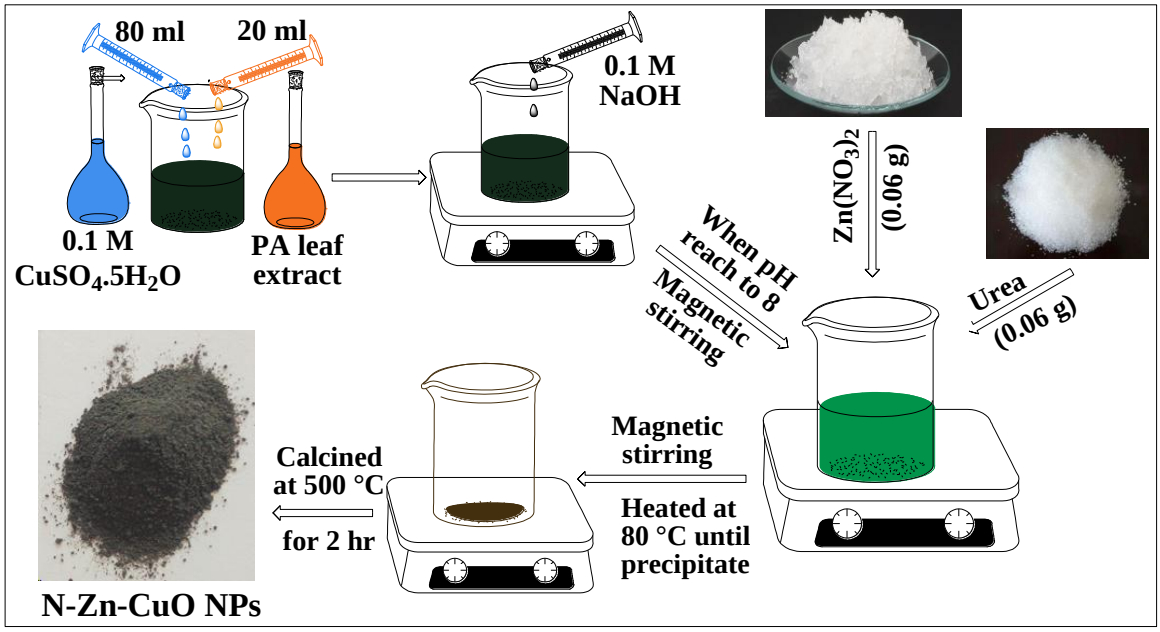

Figure 17: Flow diagram of the biosynthesis of N-Zn-CuO NPs

3.6. Characterization of Nanoparticles

The optical properties of biosynthesized CuO, N-CuO, Zn-CuO, and N-Zn-codoped CuO nanoparticles were investigated using UV-Vis diffuse reflectance spectroscopy (T80

UV/VIS spectrophotometer, PG instrument Ltd.) in the wavelength range of 200–800 nm at Central laboratory of Sciences, Hawassa University. The functional groups and metal-oxygen matrix present in the biosynthesized nanoparticles were characterized using Fourier transform infrared spectroscopy (FT-IR) at Central laboratory of Sciences, Hawassa University, with a Perkin Elmer FT-IR BX spectrophotometer, recording spectra in the range of 4000–400 cm−1 with samples prepared as KBr pellets.

The morphological structure and size distributions of the biosynthesized nanoparticles were analysed through scanning electron microscopy (SEM) images at Laboratory of Applied Biology, Adama Science and Technology University. Particle size distribution was calculated using J software based on the SEM images. The crystalline structure and size of biosynthesized nanoparticles were determined through X-ray diffraction analysis (XRD-7000, Shimadzu Corporation, Japan) at Laboratory of Material Sciences, Adama Science and Technology University, using Cu Kα = 1.5406 Å as the X-ray source, with a voltage of 40 kV and a current of 30 mA in the 2θ range of 10° to 80°.

3.7. Photocatalytic Degradation of MB

The photocatalytic degradation of MB was carried out following the procedures described in literatures [3] and [11] with slight modifications. A 50 mL solution of 5 ppm MB dye in water was placed in 100 mL beakers, and 80 mg of biosynthesized CuO NPs was added as a photocatalyst. The pH was then adjusted to 11, and the mixture was magnetically stirred in the dark for 30 minutes. After 30 minutes, the beaker containing the mixture was exposed to direct sunlight irradiation with the highest light intensity from 11:30 a.m. to 3:00 p.m. because the outside temperature was 29–33 °C, and the average solar radiation was 2.11 kWh $m^{-m}Wd^{-m}$ [108]. Following the photocatalysis reaction, the mixture was centrifuged to remove all nanocatalysts from the solution, and the absorbance of the MB solution before and after degradation was recorded at 665 nm using a UV–Vis spectrophotometer. The degradation efficiency of the biosynthesized CuO NPs was evaluated based on Equation 12. The same experimental procedure was repeated to optimize the key parameters affecting the photocatalytic activity by varying the photocatalyst dosage (10, 40, 80, 120, 160, 200, and 240 mg), initial concentration of MB dye (1, 5, 10, 15, 20, 25, and 30 ppm), and pH 2–14 (keeping all other parameters constant to investigate the optimum of one parameter by varying as stated). Similarly, the effect of the reaction time for both the dark reaction (stirring time in the dark room) and the light

reaction (exposure time to direct sunlight) was investigated by withdrawing 5 mL aliquots of the mixture from the ongoing adsorption and photocatalysis reaction at every 10 minutes, while the reaction time for all other photocatalytic parameters remained constant at the determined optimal point. The same experimental procedure was repeated to evaluate the photocatalytic performance of biosynthesized N-CuO, Zn-CuO, and N-Zn-codoped CuO NP photocatalysts over MB degradation (see Appendix 9 for details).

3.8. Nanocatalyst Reusability and Stability Test

The photocatalytic activity of all biosynthesized nanoparticles was evaluated under optimized conditions. After the completion of the reaction cycle, the nanocatalyst was separated by centrifugation from the reaction mixture, followed by washing with ethanol and deionized water. Subsequently, the nanocatalyst was dried at 80 °C in an oven for two hours to ensure the complete removal of residual moisture [112]. The reusability of the dried nanocatalyst was then tested by performing four consecutive cycles under optimized experimental conditions for photocatalytic degradation. After each cycle, the photocatalyst was reloaded with a consistent concentration and amount of fresh MB dye to evaluate its stability and efficiency over multiple uses (see Appendix 9 for details).

3.9. Kinetic Study for Photocatalytic Degradation

The photocatalytic degradation kinetics of MB dye were investigated using four kinetic models: pseudo-zero order, pseudo-first order, pseudo-second order, and the BMG model developed by Behnajady *et al.*, [105]. The degradation was studied at various exposure times ranging from 10 to 60 minutes, with 10-minute intervals. The experiments were conducted at optimized concentrations while keeping all other parameters constant. Linearized equations for zero-order kinetics, first-order kinetics, second-order kinetics, and the BMG model (equations (2), (5), (8), and (11), respectively) were employed in the analysis.

CHAPTER FOUR

RESULTS AND DISCUSSION

4.1. Visual Inspection for Biosynthesis of CuO NPs

Nanoparticles display a variety of colours during biosynthesis [4], attributed to the reaction of multiple phytochemicals in the plant extract with metal ions, transforming them into nanoparticles. As shown in Figure 18, during the biosynthesis of CuO nanoparticles, a dull dark-brown color was observed when an aqueous solution of blue copper sulphate reacted with brown-red PA extract. This indicates the reduction of Cu^{2+} ions to Cu^{0} during the formation of the copper metal-phytochemical complex through nucleation (Eq. 14). Subsequently, the color of the solution turned to deep green when the pH was adjusted to 8, indicating the formation of CuO-phytochemical complexes (Eq. 15). Finally, the solution turned brown-dark and formed a paste-like nanopowder after heating the reaction at 80 °C until the change (Eq. 16), confirming the formation of stable CuO NPs and the completion of the nanoparticle synthesis process. Similarly, as reported by Worku *et al*., [110], Karuppannan *et al*., [113], Takele *et al*., [109] and Narayanan *et al*., [114], the color changes have been observed, when the phytochemicals present in the plant extracts initially form complexes with copper salts before reducing the amount of ions to create nanoparticles, where a blue solution turned green and eventually formed a dark brown precipitate after a certain reaction time using leaf extract of *Catha edulis*, *Cardiospermum halicacabum*, *Zingiber officinale Rhizome*, and *Thespesia populnea bark powder,* respectively.

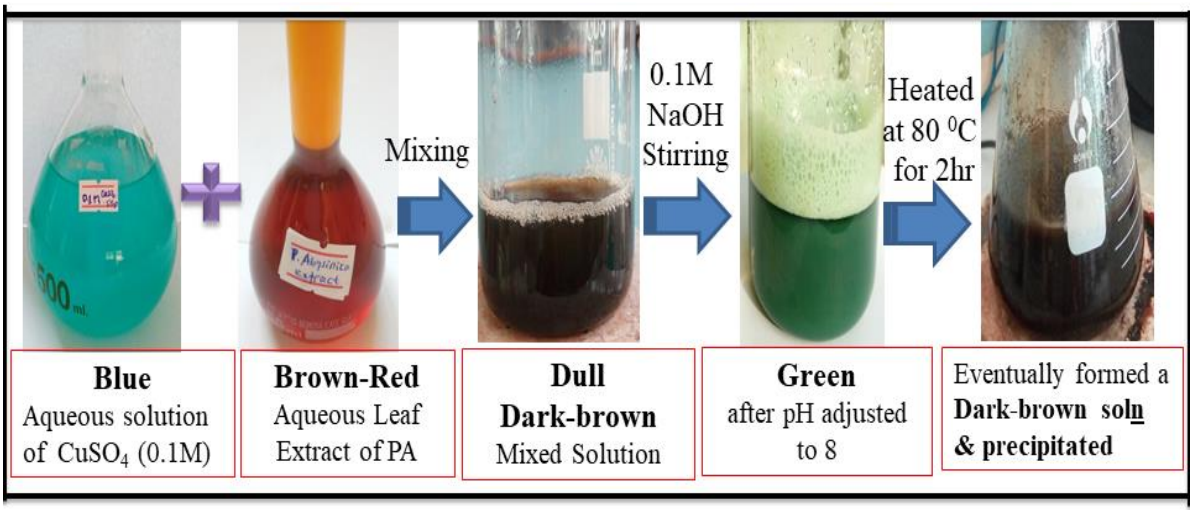

Figure 18: Visual observation of the biosynthesis of CuO NPs

The reduction of copper ions by biomolecules in plant extracts leads to the formation of CuO NPs [115]. The biosynthesis of pure CuO NPs can be explained through equations (13-15), which represent the probable mechanism involved in the process;

$$Cu^{2+} + \text{PA extract} \rightarrow [Cu^{2+}/\text{PA extract}] \quad \text{(Initiation)} \quad (13)$$

$$[Cu^{2+}/\text{plant extract}] \rightarrow [\text{Cu/Biomolecules}] \quad \text{(Reduction)} \quad (14)$$

$$[\text{Cu/Biomolecules}] \rightarrow \frac{NaOH}{Stirr} \rightarrow [\text{CuO/Biomolecules}] \quad \text{(Oxidation)} \quad (15)$$

$$[\text{CuO-Biomolecules}] \rightarrow \frac{stirr}{at\ 80\ oC} \rightarrow \text{CuO NPs} \quad \text{(stabilization)} \quad (16)$$

4.2. Characterization of the Biosynthesized Nanoparticles

4.2.1. UV–Vis Analysis

The UV–Vis spectral analysis of *Pycnostachys Abyssinica* extract yielded valuable insights into its electronic absorption properties, indicating the presence of various biomolecules. Figure 19 shows that the maximum absorbance of the *Pycnostachys Abyssinica* extract was observed at 210 nm, with additional minor peaks at 278 nm and 330 nm.

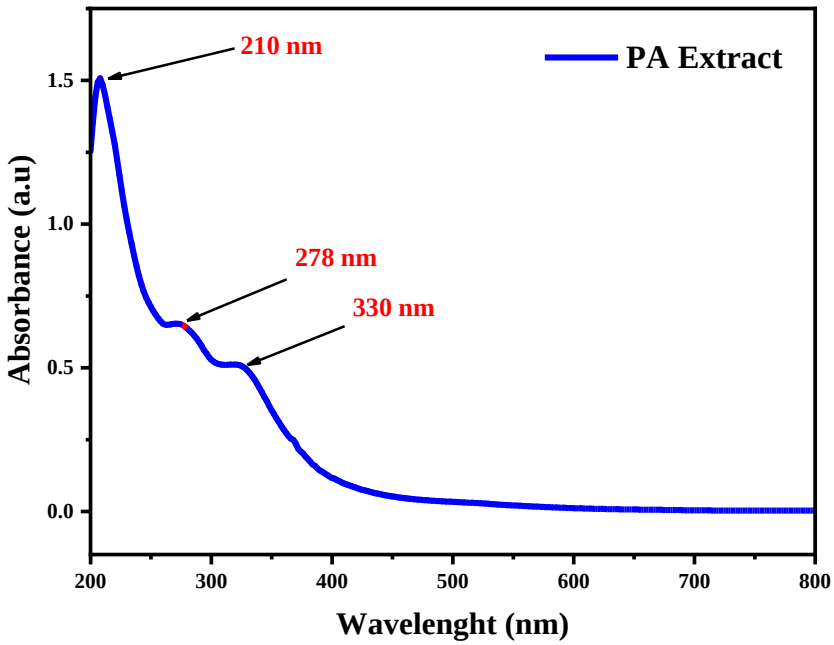

Figure 19: UV–Vis spectrum of *Pycnostachys Abyscinica*

The prominent peak at 210 nm is characteristic of protein and peptide bonds, which exhibit strong absorption in this region due to pi-bonding to pi-antibonding transitions

[116], suggesting the presence of amino acid derivatives or amides in the extract. The absorption peak at 278 nm is likely attributed to phenolic compounds, especially those with extended conjugation systems such as flavonoids and tannins. Furthermore, the peak at 330 nm may be associated with certain terpenoids or alkaloids, which typically display absorbance in this region owing to their intricate aromatic structures. These findings are consistent with the phytochemical screening of *Pycnostachys abyssinica*, which revealed the presence of alkaloids, flavonoids, glycosides, phenols, terpenoids, tannins, steroids, and acidic compounds, as previously reported [44]. This finding supports the potential use of the extract as a bioreducer and capping agent in the biosynthesis of pure CuO, N-CuO, Zn-CuO and N-Zn-CuO nanoparticles.

UV–Vis spectroscopy serves as a vital technique for identifying nanoparticle formation by detecting surface plasmon resonance (SPR) peaks and facilitating the estimation of their band gap energy. In this study, the successful synthesis of PA extract-assisted pure, metal-doped, nonmetal-doped, and codoped CuO nanoparticles (NPs) was validated through UV–Vis spectroscopy, which was utilized to assess their absorbance across the 200-800 nm wavelength range, as shown in Figure 20.

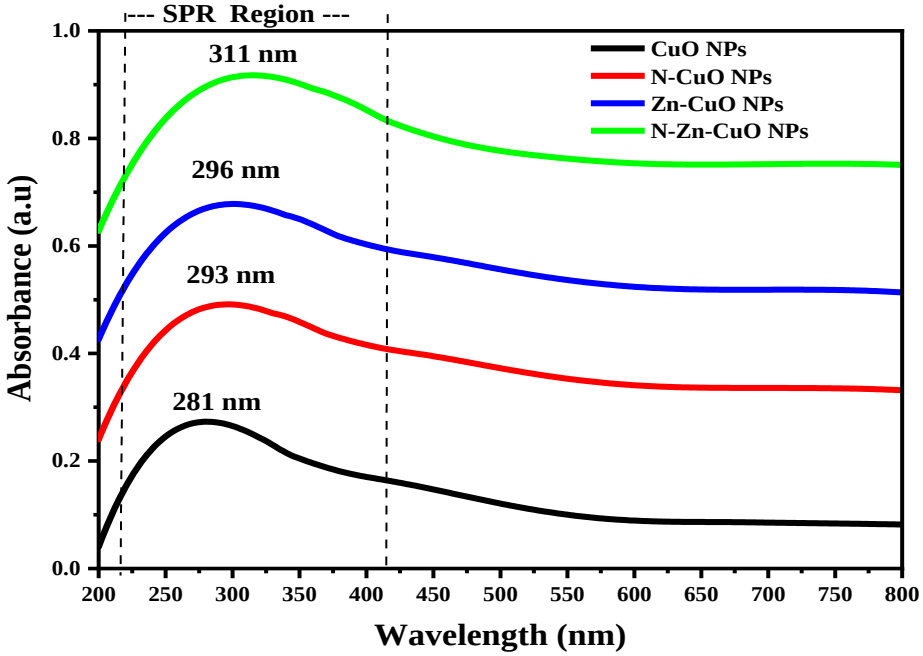

Figure 20: UV–Vis spectra of biosynthesized pure CuO NPs, N-CuO NPs, Zn-CuO NPs, and N-Zn-CuO NPs

The presence of broad absorption peaks at 240 to 350 nm with maximum absorption peaks at 281 nm, 293 nm, 296 nm, and 311 nm for CuO NPs, N-CuO NPs, Zn-CuO NPs, and N-

Zn-CuO NPs in the SPR region of the UV–Vis spectrum confirmed the formation of biosynthesized nanoscale entities, as depicted in Figure 20, and aligned well with previously reported CuO NP absorption peaks [118, 32, 83]. In comparison, the absorption peak of the pure CuO NPs was observed at 281 nm, as indicated in Figure 20. Notably, doping with N and Zn separately and codoping with both N and Zn in the lattice of CuO NPs caused a redshift in the peak position to the visible region, intensity broadening, and lower energy levels in the spectra of the N-CuO, Zn-CuO, and N-Zn-CuO NPs. This reveals the alteration of the optical and band gap properties of the CuO crystal lattice due to dopant incorporation [111].

The band gap energy of the biosynthesized nanoparticles was estimated through the application of the Tauc model [118]. The optical band gap can be determined by using the well-known Tauc relation from equation (17):

$$(\alpha h\nu)^n = A(h\nu - Eg) \tag{17}$$

where A is a constant related to the material, α is the absorption coefficient in cm^{-1}, hν is the photon energy in eV, Eg is the band gap energy in eV, and n is a constant that equals 2, 1/2, 2/3, and 1/3 for allowed direct, allowed indirect, forbidden direct, and forbidden indirect transitions, respectively. In this case, n = 2 is used for the determination of the optical band gap of the biosynthesized nanoparticles because of the good linearity of the model compared to that of the other models. The following formula [119] can be used to determine the band gap energy (E_g) of a material with corresponding to the absorption λ;

$$E_g\ (eV) = 1240/\lambda\ (nm) \tag{18}$$

where Eg is the band gap energy (eV) and λ is the wavelength in nm, corresponding to the absorption edge.

The optical band gap (E_g) values were determined by extrapolating the linear portion of the plots of $(\alpha h\nu)^2$ vs. hν to α = 0, as illustrated in Figure 21. The E_g values for pure CuO NPs, N-CuO NPs, Zn-CuO NPs, and N-Zn-CuO NPs were found to be 1.72 eV, 1.44 eV, 1.29 eV, and 1.07 eV, respectively. The energy gap (Eg) values of the pure, doped, and codoped CuO nanoparticles (NPs) fall within the commonly expected range of 1.2 eV to 1.9 eV. This indicates that there is no significant influence of quantum confinement and suggests successful controlled synthesis [20, 121]. This finding is consistent with the research conducted by [3, 94, 110], who have also reported similar Eg values for CuO nanoparticles in their previous studies.

As expected, the Tauc plot shown in Figure 21 confirmed a reduction in the band gap after doping and codoping on the crystal lattice of CuO NPs. For the pure CuO NPs, the band gap was calculated to be 1.72 eV, while this value decreased to 1.44 eV, 1.29 eV, and 1.07 eV for the N-doped, Zn-doped, and N-Zn-codoped CuO NPs, respectively.

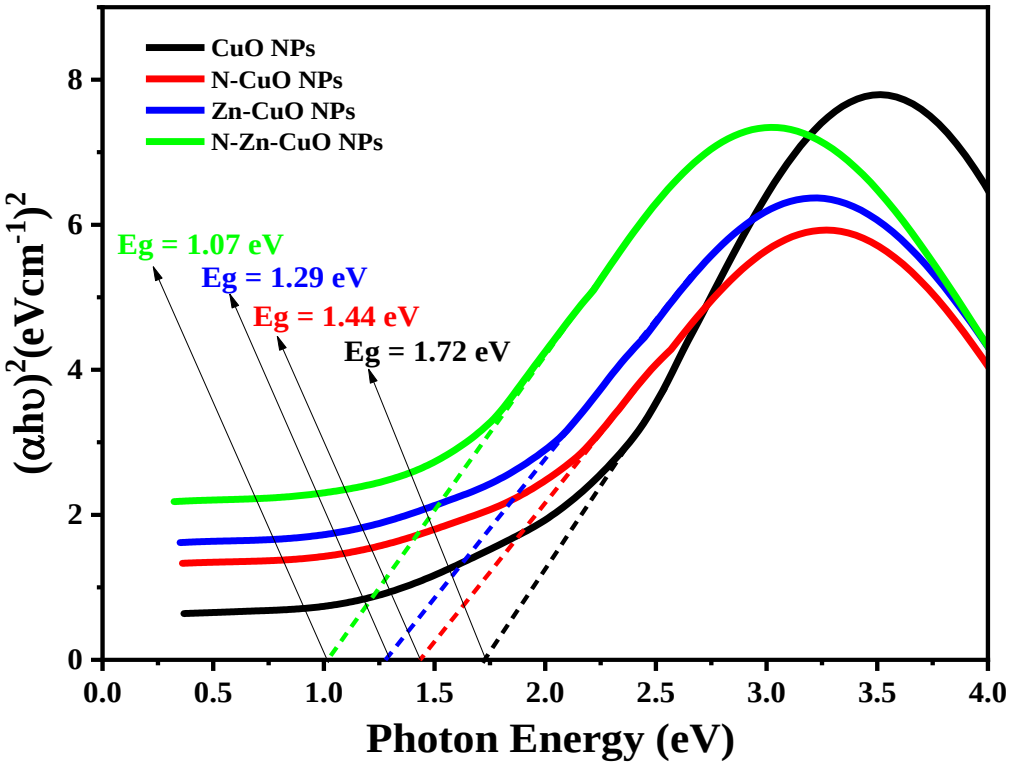

Figure 21: Tauc plot of pure CuO NPs, N-CuO NPs, Zn-CuO NPs, and N-Zn-CuO NPs

Significantly, these changes suggest the formation of new electronic states between the valence and conduction bands, leading to bandgap engineering with the successful incorporation of dopants into CuO NPs. Notably, the modified optical properties, particularly in the case of N-Zn codoping, may result in increased extinction of electron-hole pairs, which is expected to enhance photocatalytic activity compared to that of all other nanoparticles. This enhancement could enable the utilization of visible light to degrade toxic dyes present in industrial effluents. Similarly, alterations in optical properties and bandgap reductions have been analysed using UV–Vis spectroscopy in studies involving doping and codoping of CuO nanoparticles with Ag-Zn [34]. These findings highlight the potential for tailoring the optical properties and band gaps of CuO nanoparticles through doping and codoping strategies, which could have significant implications for various applications in photocatalysis and environmental remediation.

4.2.2. FT-IR Analysis

FT-IR analysis was conducted to identify the functional groups of the biomolecules and metal-oxygen matrix involved in the biosynthesis of the pure CuO NPs, N-CuO NPs, Zn-CuO NPs, and N-Zn-CuO NPs. This technique provides valuable information on the interactions between phytochemicals present in plant extracts and the metal ions responsible for the production and capping of biosynthesized nanoparticles. The individual band intensities observed in the PA extracts and their corresponding nanoparticles confirmed these interactions. The FT-IR spectra of the PA leaf extract, as shown in Figure 22, revealed the presence of several compounds. The appearance of broad peaks around 3443 cm^{-1} indicated the presence of -OH stretching and intra/intermolecular H-bonds of polyphenolic compounds [121]. Peaks at 2933 and 2842 cm^{-1} confirmed the presence of methyl and methylene C-H stretching, while absorption bands at 1738 and 1634 cm^{-1} suggested the existence of amine (N-H) and carbonyl (C=O) groups. Similarly, the peaks at 1411, 1264, 1054, and 545 cm^{-1} represented the -C-H bending alkene group, C-OH bending phenol group, and C-C bending functional group, respectively, potentially serving as stabilization, capping, and bioreducing agents in the synthesis of pure, doped and codoped CuO NPs [122].

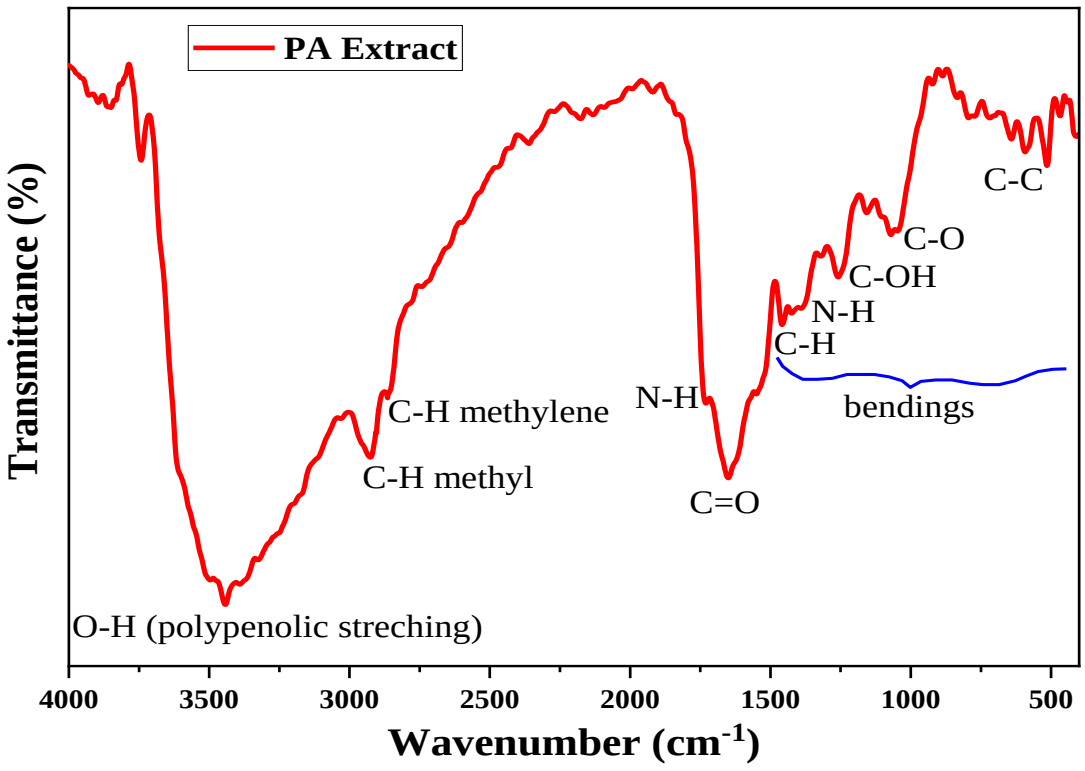

Figure 22: FT-IR spectra of *Pycnostachys Abyssinica* leaf extract

The functional groups, Cu-O bonds, doping and codoping interactions CuO matrix caused vibrational frequencies of the biosynthesized pure, doped, and codoped CuO NPs were identified through analysis of the FT-IR spectra, as depicted in Figure 23. The FT-IR spectra of CuO NPs, N-CuO NPs, Zn-CuO NPs, and N-Zn-CuO NPs exhibited characteristic peaks at 3436, 3412, 3428, and 3428 cm^{-1} corresponding to the stretching vibration of O–H, indicating the presence of intra/intermolecular H-bonds of polyphenolic compounds; strong peaks at 1129, 1117, 1119, and 1113 cm^{-1} confirmed to the C–O of phenol groups; peaks at 1675, 1670, 1663 and 1626 cm^{-1} may be indicating the C=O stretch of amide; and peaks at 1519, 1510, 1515, and 1503 cm^{-1} possibly representing the presence of primary N–H bending corresponding to the biomolecules from the PA extract during biosynthesis, respectively [123, 124]. The peaks at 784, 617, and 494 cm^{-1} for pure CuO NPs; at 760, 610, and 461 cm^{-1} for N-CuO NPs; at 780, 611, and 486 cm^{-1} for Zn-CuO NPs; and at 620, 529, and 459 cm^{-1} for N-Zn-CuO NPs corresponded to the characteristic stretching vibrations of the Cu–O bond in monoclinic CuO NPs along the (111) direction in the CuO crystal phase. This confirms the successful biosynthesis of these Cu-O nanoparticles, which is in agreement with previous literature [13, 125].

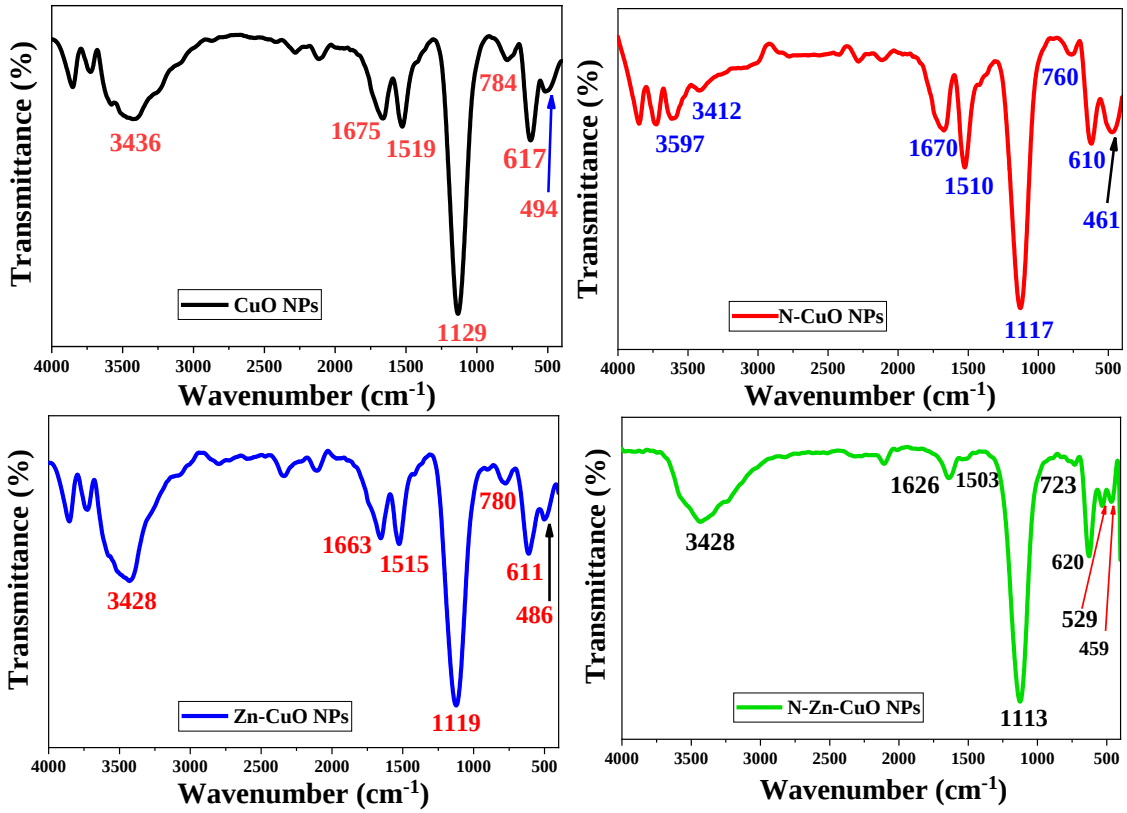

Figure 23: FT-IR spectra of the biosynthesized pure CuO NPs, N-CuO NPs, Zn-CuO NPs and N-Zn-CuO NPs

Notably, compared with those of pure CuO NPs, the FT-IR spectra of N-CuO NPs, Zn-CuO NPs, and N-Zn-CuO NCs exhibited a redshift (lower frequencies) and broadening of the characteristic peaks of CuO, indicating the incorporation of N, Zn dopants, and codopants on the surface of the CuO lattice [125]. The observed redshift in the position of the Cu-O absorption bands with N doping can be attributed to differences in bond strength arising from the substitution of nearly the radii and low electronegativity (EN) of N in the oxygen vacancy defects of CuO. With Zn doping, the redshift may be due to the substitution of Cu^{2+} ions with Zn^{2+} in the CuO lattice structure, resulting in the strengthening of the Cu-O bond [126]. The observed redshift of the Cu-O characteristic peaks from 784 to 620 cm^{-1}, 617 to 529 cm^{-1}, and 494 to 459 cm^{-1} confirmed the successful codoping of N and Zn ions into the CuO lattice [34].

4.2.3. SEM Analysis

The morphology, microstructure, particle size, and distribution of the biosynthesized pure CuO NPs, N-CuO NPs, Zn-CuO NPs, and N-Zn-CuO NPs were analysed using SEM and J software at a magnification scale of 5 µm, as depicted in Figure 24a-d, to investigate how dopants interact with the CuO matrix, influencing the morphology and size of the nanoparticles. Figure 24a illustrates biosynthesized pure CuO NPs with rhombus and diamond-like shapes, exhibiting uniformity in size with an average diameter of 2.25 µm. This uniformity suggests a controlled synthesis process and anisotropic growth of monoclinic CuO crystals composed of alternately arranged O^{2-} and Cu^{2+} ions along the (111) direction in the CuO crystal phase, resulting in well-defined shapes and sizes [127]. Similar morphological shapes with high-density polydispersed spherical CuO NPs have been reported when synthesized using *Thespesia populnea* [114].

The morphology of the N- and Zn-doped CuO NPs showed elongated and distorted rhombus and diamond-like particles with rough surfaces, exhibiting visible clustering of various sizes and creating a dense structure with diameters of 2.49 µm and 3.48 µm, respectively (Figure 24b and c). This change in morphological structure and increase in particle size were attributed to the distortion of the CuO crystal lattice upon N and Zn incorporation. Compared to N-CuO NPs, Zn-CuO NPs exhibited small agglomerated particles, with smaller particles appearing to be attached to the surfaces of larger ones, potentially introducing paramagnetic behaviour with a weak ferromagnetic nature at low fields (Figure 8c) [127, 128].

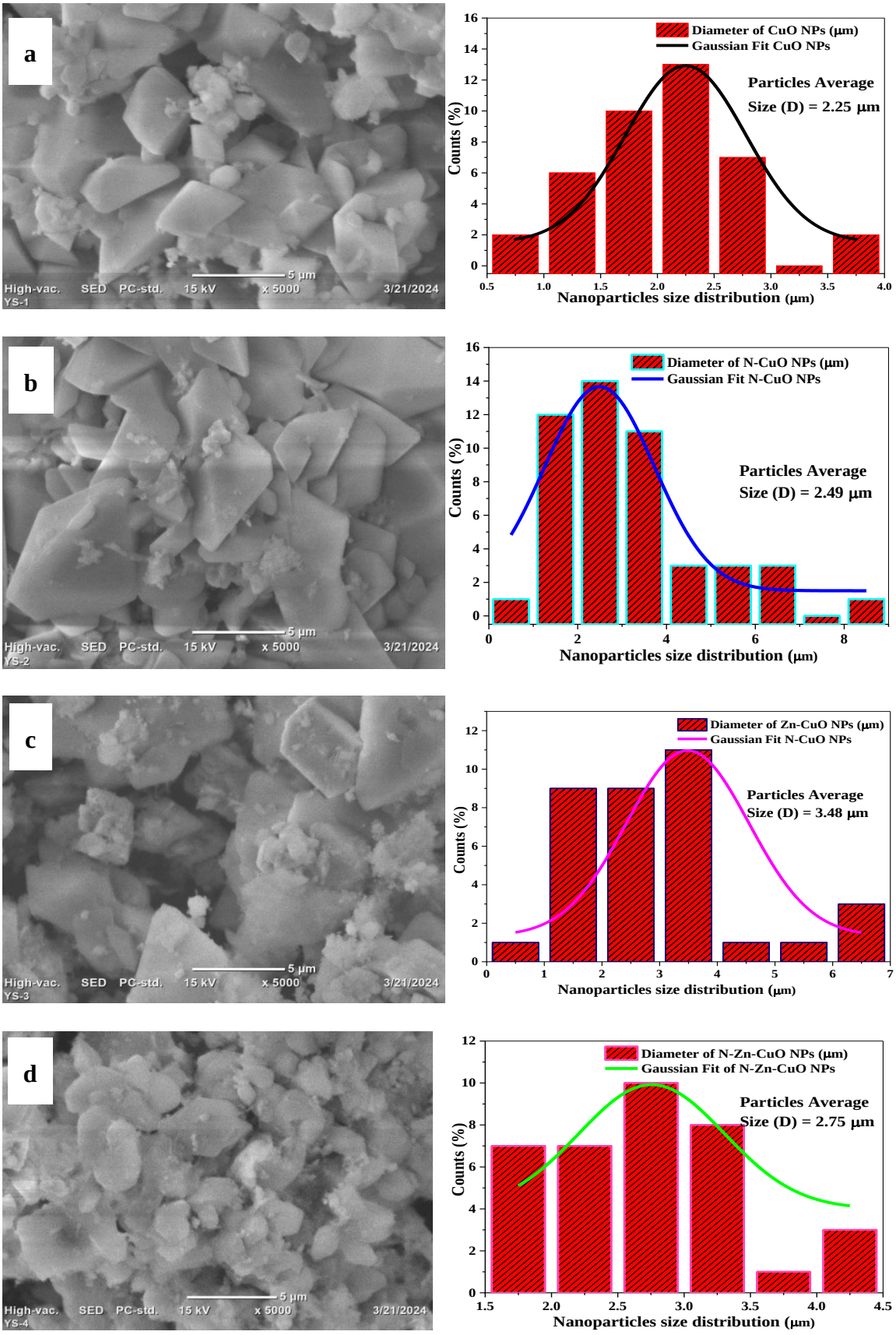

Figure 24: SEM image and histogram of particle size distribution analysis for the biosynthesized pure CuO NPs (a), N-CuO NPs (b), Zn-CuO NPs (c), and N-Zn-CuO NPs (d)

Figure 24d displays the N-Zn-CuO NPs, where codoping evidently altered the morphological shape and size due to the synergistic effect of both dopants. The particles became agglomerated, more irregular and clustered, with an average size of 2.75 µm. This increase in size and change in morphology could be attributed to the introduction of nitrogen and zinc into the CuO lattice, influencing the nanoparticle growth process [111].

4.2.4. XRD Analysis

The crystal structures and phases of the pure CuO NPs, N-CuO NPs, Zn-CuO NPs, and N-Zn-codoped CuO NPs were determined through X-ray diffraction (XRD) analysis. The combined XRD patterns for all the samples are presented in Figure 25a. Distinct diffraction peaks were observed at 33.86°, 35.52°, 38.74°, 48.76°, 53.48°, 58.32°, 61.52°, 66.22°, 68.08°, 72.44°, and 75.24°, corresponding to the (110), (002), (111), (112), (202), (020), (113), (311), (220), (311) and (002) planes, respectively. These peaks closely match the standard JCPDS Card no. 00-048-1548 for monoclinic copper oxide, indicating the successful biosynthesis of CuO NPs and the effective modification of its lattice structure with appropriate dopants. No additional phases were detected in the XRD diffraction pattern, confirming the purity of the synthesized materials. The agreement between the experimental XRD data and the reference standard, along with the absence of impurities, supports the reliability of the crystallographic information obtained. Furthermore, the observed absorption bands in the FT-IR spectra discussed earlier align with the XRD results, providing complementary evidence for the structural characteristics of the synthesized nanoparticles.

As shown in Figure 25a, doping the CuO lattice with N, Zn, and codoping does not introduce an extra phase or significantly alter the peak locations. However, compared to the patterns of pure CuO nanoparticles, the patterns of doped and codoped CuO nanoparticles exhibit minor broadening of diffraction peaks, slight shifts in peak positions towards red and blue, and reduced intensity. These changes suggest lattice disorder and associated stresses resulting from the incorporation of dopant ions into the CuO lattice, as detailed in the enlarged Figure 25b. The enlarged diffraction peaks of the (002) and (111) planes for the pure CuO NPs, N-CuO NPs, Zn-CuO NPs, and N-Zn-codoped CuO NPs were analysed. The (002) and (111) peaks for N-doped CuO NPs shifted 0.03° and 0.04° towards lower 2θ values with increased broadening, suggesting nitrogen atom incorporation into the lattice. This substitution of N^{3-} ions (ionic radii = 1.71 Å) for O^{2-} (ionic radii = 1.32 Å) ions led to lattice distortion and increased microstrain, as discussed

by [126]. Conversely, the similar diffraction peak (002) and (111) of Zn-doped CuO NPs shifted 0.04° and 0.02°, respectively, towards higher 2θ values with increased broadening due to the replacement of a larger ionic radius of Zn^{2+} ions (0.74 Å) with a smaller ionic radius of Cu^{2+} ions (0.72 Å). This might be attributed to the tensile stress that affects the shift towards a lower angle and leads to anisotropic shrinkage of the lattice, leading to lattice distortion [128, 129].

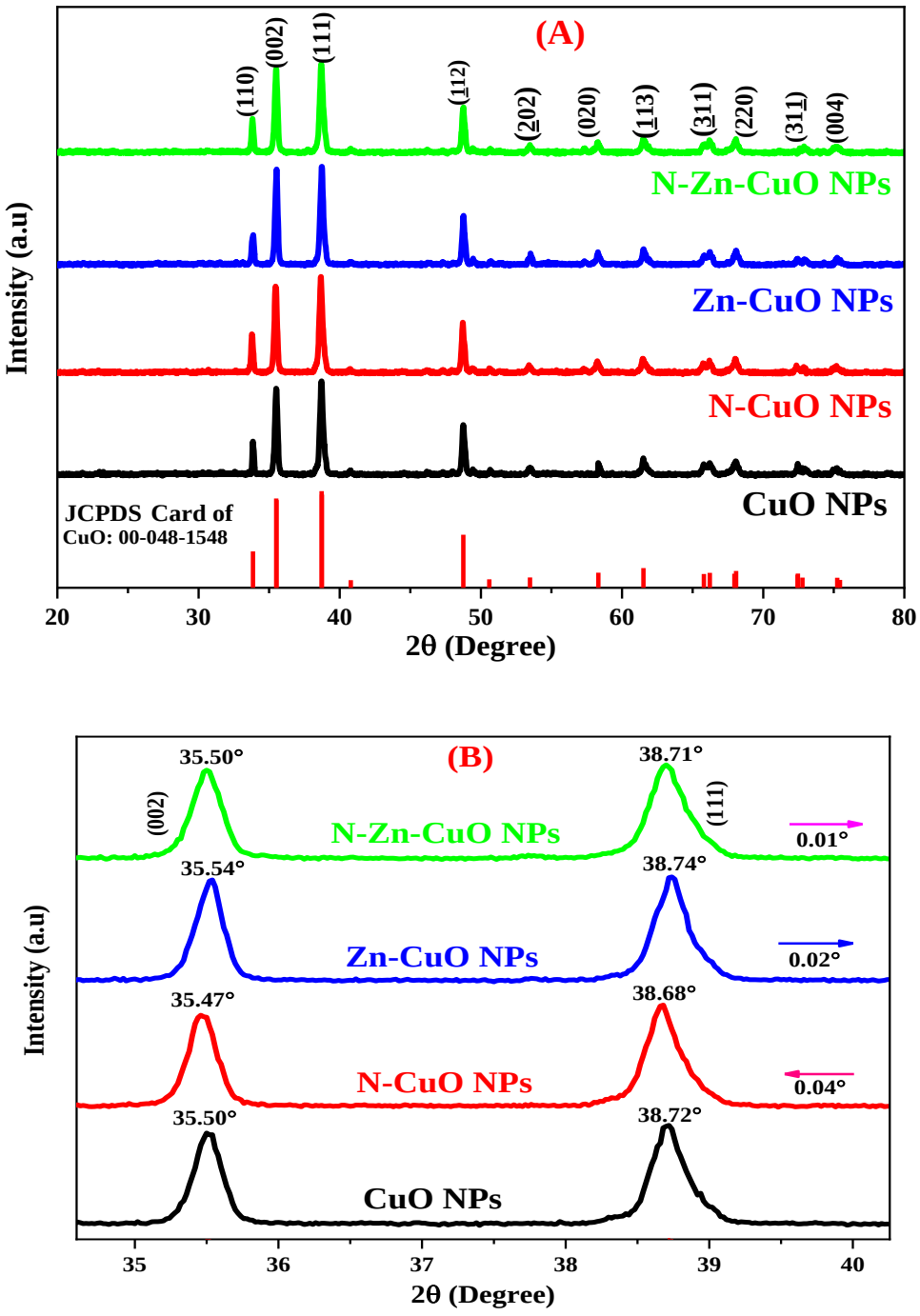

Figure 25: XRD patterns of pure, N-, Zn-doped and codoped CuO NPs (a) and Enlarged XRD pattern showing shifts in peak positions and peak sizes after doping (b)

Due to the combined effect of the codopant on the lattice of CuO, the XRD patterns of the (002) and (111) planes of the N-Zn-codoped CuO NPs were similar to those of pure CuO in terms of 2θ. However, the intensity of the peaks decreased and exhibited slightly broadening due to the addition of the dopants, thereby confirming the incorporation of N and Zn into the host CuO crystal lattice [128, 129].

The broadening of the diffraction peaks observed during doping and codoping was expected due to the decreased crystallite size. To confirm this, the crystallite sizes of the biosynthesized pure CuO NPs, N-CuO NPs, Zn-CuO NPs, and N-Zn-codoped CuO NPs were calculated using the Debye–Scherrer equation (19) as expressed by Patterson [131]. The full width at half maximum (FWHM) of the most intense diffraction peaks corresponding to the (110), (002), (111), and (112) planes were measured and are shown in Table 4.

$$D = \frac{K\lambda}{\beta\cos\theta} \tag{19}$$

where K is the Scherrer constant (0.9), λ is the wavelength of Cu Kα radiation (1.54056 nm), β is the full width at half maximum (FWHM) of the diffraction peak and 2θ is the Bragg angle.

Notably, the average crystallinity of the biosynthesized pure CuO NPs, N-CuO NPs, Zn-CuO NPs, and N-Zn-codoped CuO NPs was 38.995, 35.179, 35.041, and 31.929 nm, respectively (Table 4). The decrease in crystallite size from pure to codoped CuO NPs is due to the controlled crystallization of the CuO lattice in the presence of urea and zinc, which alters the growth kinetics of the crystals. The results indicated broadened diffraction peaks, suggesting lattice disorder and associated stresses, as well as peak shifts and reduced intensity due to the incorporation of dopant ions into the CuO lattice. XRD diffraction results also confirm the successful incorporation of the dopant into the CuO crystal lattice, as similarly revealed in the UV–Vis, FT-IR, and SEM analyses previously discussed. This is expected to improve the photocatalytic activity by modifying the optical and electrical conductivity properties of CuO semiconductors. Similar studies have explored the effects of dopants and codopants on the monoclinic crystal lattice of Ag-Mo-codoped CuO [32], Mn-Nd-codoped CuO [132], Fe-Co-codoped CuO [133], and Fe-Cd-codoped CuO [117] nanoparticles, and the current study shows good results in terms of both optical alteration and photocatalytic performance, as illustrated in Table 6.

Table 4: XRD data used for calculating the crystalline size of pure CuO NPs, N-CuO NPs, Zn-CuO NPs and N-CuO NPs

Nano catalysts	Peak No	Miller indices (hkl)	2θ (°)	FWHM (°)	Height of intensity (a.u)	D* (nm)	Av. D (nm)
CuO NPs	1	110	33.86855	0.14036	880.981	59.1648	38.995
	2	002	35.50865	0.23855	2282.905	34.9678	
	3	111	38.7191	0.30891	2344.291	27.2584	
	4	112	48.77384	0.25218	1267.552	34.5885	
N-CuO NPs	1	110	33.8005	0.18176	992.632	45.6804	35.179
	2	002	35.4707	0.24187	2325.682	34.4842	
	3	111	38.681	0.31767	2354.571	26.5037	
	4	112	48.7413	0.25614	1228.922	34.0494	
Zn-CuO NPs	1	110	33.85	0.19969	790.448	41.5843	35.040
	2	002	35.5198	0.23262	2472.843	35.8603	
	3	111	38.7387	0.30138	2452.071	27.9412	
	4	112	48.7779	0.25082	1217.066	34.7766	
N-Zn-CuO NPs	1	110	33.8266	0.18561	863.4293	42.801	31.929
	2	002	35.5005	0.25371	2188.200	31.3125	
	3	111	38.7128	0.33019	2241.252	24.0598	
	4	112	48.7659	0.2689	1156.382	29.5437	

*D = Crystallite size (nm)

4.3. Photocatalytic Activity Study

4.3.1. Effect of Dopant Concentration

The dopant concentration directly affects the enhancement of photocatalytic activity through techniques such as crystal lattice modification, the surface area of metal oxide semiconductor, charge carrier dynamics, the recombination rate, chemical stability, and synergistic effects during photodegradation [78]. Considering this, the effect of dopant concentration was optimized by varying the dopant concentration to 1% (0.02 g), 3% (0.06 g), 6% (0.12 g), and 10% (0.2 g) within 2 g of copper oxide precursor, respectively, as shown in Table 3. The optimal dopant concentrations for both N and Zn were determined based on the performance of the nanoparticles in terms of photocatalytic degradation efficiency and are presented in detail in Figure 26 and Appendix 1. As indicated in the figure 26, the efficiency of photocatalytic degradation increased from 94.62% to 98.4% and 97.5% to 98.71% as the dopant concentration increased from 1 to 3%, after which the efficiencies decreased 95.79% to 94.71% and 94.59% to 92.92% as the dopant concentration increased 6 to 10% for the nitrogen and zinc source precursors, respectively. For both the N-CuO and Zn-CuO nanoparticles, the photocatalytic degradation efficiency

increased as the concentration of dopants increased to the optimal point, indicating that the dopants successfully modified the electronic structure, creating new energy levels within the band gap or altering the band edges, which can enhance light absorption and charge carrier separation, leading to improved photocatalytic activity. However, beyond the optimal concentration, the efficiency decreased, which could be due to the oversaturation of dopants leading to agglomeration, inhibitory effects and extra changes in the crystal lattice, phase and surface area of metal oxide semiconductor that affect photocatalytic properties and reduce the number of active sites available for photocatalysis. Among the five N and Zn doping concentrations, 3 wt% showed superior photocatalytic performance. Hence, a 3% dopant concentration was chosen as the optimal concentration for both N and Zn for codoping, instrumental characterization and investigation of other photocatalytic degradation reaction parameters.

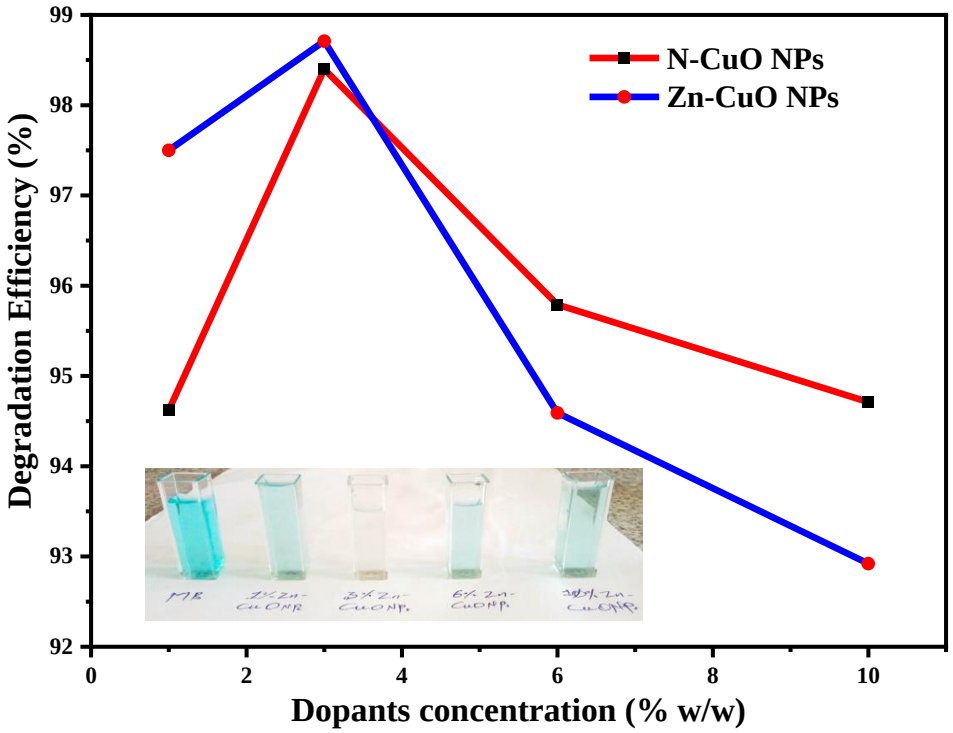

Figure 26: Effect of dopant concentration (photocatalyst dose: 80 gm/50 ml for MB, 5 ppm initial conc. of MB, pH 11, A_0 = 0.637, & exposure time to sunlight = 1hr)

4.3.2. Effect of Solution pH

The pH of the solution significantly affects photocatalytic degradation, as it can not only influence the surface charge and chemical properties of the photocatalyst but also alter the different forms of many inorganic and organic species in the reaction mixture [115]. Hence, the influence of pH on MB photocatalytic degradation by biosynthesized pure CuO

NPs, N-CuO NPs, Zn-CuO NPs and N-CuO NPs was investigated over a pH range of 2–14 at a constant nano photocatalyst dose (80 mg), initial concentration of MB (5 ppm), and irradiation time (1 hr). The optimal photocatalytic degradation efficiencies of 91.19% and 94.27% at pH 12 for the pure CuO NPs and Zn-CuO NPs, 90.17% and 97.06% at pH 11 for the N-CuO NPs and N-Zn-CuO NPs, respectively, were determined, as shown in Figure 27 and Appendix 2. Notably, the photocatalytic degradation efficiency of MB by all the biosynthesized nanocatalysts increased to the optimal pH of the solution and then decreased slightly, indicating the effect of the specific photocatalyst and pollutant being used. This is because the surface of the nano photocatalysts is negatively charged in an alkaline medium (OH^-) and positively charged in an acidic medium (H^+). Because MB is a cationic dye, its structure becomes positively charged when it is dissolved in water.

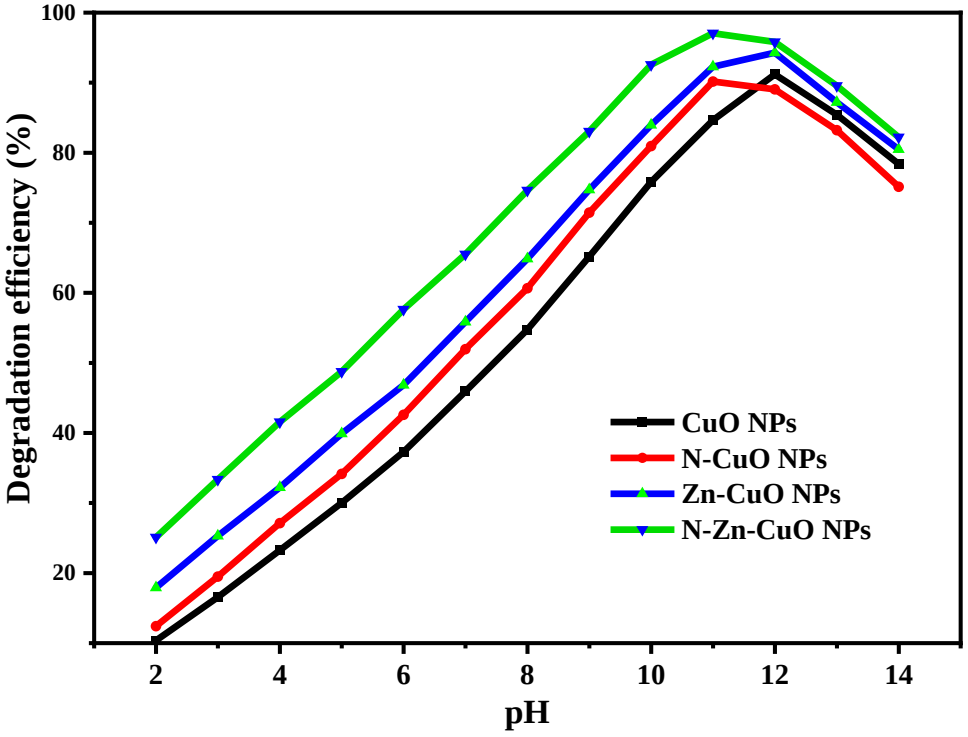

Figure 27: Effect of solution pH on the photocatalytic degradation of MB (5 ppm initial conc. MB, 80 mg of photocatalyst dose, A_0 = 0.637 and exposure time = 1 hr)

Therefore, at lower pH in acidic media, protonation creates a surface on the nanocatalyst with a positive charge, which increases the repulsive forces between the positively charged photocatalyst and the cationic dye (MB). This influences the stability and activity of the nanocatalyst, leads decreasing the photocatalytic degradation efficiency.

On the other hand, the photocatalytic degradation efficiencies of MB are greater in alkaline media due to an increase in opposite-charge interactions between the solution and

the surface of the nano photocatalyst due to nanocatalyst surface deportation [134]. Further increases in pH beyond 11 for the pure N-CuO NPs and N-Zn-CuO NPs and 12 for the pure CuO NPs and Zn-CuO NPs resulted in a slight decrease in the photocatalytic degradation efficiency because the surface of the nanocatalyst became negatively charged due to the presence of more hydroxyl ions (OH^-). This may reduce the columbic attraction between the MB dye molecule and the nanocatalyst surface [112].

4.3.3. Effect of Photocatalyst Dosage

Determining the optimal photocatalytic dosage is a key point in scaling up catalytic performance due to its vital role in photocatalysis [134]. The effect of the catalyst dosage of the biosynthesized pure CuO NPs, N-CuO NPs, Zn-CuO NPs and N-CuO NPs was studied by varying the photocatalyst load from 10 to 200 mg within 40 mg intervals at a constant irradiation time (1 hr), initial MB concentration (5 ppm) and at the optimized pH of the solution as discussed earlier, as shown in Figure 28.

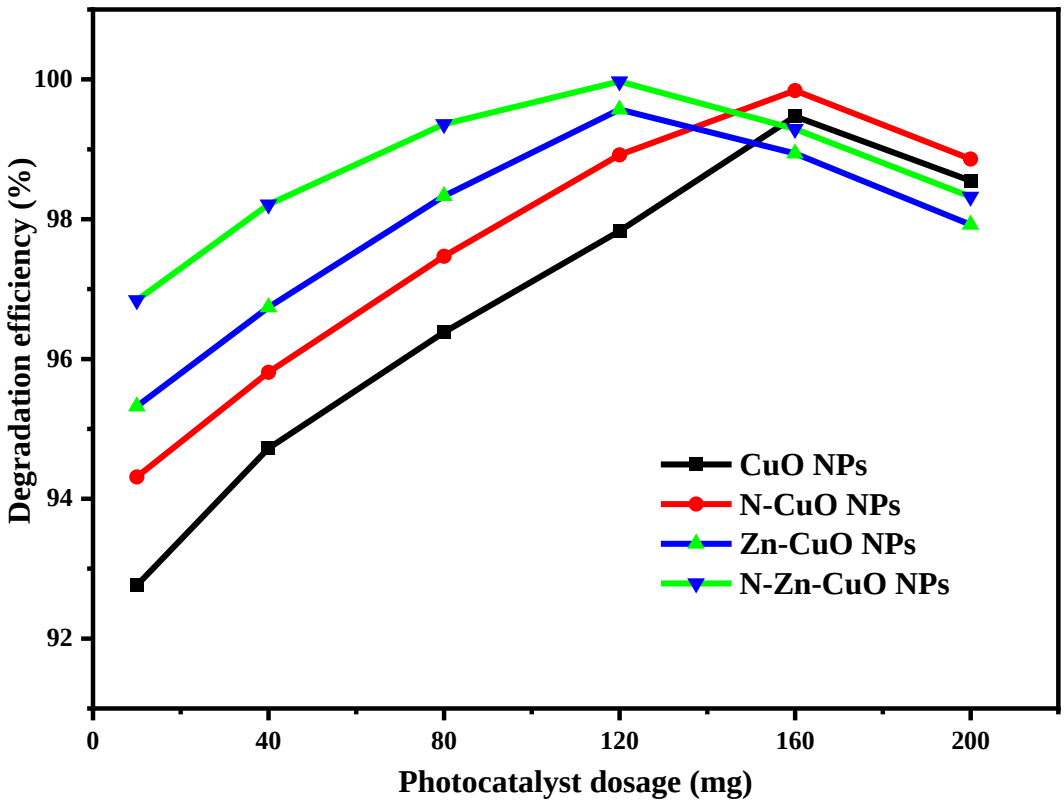

Figure 28*:* Effect of nano photocatalyst dosage on the photocatalytic degradation of MB (5 ppm initial conc. MB, with an optimized pH of 11 for pure N-CuO NPs and N-Zn-CuO NPs and 12 for pure CuO NPs and Zn-CuO NPs; A_0 = 0.637, and exposure time = 1 hr)

The results displayed in Figure 28 and Appendix 3 show that an increase in the nano photocatalyst loading from 10 to 160 mg sharply increased the degradation of MB to a maximum of 99.37% and 99.84% for pure CuO NPs and N-CuO NPs, respectively, and from 10 to 120 mg sharply increased the degradation of MB to a maximum of 99.57% and 99.97% for Zn-CuO NPs and N-Zn-CuO NPs, respectively, due to the increase in the number of hydroxyl and superoxide radicals on the number of active sites attributed to the greater accessibility of e^-/h^+ and photoresponsiveness. However, a further increase in the nano photocatalyst loading beyond the optimal mg (160 mg for pure CuO NPs and N-CuO NPs and 120 mg for Zn-CuO NPs and N-Zn-CuO NPs) resulted in a decrease in the photocatalytic degradation rate. This phenomenon may be due to factors such as nano photocatalyst aggregation, saturation of active sites, hindrance and blocking of light penetration and low availability of degradation dye caused by the excessive amount of photocatalyst [4, 93].

4.3.4. Effect of Initial Concentration of MB

The initial concentration of dye in solution can also affect photocatalytic degradation efficiency [100]. The impact of initial concentrations of MB on the photocatalytic degradation efficiency of the biosynthesized pure CuO NPs, N-CuO NPs, Zn-CuO NPs, and N-Zn-CuO NPs was investigated through seven aqueous solutions with concentrations ranging by 5 ppm from 1 to 30 ppm at constant irradiation times (1 hr), and optimal nano photocatalyst doses and pH values, as determined earlier. As shown in Figure 29 and Appendix 4, an initial concentration of MB increased from 1 ppm to 20 ppm, the photocatalytic of degradation shows plateau graph with maximum efficiencies of 99.24, 99.11, 99.07, 99.03 and 98.79% for pure CuO NPs, 99.37, 99.21, 99.13, 99.05, and 98.86% for N-CuO NPs, 99.41, 99.29, 99.18, 99.11 and 98.92% for Zn-CuO NPs, and 99.92, 99.71, 99.42, 99.29, and 99.14% for N-Zn-CuO NPs with slightly difference. At low MB concentrations (≤20 ppm), all nanoparticles exhibited high degradation efficiency (≥99%). This is because the nanoparticles have a large surface area available for adsorption and interaction with photons, resulting in more active sites and facilitate the generation of reactive species (such as hydroxyl radicals •OH) for photocatalytic reactions. Additionally, at low MB concentrations, there are fewer MB molecules competing for photon absorption and sufficient MB molecules available to be handled by the loaded photocatalyst results a higher proportion of photons are available for exciting the photocatalyst, leading to efficient degradation [3, 135]. The subsequent decrease in

photocatalytic degradation efficiency with increasing initial MB concentration above the optimum value is primarily due to the large amount of adsorbed MB, which could block active sites and reduce the interaction of light with these sites for ROS generation [3, 113]. At a high dye concentration, a significant amount of light can be absorbed by dye molecules rather than by photocatalysts, resulting in decreases in the formation of hydroxyl radicals (•OH) and superoxide ions ($•O^{2-}$). However, the degradation rate decreases with further increases in dye concentration [64].

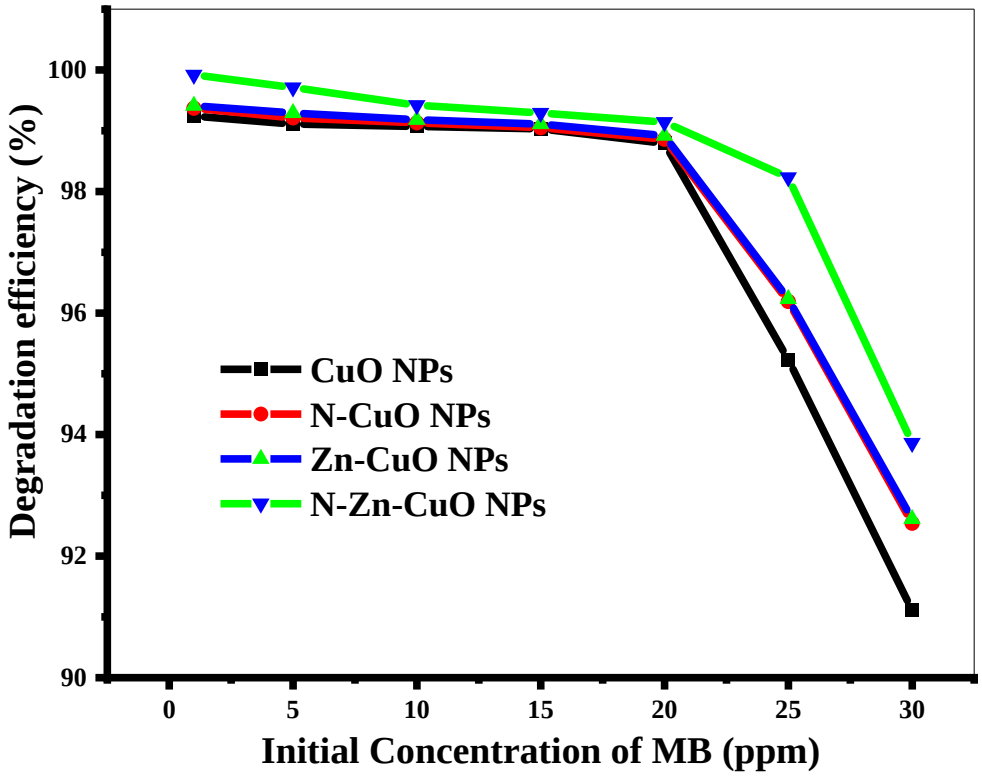

Figure 29: Effect of initial concentration of MB on photocatalytic degradation of MB (photocatalyst dosage of 160 mg for the pure CuO NPs and N-CuO NPs and 120 mg for the Zn-CuO NPs and N-Zn-CuO NPs and pH of 11 for the N-CuO NPs and N-Zn-CuO NPs and at a pH of 12 for the pure CuO NPs & Zn-CuO NPs, respectively, with an exposure time of 1hr)

4.3.5. Effect of Reaction Time at Optimal Condition

The reaction time (exposure time to sunlight and stirring time in the dark) is important for ensuring complete degradation of the pollutant and highly depends on the temperature of sunlight radiation applied to the sample [98]. In this study, the effect of reaction time (irradiation pulse dark reaction) on the photocatalytic degradation of MB by biosynthesized pure CuO NPs, N-CuO NPs, Zn-CuO NPs and N-CuO NPs was

investigated by measuring the degradation efficiency at 10 min intervals while keeping all other parameters at the optimal points for each nanocatalyst, as discussed earlier.

As shown in Figure 30 and Appendix 5, the photocatalytic degradation of MB increased sharply to 95.76%, 97.93%, 98.26% and 99.75% degradation efficiency as the reaction time increased to 30 min for pure CuO NPs, N-CuO NPs, Zn-CuO NPs and N-CuO NPs, respectively and then plateau. This effective irradiation due to the time required for the photocatalysts to interact with the available MB and break it down with a proportional availability of active sites. However, beyond 30 minutes, further exposure to light did not result in any significant increase in degradation efficiency for any of the samples. This is because the active sites on the photocatalyst surface may become saturated or deactivated over time [112].

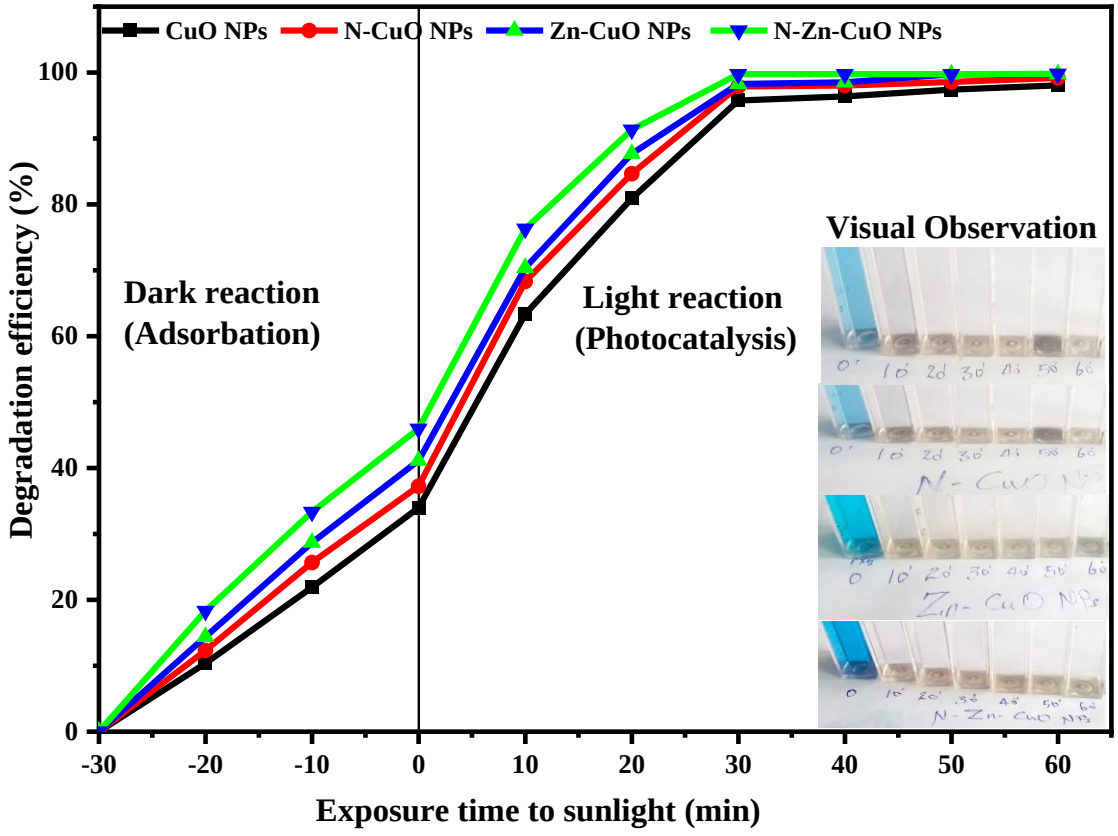

Figure 30: Effect of reaction time on the photocatalytic degradation of MB (photocatalyst dosage of 160 mg for the pure CuO NPs & N-CuO NPs, 120 mg for the Zn-CuO NPs and N-Zn-CuO NPs, pH of 11 for the N-CuO NPs & N-Zn-CuO NPs, pH of 12 for the pure CuO NPs & Zn-CuO NPs, 20 ppm initial conc. MB, A_0 = 2.230 with an exposure time of 1 hr)

Important comparison represented by Figure 30 shows that the adsorption process that occurred in the dark reaction time (30 min) region was a thermodynamic reaction, with degradation efficiencies of 33.94%, 37.76%, 41.12% and 45.95% for pure CuO NPs, N-CuO NPs, Zn-CuO NPs and N-Zn-CuO NPs, respectively, whereas the photocatalysis reaction occurred in the light region, which resulted in approximately two-fold fast degradation efficiencies of 95.76%, 97.93%, 98.26% and 99.75% for pure CuO NPs, N-CuO NPs, Zn-CuO NPs and N-Zn-CuO NPs, respectively, within a similar 30 min reaction. This increase in efficiency can be directly correlated with the generation of electron-hole pairs, which subsequently generate superoxide anions and hydroxyl radicals when light is incident on a semiconductor photocatalyst, and these reactive oxygen species (ROS) cause the degradation of dye molecules [136].

Notably, the photocatalytic dye degradation efficiency of pure CuO was 95.76% after 30 min of light irradiation. When N and Zn are doped alone with CuO, the efficiencies increase to 97.88% and 98.26%, respectively, for the same period of irradiation. This increase in photocatalytic performance due to a decrease in the band gap of the CuO lattice with n-type or p-type dopants causes more electron-hole pairs to be generated, leading to an increase in ROS generation. Interestingly, the excellent photocatalytic activity of the N-Zn-CuO NPs was 99.75% after 30 min of light irradiation, which is attributed to the synergetic effects of N and Z on the surface of CuO; these N-Zn-CuO NPs can photogenerate electron-hole pairs, effectively suppressing the recombination rate, and quickly transfer excited electrons from Cb by reducing the energy band gap in both Cb with an n-type dopant nitrogen and Vb with an p-type dopant zinc [32, 112].

4.4. Kinetic Study for Photocatalytic Degradation

4.4.1. Calibration Curve

A kinetic study of photocatalytic degradation examines how quickly a pollutant breaks down under optimal conditions, determining key factors such as the rate constant, reaction order, and activation energy. Using photocatalysts such as metal oxides and light sources (UV or visible), the study models the reaction kinetics, which can follow pseudo-order, first-order, second-order, or BMG kinetics, based on the specific mechanism [104]. In this study, various kinetic models were employed to analyse the experimental data and determine the degradation mechanism of dyes. To investigate the selected kinetic models, the calibration curve was first plotted with the initial concentration of MB versus its

corresponding absorbance, as depicted in Figure 31. This was done to determine the molar absorptivity coefficient based on the data presented in Appendix 6.

Based on the Beer–Lambert law of concentration and absorbance relationship, the concentrations of MB after photocatalytic degradation at any time interval and other quantities of kinetic models were calculated.

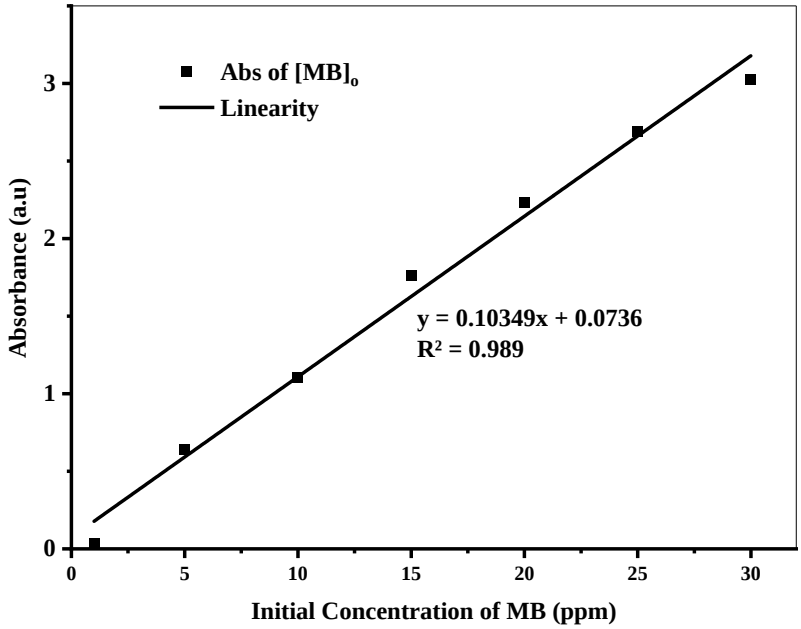

Figure 31: Calibration curve of initial concentration of MB

This was done to investigate the degradation rate of MB by biosynthesized pure CuO NPs, N-CuO NPs, Zn-CuO NPs, and N-Zn-CuO NPs using pseudo-zero-order, pseudo-first-order, pseudo-second-order, and BMG models. The data is presented in Appendix 7.

4.4.2. Pseudo-Zero, First, Second and BMG kinetics models

To investigate the degradation kinetics of MB dyes facilitated by biosynthesized pure CuO NPs, N-CuO NPs, Zn-CuO NPs, and N-Zn-CuO NPs, linearized Equations (2), (5), (8), and (11) were used. The data presented in Appendix 7 were used to plot graphs as C_o-C_t against time (t), ln $[C_o/C_t]$ against time (t), $[1/C_o\text{-}1/C_t]$ versus time (t), and $[t/(1 – C_t/C_o]$ versus time (t) for pseudo-zero-order, pseudo-first-order, and pseudo-second-order and BMG kinetics models, respectively, & the graphs are illustrated in Figure 32 (a, b, c, & d). The correlation coefficients (R^2) and rate constants ($k_{0\text{-}2}$) for each pseudo kinetics model, as well as the correlation coefficients (R^2), inverses of intercepts (m) corresponding to the initial dye decolorization rate (1/m), and inverses of slopes (b) corresponding to the maximum decolorization capacity (1/b) of the BMG kinetic model [137], were

determined, and the results are tabulated in Table 5. The data indicate notably high correlation coefficients (R^2) near unity = 0.99741, 0.99637, 0.99741, and 0.99799 for the biosynthesized pure CuO NPs, N-CuO NPs, Zn-CuO NPs, and N-Zn-CuO NPs, respectively, for the MB degradation rate according to the BMG kinetic model (Figure 32d). These results signify strong fits for the degradation of MB on the surface of all photocatalysts with the BMG kinetic model compared to other pseudo-kinetic models. Furthermore, a comparable study utilizing pure CuO NPs for the degradation of Congo red and Alizarin red S reported higher correlation coefficients of 0.99998 for both dyes in the same model [3]. Conversely, the correlation coefficients for the pseudo-zero, first, second-order models were lower for MB dyes on the surface of all the photocatalysts, as detailed in Table 5, suggesting that the photocatalytic degradation of MB dye does not conform well to these models.

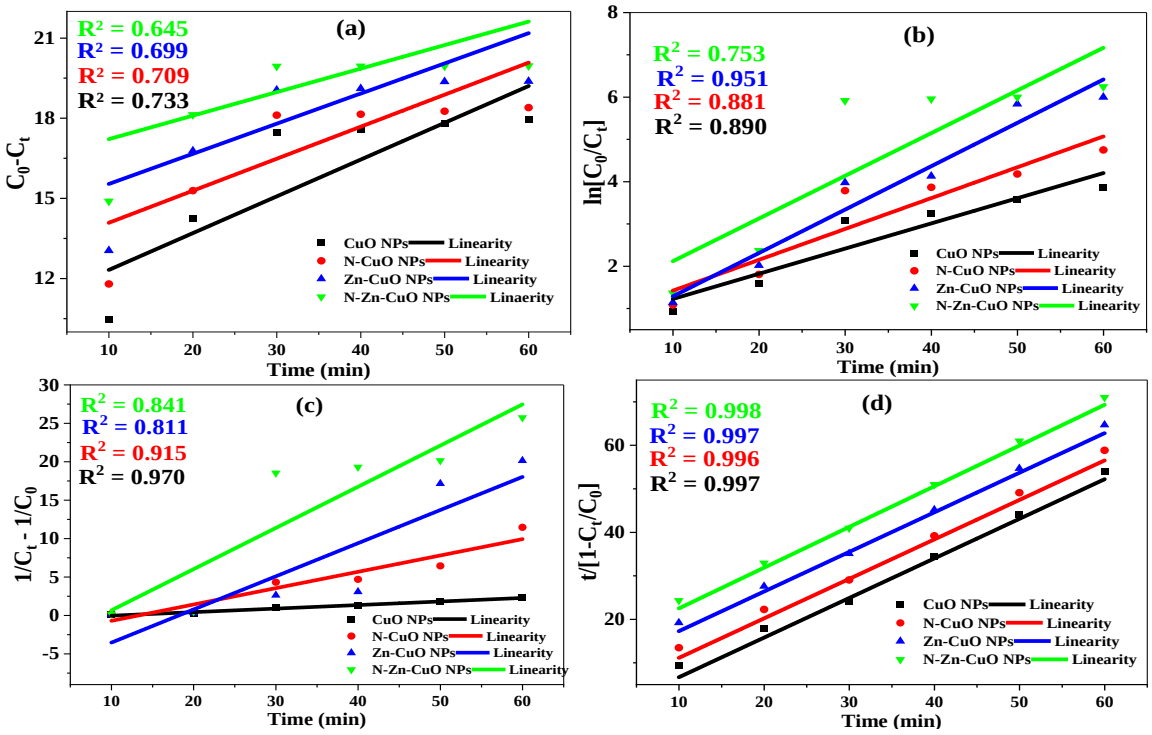

Figure 32: Pseudo zero-order (a), pseudo-first-order (b), pseudo-second-order (c), and BMG kinetic models (d) for the photocatalytic degradation of MB by biosynthesized pure CuO NPs, N-CuO NPs, Zn-CuO NPs, & N-Zn-CuO NPs.

The parameter 1/b, which is associated with the maximum decolorization capacity of the photocatalysis reaction for the BMG model, was 1.098, 1.101, 1.098 and 1.068 for the biosynthesized pure CuO NPs, N-CuO NPs, Zn-CuO NPs, and N-Zn-CuO NPs, respectively. The observed values of 1/b are equal to ≥1, implies that all the

biosynthesized nanocatalysts have high capacity for decolorization of MB dye by photocatalysis reaction [138]. According to the BMG model, the 1/m parameter values were 0.188, 0.191, 0.213, and 0.310 min^{-1} for the biosynthesized pure CuO NPs, N-CuO NPs, Zn-CuO NPs, and N-Zn-CuO NPs, respectively, which indicated the initial discolouration rate of the MB dye. The sharp increase in the discolouration rate (1/m) from pure to doped and codoped samples revealed the successful increase in the photocatalytic degradation rate and efficiency of the CuO lattice upon modification. Interestingly, the highest 1/m value was 0.310 min^{-1} for N-Zn-CuO NPs, which is 1.65 times faster than the initial discolouration rate of MB dye with pure CuO, which is 0.188 min^{-1} due to high photons generate and transfer a large number of hydroxyl species (OH•) and superoxide species ($•O^{2-}$) radicals caused by band reduction with codoping. A similar outcome was observed for the discolouration of an azo dye (methyl orange) by Xu *et al.,* [138].

Table 5: Fitted data of the selected kinetics models for the photocatalytic degradation of MB by all the biosynthesized nanocatalysts

Kinetic Models	**Pseudo-Zero Order**		**Pseudo-Fist Order**		**Pseudo-Second Order**		**BMG**		
Nanocatalyst	k_0 (ppm /min)	R^2	k_1 (min^{-1})	R^2	k_2 (min/ ppm)	R^2	1/m (min^{-1})	**1/b**	R^2
CuO NPs	0.138	0.732	0.059	0.891	0.891	0.970	0.188	1.098	0.9973
N-CuO NPs	0.120	0.709	0.073	0.882	0.213	0.914	0.191	1.101	0.9963
Zn-CuO NPs	0.113	0.699	0.102	0.951	0.431	0.811	0.213	1.098	0.9974
N-Zn-CuO NPs	0.088	0.645	0.101	0.753	0.536	0.841	0.310	1.068	0.9979

The BMG kinetic model (Behnajady, Modirshahla, Ghanbery) offers significant implications for photocatalytic reactions; (1) Reaction Mechanism Understanding: Unveils intricate steps and rate-determining factors in pollutant degradation. (2) Reaction Rate Quantification: Accurately measures reaction rates and constants, optimizing conditions and system design. (3) Degradation Efficiency Prediction: Predicts degradation efficiency under varying conditions, aiding in parameter optimization. (4) Photocatalyst Comparison: Enables comparative analyses to identify the most effective catalysts for specific applications.

In summary, the BMG kinetic model is well-suited for fitting photocatalytic degradation reactions due to its ability to capture complex reaction mechanisms, consider multiple influencing parameters, and provide predictive insights into the behaviour of photocatalytic systems.

4.5. Mechanism of Photocatalytic Degradation

A reasonable mechanism explaining the photocatalytic degradation of MB on the surfaces of pure CuO NPs, N-CuO NPs, Zn-CuO NPs, and N-Zn-CuO NPs under sunlight irradiation was proposed based on the experimental findings, as depicted in Figure 33. Photocatalytic degradation of MB through the photocatalysis reaction commences when sunlight irradiates the surface of pure CuO NPs, leading to the absorption of photons (hv) by the photocatalyst (Eq. 20). This absorption results in the generation of electrons (e^-) and holes (h^+) in the valence band (Vb), as illustrated in Figure 33a. Immediately, photogenerated electrons (e^-) with energies equal to or greater than the 1.72 eV band gap are excited to the conduction band (Cb) of CuO NPs, where they interact with atmospheric oxygen molecules to produce superoxide anion radicals ($\bullet O^{2-}$) (Eq. 21). Similarly, photogenerated holes (h^+) at the Vb react with water molecules to generate hydroxyl radicals (OH•) (Eq. 22) The reactive oxygen species (ROS), namely, OH• and $\bullet O^{2-}$, produced through these processes target the chromophore groups (-N=C- and -S=C-) of the MB dye, leading to the rapid breakdown of its molecular structure into colorless and nontoxic mineralized molecules (Eq. 23), specifically leucomethylene blue (LMB), which further decomposes into CO_2 and H_2O [9, 139], as represented in equations (20-23) below:

$$\mathrm{CuO} + h\nu \rightarrow h^+_{(Vb)} + e^-_{(Cb)} \quad \text{photoinitiation} \quad (20)$$

$$e^-_{(CB)} + O_2 \rightarrow \bullet O^2 \quad \text{photooxidation} \quad (21)$$

$$h^+_{(Vb)} + H_2O \rightarrow \bullet OH + H^+ \quad \text{photoreduction} \quad (22)$$

$$\bullet OH / \bullet O^{2-} + \text{MB dye} \rightarrow \text{LMB} \rightarrow CO_2 + H_2O \quad \text{photodegradation product} \quad (23)$$

The present study investigated the effects of doping and codoping copper oxide nanoparticles with nitrogen and/or zinc, which resulted in changes in the electron-hole transfer mechanism, and this modification led to an increase in the photocatalytic degradation rate and efficiency of the MB dye.

In pure CuO NPs, the large band gap energy resulted in a higher rate of electron-hole recombination, leading to less efficient photocatalytic activity. However, when n-type dopant nitrogen was incorporated into the oxygen vacancy defects of CuO lattice (N-CuO NPs), it was generated a new electron donor electronic state below the Cb and reducing the band gap to 1.44 eV. This newly formed electronic state energy level could increase the electron carrier concentration and assisting in electron transfer to the Cb due to donor

nitrogen impurity [126]. On the other hand, the introduction of p-type dopant zinc into the Cu^{2+} of CuO lattice (Zn-CuO NPs), it was created a new electron acceptor electronic state above the Vb, and decreased the band gap to 1.29 eV. This process borrows/accept an electron from a neighbouring host semiconductor and creating more holes within the crystal structure that acts as a positive charge carrier moving freely due to acceptor zinc impurity. Which results enhanced photocatalytic activity by increasing the rate of hole concentration and electron excitation to the Cb, facilitate better electron-hole separation, and decreased electron-hole recombination [140]. This reduction in band gap leads to the production of a large number of ROS, which can enhance the photocatalytic degradation rate, and the efficiency is visually represented in Figure 33b-c.

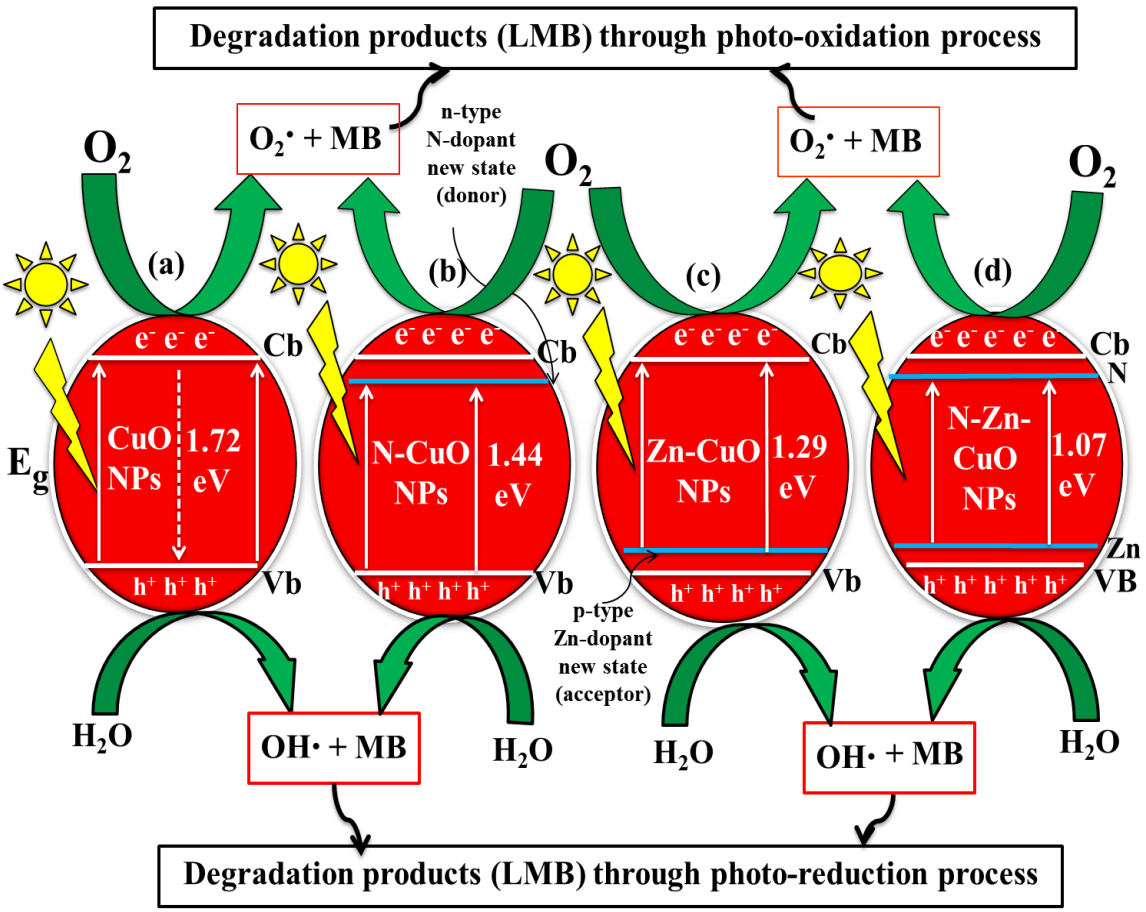

Figure 33: Schematic illustration of the photocatalytic degradation mechanism of MB by biosynthesized pure CuO NPs (a), N-CuO NPs (b), Zn-CuO NPs (c), and N-Zn-CuO NPs (d)

The most significant improvement was observed for the N-Zn-CuO NPs, where codoping with both nitrogen and zinc resulted in the lowest band gap energy of 1.07 eV. This synergistic codoping optimized the electron-hole separation and transfer mechanisms,

leading to a substantial increase in ROS (OH• and $•O^{2-}$) production [32, 112] and consequently boosting the photocatalytic degradation efficiency of MB compared to that of pure and doped CuO NPs, as shown in Figure 33d. As indicated above, there is a direct correlation between the photocatalytic degradation efficiency of the dye and variations in the band gap.

4.6. Nanocatalyst Reusability Test

The issue of nanocatalyst reusability poses a significant challenge in current research, as many catalysts lose their effectiveness after a few cycles, leading to their disposal. The reusability and stability of nanocatalysts play a critical role in determining their overall performance, as a durable and active catalyst can significantly reduce process costs. Hence, the reusability and nanocatalytic stability of all the synthesized nanoparticles for the degradation of MB were evaluated under optimal experimental conditions by testing all the biosynthesized nanocatalysts over four cycles under solar irradiation. As shown in bar Figure 34 and Appendix 8, the photocatalytic degradation efficiencies of pure CuO NPs, N-CuO NPs, Zn-CuO NPs, and N-Zn-CuO NPs were 95.76%, 97.88%, 98.26% and 99.75%, respectively, after four consecutive reuse cycles, and the degradation efficiencies were 90.09%, 93.43%, 94.83%, and 95.82%, respectively, under sunlight irradiation. The results highlighted that all the biosynthesized nanocatalysts exhibit excellent reusability and stability performance, with minimal decrease in the photocatalytic degradation efficiency per four reuse cycles. Notably, doping and codoping not only improve the photocatalytic activity of CuO NPs but also enhance their stability and reusability. This is confirmed by the reusability test, which showed that the degradation efficiency decreased by less than 1% per cycle, outperforming the undoped CuO nanocatalyst. In general, this small decrease indicates good reusability and stability of the catalysts. These findings underscore the potential for green-synthesized pure CuO NPs, N-CuO NPs, Zn-CuO NPs, and N-Zn-CuO NPs to serve as efficient and sustainable nanocatalysts across various applications, suggesting promising prospects for their practical catalytic decomposition of organic contaminants in environmental remediation.

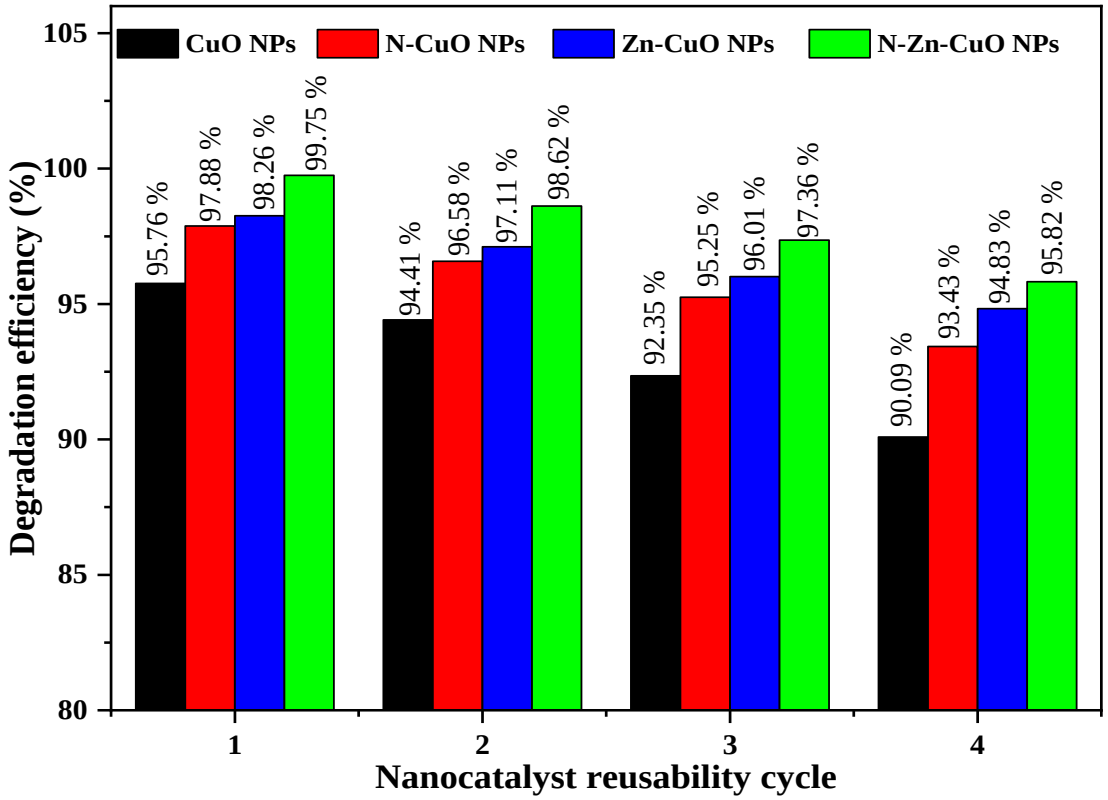

Figure 34: Reusability of pure CuO NPs, N-CuO NPs, Zn-CuO NPs, and N-Zn-CuO NP nanocatalysts for the degradation of MB

4.7. Comparison of Pervious Works

A comprehensive review was conducted to compare the photocatalytic degradation efficiency of methylene blue under natural sunlight using previous works, chemical and green synthesized pure and modified CuO nanoparticles. The findings were summarized in Table 6. In this current study, biosynthesized pure CuO NPs, N-CuO NPs, Zn-CuO NPs, and N-Zn-CuO NPs demonstrated superior results compared to previous reports in terms of optical alteration-led photocatalytic performance. These nanoparticles achieved an impressive efficiency of 99.75% in a 30-minute photocatalysis reaction. This remarkable outcome addresses the existing research gap successfully by employing a synergistic codoping approach through a green synthesis method.

Table 6: Summarization and Comparison of previous works

Nano Photocatalyst	Synthesis methods	Crystalline Size (nm)	Band gap (eV)	Exposure time (min)	Degradation efficiency (%)	Ref
CuO NPs	Biological *(Ocimum americanum)*	68	-	200	71.06	[141]
CuO NPs	Biological *(Amaranthus dubius)*	11	2.23	150	84	[142]
CuO NPs	Biological *(Neem leaf)*	18.42	1.67	30	79.28	[112]
CuO NPs	Chemical *(co-precipitation)*	9.01	1.93	100	38.77	[13]
Ce-Zn- CuO NPs		8.36	1.01		81.64	
CuO NPs	Biological *(Acmella ciliate)*	18.53	1.88	120	68	[96]
Ni-CuO NPs		8.63	1.73		81	
CuO NPs	Chemical (combustion)	52	1.52	120	92	[143]
Tb-CuO NPs		27	1.46		94	
CuO NPs	Chemical *(co-precipitation method*	21	3.230	12	77.81	[129]
Co-CuO NPs		31	3.256		68.90	
Mn-CuO NPs		27	3.207		70.83	
Ni-CuO NPs		29	3.274		81.53	
CuO NPs	Chemical (microwave)	13.10	1.42	60	97	[34]
Ag-Fe-CuO NPs		21.53	1.41		94	
CuO NPs	Biological *(Azadirachta Indica)*	19.8	2.93	180	52%	[32]
Ag-CuO NPs		17.20	2.39		74%	
Mo-CuO NPs		14.57	2.59		88%	
Ag-Mo-CuO NPs		11.23	2.22		99%	
CuO NPs	Biological *(Pycnostachys Abyssinica)*	38.995	1.72	30	95.76	This work
N-CuO NPs		35.179	1.44		97.88	
Zn-CuO NPs		35.041	1.29		98.26	
N-Zn-CuO NPs		31.929	1.07		99.75	

CHAPTER FIVE

CONCLUSION AND RECOMMENDATION

5.1. Conclusion

In this study, N-Zn-codoped CuO NPs was successfully synthesized as highly efficient photocatalyst by using *Pycnostachys abyssinica* Fresen plant leaf extract as a bioreducing and capping agent for the photocatalytic degradation of methylene blue under natural sunlight irradiation. Additional, pure CuO NPs, N-CuO NPs, and Zn-CuO NPs were also synthesized through a green method to compare their photocatalytic activity with that of N-Zn-codoped CuO NPs. The biosynthesized nanoparticles were characterized using UV–Vis, XRD, SEM, and FT-IR techniques. The average crystallinity (D) was determined to be 25 nm, 19.8 nm, 17.20 nm, 14.57 nm, and 11.23 nm, while the energy band gap (Eg) values were 1.72 eV, 1.44 eV, 1.29 eV, and 1.07 eV for the biosynthesized pure CuO NPs, N-CuO NPs, Zn-CuO NPs, and N-Zn-CuO NPs, respectively. The significant changes in the D and Eg values indicate the formation of new electronic states between the valence and conduction bands, resulting in bandgap engineering with successful dopant incorporation into CuO NPs. The photocatalytic activity of all the biosynthesized nanoparticles was assessed using methylene blue (MB) dye under solar light irradiation. The results showed that the photocatalytic activity of N-Zn-CuO NPs (99.75%) surpassed that of Zn-CuO NPs (98.26%), N-CuO NPs (97.93%), and pure CuO NPs (95.76%) under optimal conditions. The modified optical properties, particularly in the case of N-Zn codoping, likely contributed to the increased extinction of electron-hole pairs, enhancing the photocatalytic activity compared to that of other nanoparticles. Kinetic studies of MB degradation rates revealed high correlation coefficients (R^2) close to unity = 0.99741, 0.99637, 0.99741, and 0.99799 for biosynthesized pure CuO NPs, N-CuO NPs, Zn-CuO NPs, and N-Zn-CuO NPs, respectively, using the BMG kinetic model, indicating its suitability for dye degradation on all photocatalysts. The reusability and stability of the biosynthesized nanocatalysts were evaluated, showing efficient catalytic performance with a slight decrease in degradation rate after multiple uses. The superior photocatalytic activity of the biosynthesized N-Zn-CuO photocatalyst highlights its potential as an effective and environmentally friendly solution for treating toxic organic dyes in environmental remediation efforts.

5.2. Recommendations

Currently study explored the potential of biosynthesized N-Zn-CuO NPs as an efficient and eco-friendly solution for the photocatalytic degradation of toxic MB dyes released from industry. The findings suggest that physiochemical properties of modified N-Zn-CuO nanomaterials have great potential for addressing multiple applications. To fully explore the potential of these nanomaterials, the following future research directions are recommended:

1. **Electrochemical Energy Storage**: Investigate the application of N-Zn-CuO NPs as electrode materials for supercapacitors and batteries. Their high surface area, good conductivity, and electrochemical stability make them promising candidates for high-performance energy storage devices.
2. **Electrochemical Sensing and Catalysis**: Explore the potential of N-Zn-CuO NPs as surface-modified electrodes for biosensors and electro-catalysts. Their unique optical, electrical, and electronic properties could enable the development of sensitive and efficient sensors and catalysts for various applications.
3. **Biological Applications**: Investigate the antibacterial, antimalarial, antimicrobial, and antioxidant properties of N-Zn-CuO NPs. Their biocompatibility and potential pharmacological properties make them promising candidates for nanomedicine applications, leveraging the pharmacological properties of *Pycnostachys abyssinica* Fresen in the nanoparticle matrix.
4. **Long-Term Stability and Reusability**: Conduct thorough evaluations of the long-term stability and reusability of N-Zn-CuO NPs under various environmental conditions. This will ensure their practical applicability for large-scale environmental remediation and other applications.

REFERANCES

[1] M. R. Islam, M. Saiduzzaman, S. S. Nishat, A. Kabir, and S. F. U. Farhad, "Synthesis, characterization and visible light-responsive photocatalysis properties of Ce doped CuO nanoparticles: A combined experimental and DFT+U study," *Colloids Surfaces A Physicochem. Eng. Asp.*, vol. 617, May 2021, doi: 10.1016/j.colsurfa.2021.126386.

[2] A. G. Bekru, L. T. Tufa, O. A. Zelekew, J. Gwak, J. Lee, and F. K. Sabir, "Microwave-Assisted Synthesis of rGO-ZnO/CuO Nanocomposites for Photocatalytic Degradation of Organic Pollutants," *Crystals*, vol. 13, no. 1, Jan. 2023, doi: 10.3390/cryst13010133.

[3] G. F. Aaga and S. T. Anshebo, "Green synthesis of highly efficient and stable copper oxide nanoparticles using an aqueous seed extract of Moringa stenopetala for sunlight-assisted catalytic degradation of Congo red and alizarin red s," *Heliyon*, vol. 9, no. 5, May 2023, doi: 10.1016/j.heliyon.2023.e16067.

[4] Y. S. Jara, T. T. Mekiso, and A. P. Washe, "Highly efficient catalytic degradation of organic dyes using iron nanoparticles synthesized with Vernonia Amygdalina leaf extract," *Sci. Rep.*, vol. 14, no. 1, pp. 1–18, 2024, doi: 10.1038/s41598-024-57554-5.

[5] A. Bafana, S. S. Devi, and T. Chakrabarti, "Azo dyes: Past, present and the future," *Environmental Reviews*, vol. 19, no. 1. National Research Council of Canada, pp. 350–370, 2011. doi: 10.1139/a11-018.

[6] H. Xu *et al.*, "Zn-doped CuO nanocomposites inhibit tumor growth by NF-κB pathway cross-linked autophagy and apoptosis," *Nanomedicine*, vol. 14, no. 2, pp. 131–149, Jan. 2019, doi: 10.2217/nnm-2018-0366.

[7] M. A. Abomuti, E. Y. Danish, A. Firoz, N. Hasan, and M. A. Malik, "Green synthesis of zinc oxide nanoparticles using salvia officinalis leaf extract and their photocatalytic and antifungal activities," *Biology (Basel).*, vol. 10, no. 11, 2021, doi: 10.3390/biology10111075.

[8] A. K. Kushwaha, N. Gupta, and M. C. Chattopadhyaya, "Removal of cationic methylene blue and malachite green dyes from aqueous solution by waste materials of Daucus carota," *J. Saudi Chem. Soc.*, vol. 18, no. 3, pp. 200–207, 2014.

[9] S. Aroob *et al.*, “Green Synthesis and Photocatalytic Dye Degradation Activity of CuO Nanoparticles,” *Catalysts*, vol. 13, no. 3, pp. 1–18, 2023, doi: 10.3390/catal13030502.

[10] S. Gautam *et al.*, “Metal oxides and metal organic frameworks for the photocatalytic degradation: A review,” *J. Environ. Chem. Eng.*, vol. 8, no. 3, p. 103726, 2020.

[11] U. Wijesinghe, G. Thiripuranathar, H. Iqbal, and F. Menaa, “Biomimetic synthesis, characterization, and evaluation of fluorescence resonance energy transfer, photoluminescence, and photocatalytic activity of zinc oxide nanoparticles,” *Sustain.*, vol. 13, no. 4, pp. 1–22, 2021, doi: 10.3390/su13042004.

[12] A. Ahmed *et al.*, “Efficient photocatalytic degradation of toxic Alizarin yellow R dye from industrial wastewater using biosynthesized Fe nanoparticle and study of factors affecting the degradation rate,” *J. Photochem. Photobiol. B Biol.*, vol. 202, p. 111682, 2020, doi: 10.1016/j.jphotobiol.2019.111682.

[13] A. ur Rehman *et al.*, “Fabrication of binary metal doped CuO nanocatalyst and their application for the industrial effluents treatment,” *Ceramics International*, vol. 47, no. 5. Elsevier Ltd, pp. 5929–5937, Mar. 01, 2021. doi: 10.1016/j.ceramint.2020.11.064.

[14] R. Ameta, M. S. Solanki, S. Benjamin, and S. C. Ameta, *Photocatalysis*. 2018. doi: 10.1016/B978-0-12-810499-6.00006-1.

[15] A. Bhaduri and K. Kajal, “Facile synthesis and characterization of cupric oxide (CuO) nanoparticles: Inexpensive and abundant candidate for light harvesting,” in *AIP Conference Proceedings*, 2019, vol. 2093, no. 1.

[16] M. Seethalakshmi, M. Shanthi, S. Dhanapandian, and K. Ashokkumar, “Hydrothermally synthesized various morphological CuO nanoparticles for stable and enhanced supercapacitor applications.” [Online]. Available: https://ssrn.com/abstract=4601113

[17] R. A. Bajwa, U. Farooq, S. Ullah, M. Salman, S. Haider, and R. Hussain, “Metal-organic framework (MOF) attached and their derived metal oxides (Co, Cu, Zn and Fe) as anode for lithium ion battery: A review,” *J. Energy Storage*, vol. 72, p. 108708, 2023.

[18] S. Surendhiran, V. Gowthambabu, A. Balamurugan, M. Sudha, V. B. S. Kumar, and K. C. Suresh, “Rapid green synthesis of CuO nanoparticles and evaluation of its photocatalytic and electrochemical corrosion inhibition performance,” *Mater. Today Proc.*, vol. 47, pp. 1011–1016, 2021.

[19] A. Q. Malik *et al.*, “A review on the green synthesis of nanoparticles, their biological applications, and photocatalytic efficiency against environmental toxins,” *Environ. Sci. Pollut. Res.*, vol. 30, no. 27, pp. 69796–69823, 2023.

[20] A. K. Inamdar *et al.*, “A review on environmental applications of metal oxide nanoparticles through waste water treatment,” *Mater. Today Proc.*, 2023.

[21] G. Chandrabose, “Heterostructured Metaloxide Photocatalytic (Copper Oxide and Titanium Oxide) for Degradation and Removal of Organic Pollutants from Water.” The Open University, 2022.

[22] A. L. Ivansyah *et al.*, “Insight into novel triple doping (Mg, Cu, N and Mg, Cu, B) on the structural, optical, photocatalytic, and antibacterial properties of ZnO,” *Colloids Surfaces A Physicochem. Eng. Asp.*, vol. 678, p. 132454, 2023.

[23] M. Memar, A. R. Rezvani, and S. Saheli, “Synthesis of Cr/Mn and S-doped with CuO nanoparticles and systematic investigations of structural, optical and photocatalytic properties,” *Inorg. Chem. Commun.*, vol. 138, p. 109245, 2022.

[24] E. M. Bayan, T. G. Lupeiko, L. E. Pustovaya, M. G. Volkova, V. V. Butova, and A. A. Guda, “Zn–F co-doped TiO2 nanomaterials: Synthesis, structure and photocatalytic activity,” *J. Alloys Compd.*, vol. 822, May 2020, doi: 10.1016/j.jallcom.2020.153662.

[25] J. Zhang, K. Tse, M. Wong, Y. Zhang, and J. Zhu, “A brief review of co-doping,” *Frontiers of Physics*, vol. 11, no. 6. Higher Education Press, Dec. 01, 2016. doi: 10.1007/s11467-016-0577-2.

[26] X. Niu, W. Yan, C. Shao, H. Zhao, and J. Yang, “Hydrothermal synthesis of Mo-C co-doped TiO2 and coupled with fluorine-doped tin oxide (FTO) for high-efficiency photodegradation of methylene blue and tetracycline: Effect of donor-acceptor passivated co-doping,” *Appl. Surf. Sci.*, vol. 466, pp. 882–892, 2019.

[27] S. G. Rejith and C. Krishnan, “Optical Characterizations of Zn-doped CuO Nanoparticles,” *Sci. Acta Xaver. An Int. Sci. J.*, vol. 4, no. 1, pp. 91–98, 2013,

[Online]. Available: http://oaji.net/articles/2014/1420-1415936604.pdf

[28] G. preet Singh, K. J. Singh, K. Chandel, P. Kaur, and J. Kaur, “Green synthesis of NiO doped CuO Nanoparticles: Potential for Environmental Remediation,” *Inorg. Chem. Commun.*, vol. 157, p. 111250, 2023.

[29] P. S. Vindhya and V. T. Kavitha, “Effect of cobalt doping on antimicrobial, antioxidant and photocatalytic activities of CuO nanoparticles,” *Mater. Sci. Eng. B*, vol. 289, p. 116258, 2023.

[30] D. P. Jaihindh, P. Anand, R.-S. Chen, W.-Y. Yu, M.-S. Wong, and Y.-P. Fu, “Cl-doped CuO for electrochemical hydrogen evolution reaction and tetracycline photocatalytic degradation,” *J. Environ. Chem. Eng.*, vol. 11, no. 3, p. 109852, 2023.

[31] K. Luo *et al.*, “Facile synthesis of Ag/Zn1-xCuxO nanoparticle compound photocatalyst for high-efficiency photocatalytic degradation: Insights into the synergies and antagonisms between Cu and Ag,” *Ceram. Int.*, vol. 47, no. 1, pp. 48–56, Jan. 2021, doi: 10.1016/j.ceramint.2020.06.102.

[32] K. Rajendaran, R. Muthuramalingam, and S. Ayyadurai, “Green synthesis of Ag-Mo/CuO nanoparticles using Azadirachta indica leaf extracts to study its solar photocatalytic and antimicrobial activities,” *Mater. Sci. Semicond. Process.*, vol. 91, pp. 230–238, Mar. 2019, doi: 10.1016/j.mssp.2018.11.021.

[33] Anu, N. Thakur, K. Kumar, and K. K. Sharma, “Application of Co-doped copper oxide nanoparticles against different multidrug resistance bacteria,” *Inorg. Nano-Metal Chem.*, vol. 50, no. 10, pp. 933–943, 2020, doi: 10.1080/24701556.2020.1728554.

[34] N. Thakur *et al.*, “Antibacterial and photocatalytic activity of undoped and (Ag, Fe) co-doped CuO nanoparticles via microwave-assisted method,” *Nanofabrication*, vol. 7, Jun. 2022, doi: 10.37819/nanofab.007.186.

[35] K. Rudresha *et al.*, “Structural, electrochemical sensor and photocatalytic activity of combustion synthesized of novel ZnO doped CuO NPs,” *Mater. Res. Express*, vol. 10, no. 7, Jul. 2023, doi: 10.1088/2053-1591/ace879.

[36] L. Predoană *et al.*, “Copper-/Zinc-Doped TiO2 Nanopowders Synthesized by Microwave-Assisted Sol–Gel Method,” *Gels*, vol. 9, no. 4, p. 267, 2023.

[37] P. G. Ramos, J. Espinoza, L. A. Sánchez, and J. Rodriguez, “Enhanced photocatalytic degradation of Rhodamine B employing transition metal (Fe, Cu, Co) doped ZnO/rGO nanostructures synthesized by electrospinning-hydrothermal technique,” *J. Alloys Compd.*, vol. 966, p. 171559, 2023.

[38] H. J. Biswal, P. R. Vundavilli, K. Mondal, N. P. Shetti, and A. Gupta, “ZnO/CuO nanostructures anchored over Ni/Cu tubular films via pulse electrodeposition for photocatalytic and antibacterial applications,” *Mater. Sci. Energy Technol.*, vol. 6, pp. 237–251, 2023.

[39] S. C. Lims, S. Divya, and M. Jose, “Design of CuO@ SiO2 core shell nanocomposites and its applications to photocatalytic degradation of Rhodamine B dye,” *Opt. Mater. (Amst).*, vol. 144, p. 114356, 2023.

[40] S. M. F. Khyrun, A. J. Christy, R. Usha, L. C. Nehru, and S. Suresh, “Novel solution combustion synthesis of CeO2/CuO nanocomposite for photocatalytic and biological applications,” *Opt. Mater. (Amst).*, vol. 139, p. 113756, 2023.

[41] A. BaQais, M. W. Alam, M. Farhan, G. Muteeb, N. Allag, and S. Mushtaq, “Probe-Sonicated Synthesis of CuO–ZnO Hybrid Nanocomposite for Photocatalytic and Supercapacitor Applications,” *Inorganics*, vol. 11, no. 9, p. 370, 2023.

[42] H. M. Al-Attar, H. T. Hussein, R. S. Zamel, A. J. Addie, and M. K. A. Mohammed, “Methylene blue degradation using ZnO: CuO: Al2O3 nanocomposite synthesized by liquid laser ablation,” *Opt. Quantum Electron.*, vol. 55, no. 4, p. 309, 2023.

[43] Samriti, R. Gupta, O. Ruzimuradov, and J. Prakash, “Synthesis of Multifunctional Hybrid Semiconductor Nanomaterials,” in *Multifunctional Hybrid Semiconductor Photocatalyst Nanomaterials: Application on Health, Energy and Environment*, Springer, 2023, pp. 31–51.

[44] T. Tesfaye Tole and L. Abayneh, “CHEMICAL STUDIES OF COMMIPHORATEREBINTHINA AND PYCNOSTACHYS ABYSSINICA OCCURRING IN ETHIOPIA,” *African J. Chem. Educ.*, vol. 10, no. 1, p. 10, 2020.

[45] S. Dubale, D. Kebebe, A. Zeynudin, N. Abdissa, and S. Suleman, “Phytochemical Screening and Antimicrobial Activity Evaluation of Selected Medicinal Plants in Ethiopia,” *J. Exp. Pharmacol.*, vol. 15, pp. 51–62, 2023, doi: 10.2147/JEP.S379805.

[46] G. Yemata and M. Fetene, “In vitro evaluation of the antibacterial activity of some medicinal plant extracts against Xanthomonas campestris pv. musacearum,” *Ethiop. J. Sci. Technol.*, vol. 10, no. 1, pp. 17–32, 2017.

[47] Y. Dessie and S. Tadesse, “A Review on Advancements of Nanocomposites as Efficient Anode Modifier Catalyst for Microbial Fuel Cell Performance Improvement,” *J. Chem. Rev.*, vol. 3, no. 4, pp. 320–344, 2021, doi: 10.22034/jcr.2021.314327.1128.

[48] S. Vijayaram *et al.*, “Applications of Green Synthesized Metal Nanoparticles — a Review,” *Biological Trace Element Research*. Springer, 2023. doi: 10.1007/s12011-023-03645-9.

[49] E. Bilgiç and A. Baba, “Effect of Urbanization on Water Resources: Challenges and Prospects BT - Groundwater in Arid and Semi-Arid Areas: Monitoring, Assessment, Modelling, and Management,” S. Ali and A. M. Armanuos, Eds. Cham: Springer Nature Switzerland, 2023, pp. 81–108. doi: 10.1007/978-3-031-43348-1_4.

[50] U. T. Bekabil, “Industrialization and Environmental Pollution in Africa: An Empirical Review,” *J. Resour. Dev. Manag.*, vol. 69, no. 21, pp. 18–21, 2020, doi: 10.7176/jrdm/69-03.

[51] S. Mallakpour and M. Madani, “A review of current coupling agents for modification of metal oxide nanoparticles,” *Prog. Org. Coatings*, vol. 86, pp. 194–207, 2015.

[52] M.-C. Daniel and D. Astruc, “Gold nanoparticles: assembly, supramolecular chemistry, quantum-size-related properties, and applications toward biology, catalysis, and nanotechnology,” *Chem. Rev.*, vol. 104, no. 1, pp. 293–346, 2004.

[53] S. Horikoshi and N. Serpone, “Microwave flow chemistry as a methodology in organic syntheses, enzymatic reactions, and nanoparticle syntheses,” *Chem. Rec.*, vol. 19, no. 1, pp. 118–139, 2019.

[54] R. Feynman, “There’s plenty of room at the bottom.,” *Reson. J. Sci. Educ.*, vol. 16, no. 9, 2011.

[55] D. M. Eigler and E. K. Schweizer, “Positioning single atoms with a scanning tunnelling microscope,” *Nature*, vol. 344, no. 6266, pp. 524–526, 1990.

[56] N. Taniguchi, “On the basic concept of‘nano-technology’,” in *Proc. Intl. Conf. Prod. Eng. Tokyo, Part II, 1974*, 1974.

[57] G. M. Nair, T. Sajini, and B. Mathew, “Advanced green approaches for metal and metal oxide nanoparticles synthesis and their environmental applications,” *Talanta Open*, vol. 5, p. 100080, 2022.

[58] S. R. Falsafi *et al.*, “Metal nanoparticles and carbohydrate polymers team up to improve biomedical outcomes,” *Biomed. Pharmacother.*, vol. 168, p. 115695, 2023.

[59] S. S. Shankar, A. Rai, B. Ankamwar, A. Singh, A. Ahmad, and M. Sastry, “Biological synthesis of triangular gold nanoprisms,” *Nat. Mater.*, vol. 3, no. 7, pp. 482–488, 2004.

[60] J. Virkutyte and R. S. Varma, “Green synthesis of metal nanoparticles: biodegradable polymers and enzymes in stabilization and surface functionalization,” *Chem. Sci.*, vol. 2, no. 5, pp. 837–846, 2011.

[61] R. G. Saratale *et al.*, “A comprehensive review on green nanomaterials using biological systems: Recent perception and their future applications,” *Colloids Surfaces B Biointerfaces*, vol. 170, pp. 20–35, 2018.

[62] A. Gour and N. K. Jain, “Advances in green synthesis of nanoparticles,” *Artif. cells, nanomedicine, Biotechnol.*, vol. 47, no. 1, pp. 844–851, 2019.

[63] R. V. Bordiwala, “Green synthesis and Applications of Metal Nanoparticles.- A Review Article,” *Results Chem.*, vol. 5, no. December 2022, p. 100832, 2023, doi: 10.1016/j.rechem.2023.100832.

[64] H. Kausar *et al.*, “Green synthesis and characterization of copper nanoparticles for investigating their effect on germination and growth of wheat,” *PLoS One*, vol. 17, no. 6, p. e0269987, 2022.

[65] S. Jadoun, R. Arif, N. K. Jangid, and R. K. Meena, “Green synthesis of nanoparticles using plant extracts: A review,” *Environ. Chem. Lett.*, vol. 19, no. 1, pp. 355–374, 2021.

[66] D. Letchumanan, S. P. M. Sok, S. Ibrahim, N. H. Nagoor, and N. M. Arshad, “Plant-based biosynthesis of copper/copper oxide nanoparticles: An update on their applications in biomedicine, mechanisms, and toxicity,” *Biomolecules*, vol. 11, no. 4, 2021, doi: 10.3390/biom11040564.

[67] J. Hussien, A. Hymete, and J. Rohloff, “Volatile constituents and biological activities of Pycnostachys abyssinica and Pycnostachys eminii extracts,” *Pharm. Biol.*, vol. 48, no. 12, pp. 1384–1391, 2010, doi: 10.3109/13880209.2010.486406.

[68] M. Umadevi, K. P. S. Kumar, D. Bhowmik, and S. Duraivel, “Traditionally used anticancer herbs in India,” *J. Med. Plants Stud.*, vol. 1, no. 3, pp. 56–74, 2013.

[69] M. Anza, “In vitro Antioxidant and Antibacterial Activity of Root Extracts of Pycnostchyus abyssinica Fresen,” 2017. [Online]. Available: https://api.semanticscholar.org/CorpusID:249881027

[70] B. Messele, H. Lemma, M. G. Abdel-Mohsen, and T. Gebre-Mariam, “In vitro evaluation of the antimicrobial activities of selected medicinal plants,” *Ethiop. Pharm. J.*, vol. 22, no. 1, pp. 1–14, 2004.

[71] M. MEGERSA and S. WOLDETSADIK, “Ethnobotanical study of medicinal plants used by local communities of Damot Woyde District, Wolaita Zone, Southern Ethiopia,” *Nusant. Biosci.*, vol. 14, no. 1, pp. 10–24, 2022, doi: 10.13057/nusbiosci/n140102.

[72] M. M. Moliso, F. Tessema, M. Yilma, T. Getachew, and M. Asrat, “Documentation of ethno veterinary practices in selected sites of wolaita and dawuro zones, Ethiopia,” *Glob. J. Sci. Front. Res. D Agric. Vet.*, vol. 16, p. 5, 2016.

[73] S. C. Mali, A. Dhaka, S. Sharma, and R. Trivedi, “Review on biogenic synthesis of copper nanoparticles and its potential applications,” *Inorg. Chem. Commun.*, vol. 149, p. 110448, 2023.

[74] H. B. Habeeb Rahuman *et al.*, “Medicinal plants mediated the green synthesis of silver nanoparticles and their biomedical applications,” *IET nanobiotechnology*, vol. 16, no. 4, pp. 115–144, 2022.

[75] R. K. Raja *et al.*, “Green nanotechnology for the environment,” in *Handbook of Microbial Nanotechnology*, Elsevier, 2022, pp. 461–478.

[76] A. Gürses *et al.*, “Dyes and pigments: their structure and properties,” *Dye. Pigment.*, pp. 13–29, 2016.

[77] M. Roy and R. Saha, “Dyes and their removal technologies from wastewater: A critical review,” *Intell. Environ. data Monit. Pollut. Manag.*, pp. 127–160, 2021.

[78] S. S. Emmanuel, A. A. Adesibikan, O. D. Saliu, and E. A. Opatola, “Greenly biosynthesized bimetallic nanoparticles for ecofriendly degradation of notorious dye pollutants: A review,” *Plant Nano Biol.*, vol. 3, p. 100024, 2023.

[79] G. F. Aaga, W. M. Fereja, D. N. Tolcha, and A. A. Labena, “Croton macrostachyus leaf extract mediated synthesis of highly efficient ZnO NPs and ZnO/bentonite nanocomposites for photocatalytic degradation of organic dyes under solar irradiation,” *J. Environ. Chem. Eng.*, vol. 11, no. 5, Oct. 2023, doi: 10.1016/j.jece.2023.110982.

[80] K. Jain, C. Desai, O. Tiwari, and D. Madamwar, “Dyes: effect on the environment and biosphere and their remediation constraints,” *Microb. bioremediation Biodegrad.*, pp. 73–94, 2020.

[81] V. T. Tan, “Supported-metal oxide nanoparticles-potential photocatalysts,” in *Photophysics, Photochemical and Substitution Reactions-Recent Advances*, IntechOpen, 2020.

[82] Y. Deng, “Semiconducting metal oxides: Composition and sensing performance,” in *Semiconducting Metal Oxides for Gas Sensing*, Springer, 2023, pp. 105–147.

[83] P. Kumar, S. Kumar, and N. Thakur, “Azadirachta indica and polyvinylpyrrolidone encapsulated Fe2O3 nanoparticles to enhance the photocatalytic and antioxidant activity,” *Inorg. Chem. Commun.*, vol. 155, p. 111084, 2023.

[84] Samriti, V. Rajput, R. K. Gupta, and J. Prakash, “Engineering metal oxide semiconductor nanostructures for enhanced charge transfer: fundamentals and emerging SERS applications,” *Journal of Materials Chemistry C*, vol. 10, no. 1. Royal Society of Chemistry, pp. 73–95, Jan. 07, 2022. doi: 10.1039/d1tc04886d.

[85] A. R. Agustin, “Surface modification of TiO_2 nanoparticles in supercritical carbon dioxide.” 金沢大学, 2021.

[86] M. B. Gawande *et al.*, “Cu and Cu-Based Nanoparticles: Synthesis and Applications in Catalysis,” *Chemical Reviews*, vol. 116, no. 6. American Chemical Society, pp. 3722–3811, Mar. 23, 2016. doi: 10.1021/acs.chemrev.5b00482.

[87] M. Nesa, M. A. Momin, M. Sharmin, and A. H. Bhuiyan, “Structural, optical and electronic properties of CuO and Zn doped CuO: DFT based First-principles calculations,” *Chem. Phys.*, vol. 528, p. 110536, 2020.

[88] M. A. Khan, N. Nayan, Shadiullah, M. K. Ahmad, and C. F. Soon, “Surface study of cuo nanopetals by advanced nanocharacterization techniques with enhanced optical and catalytic properties,” *Nanomaterials*, vol. 10, no. 7, pp. 1–18, Jul. 2020, doi: 10.3390/nano10071298.

[89] S. Naz, A. Gul, M. Zia, and R. Javed, “Synthesis, biomedical applications, and toxicity of CuO nanoparticles,” *Applied Microbiology and Biotechnology*, vol. 107, no. 4. Springer Science and Business Media Deutschland GmbH, pp. 1039–1061, Feb. 01, 2023. doi: 10.1007/s00253-023-12364-z.

[90] P. Yadav, P. K. Dwivedi, S. Tonda, R. Boukherroub, and M. V Shelke, “Metal and non-metal doped metal oxides and sulfides,” *Green Photocatal.*, pp. 89–132, 2020.

[91] A. Winnacker, “Donors and Acceptors,” in *The Physics Behind Semiconductor Technology*, Springer, 2022, pp. 39–49.

[92] A. Alqahtani, “Engineering the Energy Gap of Cupric Oxide Nanomaterial Using Extreme Learning Machine and Stepwise Regression Algorithms,” *J. Nanomater.*, vol. 2021, 2021, doi: 10.1155/2021/4797686.

[93] R. Portela, “Non-metal doping for band-gap engineering,” in *Design of Advanced Photocatalytic Materials for Energy and Environmental Applications*, Springer, 2013, pp. 287–309.

[94] F. Irfan, M. U. Tanveer, M. A. Moiz, S. W. Husain, and M. Ramzan, “TiO2 as an effective photocatalyst mechanisms, applications, and dopants: a review,” *Eur. Phys. J. B*, vol. 95, no. 11, p. 184, 2022.

[95] W. S. Koe, J. W. Lee, W. C. Chong, Y. L. Pang, and L. C. Sim, “An overview of photocatalytic degradation: photocatalysts, mechanisms, and development of photocatalytic membrane,” *Environ. Sci. Pollut. Res.*, vol. 27, no. 3, pp. 2522–2565, 2020.

[96] E. T. Debele, T. D. Desissa, O. A. Zelekew, F. F. Bakare, G. B. Feyisa, and T. H. Wondimu, “Plant-Mediated Synthesis of Ni-Doped CuO and Fe2O3Nanocomposite for Photodegradation of Methylene Blue Dye,” *J. Nanomater.*, vol. 2023, 2023, doi: 10.1155/2023/3678679.

[97] A. Tawfik *et al.*, “Solar photo-oxidation of recalcitrant industrial wastewater: a review,” *Environ. Chem. Lett.*, vol. 20, no. 3, pp. 1839–1862, 2022.

[98] M. Náfrádi, G. Veréb, D. S. Firak, and T. Alapi, “Photocatalysis: Introduction, Mechanism, and Effective Parameters,” *Green Photocatalytic Semicond. Recent Adv. Appl.*, pp. 3–31, 2022.

[99] L. A. Ramos-Huerta, L. Laureys, A. G. Llanos, P. J. Valadés, R. S. Ruiz, and C. O. Castillo, “Assessing the effect of light intensity and light wavelength spectra on the photoreduction of formic acid using a graphene oxide material,” *Int. J. Chem. React. Eng.*, vol. 18, no. 8, p. 20200008, 2020.

[100] M. Saeed, M. Muneer, A. ul Haq, and N. Akram, “Photocatalysis: An effective tool for photodegradation of dyes—A review,” *Environ. Sci. Pollut. Res.*, vol. 29, no. 1, pp. 293–311, 2022.

[101] A. Kumar and G. Pandey, “A review on the factors affecting the photocatalytic degradation of hazardous materials,” *Mater. Sci. Eng. Int. J*, vol. 1, no. 3, pp. 1–10, 2017.

[102] W. Shi, W.-X. Fang, J.-C. Wang, X. Qiao, B. Wang, and X. Guo, “pH-controlled mechanism of photocatalytic RhB degradation over gC 3 N 4 under sunlight irradiation,” *Photochem. Photobiol. Sci.*, vol. 20, pp. 303–313, 2021.

[103] A. Das, P. Ningthoukhongjam, and R. G. Nair, “A study on the crucial reaction parameters involved in photocatalytic and sonophotocatalytic removal of organic pollutants,” *Water, Air, Soil Pollut.*, vol. 233, no. 7, p. 282, 2022.

[104] H. D. Tran, D. Q. Nguyen, P. T. Do, and U. N. P. Tran, “Kinetics of photocatalytic degradation of organic compounds: a mini-review and new approach,” *RSC Advances*, vol. 13, no. 25. Royal Society of Chemistry, pp. 16915–16925, Jun. 05, 2023. doi: 10.1039/d3ra01970e.

[105] M. A. Behnajady, N. Modirshahla, and F. Ghanbary, “A kinetic model for the decolorization of C.I. Acid Yellow 23 by Fenton process,” *J. Hazard. Mater.*, vol. 148, no. 1–2, pp. 98–102, 2007, doi: 10.1016/j.jhazmat.2007.02.003.

[106] J. P. P. Lima, C. H. B. Tabelini, M. D. N. Ramos, and A. Aguiar, “Kinetic evaluation of Bismarck Brown Y azo dye oxidation by Fenton processes in the presence of aromatic mediators,” *Water, Air, Soil Pollut.*, vol. 232, no. 8, p. 321, 2021.

[107] H.-Y. Xu, Y. Li, W.-S. Wang, X.-J. Li, and L.-M. Dong, “Magnetic nanoscale

MnFe2O4 as heterogeneous Fenton-like catalyst for rhodamine B degradation: efficiency, kinetics and process optimization," *J. Iran. Chem. Soc.*, vol. 20, no. 8, pp. 2043–2055, 2023.

[108] U. Wijesinghe, G. Thiripuranathar, F. Menaa, H. Iqbal, A. Razzaq, and H. Almukhlifi, "Green synthesis, structural characterization and photocatalytic applications of ZnO nanoconjugates using Heliotropium indicum," *Catalysts*, vol. 11, no. 7, 2021, doi: 10.3390/catal11070831.

[109] E. Takele, R. Feyisa Bogale, G. Shumi, and G. Kenasa, "Green Synthesis, Characterization, and Antibacterial Activity of CuO/ZnO Nanocomposite Using Zingiber officinale Rhizome Extract," *J. Chem.*, vol. 2023, 2023, doi: 10.1155/2023/3481389.

[110] W. W. Andualem, F. K. Sabir, E. T. Mohammed, H. H. Belay, and B. A. Gonfa, "Synthesis of copper oxide nanoparticles using plant leaf extract of catha edulis and its antibacterial activity," *J. Nanotechnol.*, vol. 2020, 2020, doi: 10.1155/2020/2932434.

[111] D. S. Vasanthi, K. Ravichandran, P. Kavitha, S. Sriram, and P. K. Praseetha, "Combined effect of Cu and N on bandgap modification of ZnO film towards effective visible light responsive photocatalytic dye degradation," *Superlattices Microstruct.*, vol. 145, Sep. 2020, doi: 10.1016/j.spmi.2020.106637.

[112] L. Yadeta Gemachu and A. Lealem Birhanu, "Green synthesis of ZnO, CuO and NiO nanoparticles using Neem leaf extract and comparing their photocatalytic activity under solar irradiation," *Green Chem. Lett. Rev.*, vol. 17, no. 1, p. 2293841, 2024.

[113] S. K. Karuppannan, R. Ramalingam, S. B. Mohamed Khalith, M. J. H. Dowlath, G. I. Darul Raiyaan, and K. D. Arunachalam, "Characterization, antibacterial and photocatalytic evaluation of green synthesized copper oxide nanoparticles," *Biocatal. Agric. Biotechnol.*, vol. 31, no. September 2020, 2021, doi: 10.1016/j.bcab.2020.101904.

[114] M. Narayanan, F. ahamed J. hussain, B. Srinivasan, M. T. Sambantham, L. A. Al-Keridis, and F. A. AL-mekhlafi, "Green synthesizes and characterization of copper-oxide nanoparticles by Thespesia populnea against skin-infection causing microbes," *J. King Saud Univ. - Sci.*, vol. 34, no. 3, p. 101885, 2022, doi:

10.1016/j.jksus.2022.101885.

[115] S. A. Akintelu, A. S. Folorunso, F. A. Folorunso, and A. K. Oyebamiji, “Green synthesis of copper oxide nanoparticles for biomedical application and environmental remediation,” *Heliyon*, vol. 6, no. 7, p. e04508, 2020, doi: 10.1016/j.heliyon.2020.e04508.

[116] K. R. Reddy, “Green synthesis, morphological and optical studies of CuO nanoparticles,” *J. Mol. Struct.*, vol. 1150, pp. 553–557, 2017.

[117] A. Pramothkumar, N. Senthilkumar, R. M. Jenila, M. Durairaj, T. C. S. Girisun, and I. V. Potheher, “A study on the electrical, magnetic and optical limiting behaviour of Pure and Cd-Fe co-doped CuO NPs,” *J. Alloys Compd.*, vol. 878, p. 160332, 2021, doi: 10.1016/j.jallcom.2021.160332.

[118] J. Tauc, “Optical properties and electronic structure of amorphous Ge and Si,” *Mater. Res. Bull.*, vol. 3, no. 1, pp. 37–46, 1968.

[119] Y. Dessie and S. Tadesse, “Optimization of polyvinyl alcohol binder on PANI coated pencil graphite electrode in doubled chamber microbial fuel cell for glucose biosensor,” *Sens. Bio-Sensing Res.*, vol. 36, p. 100484, 2022, doi: 10.1016/j.sbsr.2022.100484.

[120] J. Iqbal *et al.*, “Facile synthesis of Zn doped CuO hierarchical nanostructures: Structural, optical and antibacterial properties,” *AIP Adv.*, vol. 5, no. 12, Dec. 2015, doi: 10.1063/1.4937907.

[121] H. Veisi, B. Karmakar, T. Tamoradi, S. Hemmati, M. Hekmati, and M. Hamelian, “Biosynthesis of CuO nanoparticles using aqueous extract of herbal tea (Stachys Lavandulifolia) flowers and evaluation of its catalytic activity,” *Sci. Rep.*, vol. 11, no. 1, pp. 1–13, 2021, doi: 10.1038/s41598-021-81320-6.

[122] A. G. Bekru, O. A. Zelekew, D. M. Andoshe, F. K. Sabir, and R. Eswaramoorthy, “Microwave-assisted synthesis of CuO nanoparticles using cordia africana Lam. leaf extract for 4-nitrophenol reduction,” *J. Nanotechnol.*, vol. 2021, 2021, doi: 10.1155/2021/5581621.

[123] Y.-K. Phang *et al.*, “Green synthesis and characterization of CuO nanoparticles derived from papaya peel extract for the photocatalytic degradation of palm oil mill effluent (POME),” *Sustainability*, vol. 13, no. 2, p. 796, 2021.

[124] S. M. Yakout and A. M. El-Sayed, “Structural, Morphological and Ferromagnetic Properties of Pure and (Mn, Co) Codoped CuO Nanostructures,” *J. Supercond. Nov. Magn.*, vol. 29, no. 11, pp. 2961–2968, 2016, doi: 10.1007/s10948-016-3641-9.

[125] R. M. Adnan, M. Mezher, A. M. Abdallah, R. Awad, and M. I. Khalil, “Synthesis, Characterization, and Antibacterial Activity of Mg-Doped CuO Nanoparticles,” *Molecules*, vol. 28, no. 1, Jan. 2023, doi: 10.3390/molecules28010103.

[126] M. J. Ferdous Anik, S. R. Mim, S. S. Swapno, S. Munira, O. Roy, and M. M. Billah, “Vacancy induced enhanced photocatalytic activity of nitrogen doped CuO NPs synthesized by Co-precipitation method,” *Heliyon*, vol. 10, no. 6, p. e27613, 2024, doi: 10.1016/j.heliyon.2024.e27613.

[127] R. O. Yathisha and Y. Arthoba Nayaka, “Structural, optical and electrical properties of zinc incorporated copper oxide nanoparticles: doping effect of Zn,” *J. Mater. Sci.*, vol. 53, no. 1, pp. 678–691, 2018, doi: 10.1007/s10853-017-1496-5.

[128] M. Y. El Sayed, N. El Ghouch, G. O. Younes, and R. Awad, “Influence of Zn doping on the structural, optical, and magnetic properties of CuO nanoparticles and evaluation of its anti-corrosive behavior of mild steel in acidic medium,” *J. Bio-and Tribo-Corrosion*, vol. 8, no. 4, p. 95, 2022.

[129] A. Pramothkumar, N. Senthilkumar, K. C. Mercy Gnana Malar, M. Meena, and I. Vetha Potheher, “A comparative analysis on the dye degradation efficiency of pure, Co, Ni and Mn-doped CuO nanoparticles,” *J. Mater. Sci. Mater. Electron.*, vol. 30, no. 20, pp. 19043–19059, 2019, doi: 10.1007/s10854-019-02262-4.

[130] N. Thakur, K. Kumar, and A. Kumar, “Effect of (Ag, Zn) co-doping on structural, optical and bactericidal properties of CuO nanoparticles synthesized by a microwave-assisted method,” *Dalt. Trans.*, vol. 50, no. 18, pp. 6188–6203, 2021.

[131] A. L. Patterson, “The Scherrer formula for X-ray particle size determination,” *Phys. Rev.*, vol. 56, no. 10, p. 978, 1939.

[132] A. Albert manoharan *et al.*, “Facile synthesis and characterization of undoped, Mn doped and Nd co-doped CuO nanoparticles for optoelectronic and magnetic applications,” *J. Mol. Struct.*, vol. 1171, pp. 388–395, 2018, doi: 10.1016/j.molstruc.2018.06.018.

[133] A. M. El Sayed and M. Shaban, “Structural, optical and photocatalytic properties of

Fe and (Co, Fe) co-doped copper oxide spin coated films," *Spectrochim. Acta - Part A Mol. Biomol. Spectrosc.*, vol. 149, pp. 638–646, 2015, doi: 10.1016/j.saa.2015.05.010.

[134] F. Mohamed, S. Hassaballa, M. Shaban, and A. M. Ahmed, "Highly Efficient Photocatalyst Fabricated from the Chemical Recycling of Iron Waste and Natural Zeolite for Super Dye Degradation," *Nanomaterials*, vol. 12, no. 2, Jan. 2022, doi: 10.3390/nano12020235.

[135] D. M. Nzilu, E. S. Madivoli, D. S. Makhanu, S. I. Wanakai, G. K. Kiprono, and P. G. Kareru, "Green synthesis of copper oxide nanoparticles and its efficiency in degradation of rifampicin antibiotic," *Sci. Rep.*, vol. 13, no. 1, pp. 1–18, 2023, doi: 10.1038/s41598-023-41119-z.

[136] T. Welderfael, O. P. Yadav, A. M. Taddesse, and J. Kaushal, "Synthesis, characterization and photocatalytic activities of Ag-N-Codoped ZnO nanoparticles for degradation of methyl red," *Bull. Chem. Soc. Ethiop.*, vol. 27, no. 2, pp. 221–232, 2013, doi: 10.4314/bcse.v27i2.7.

[137] C. S. Santana, M. D. N. Ramos, C. C. V. Velloso, and A. Aguiar, "Kinetic evaluation of dye decolorization by fenton processes in the presence of 3-hydroxyanthranilic acid," *Int. J. Environ. Res. Public Health*, vol. 16, no. 9, 2019, doi: 10.3390/ijerph16091602.

[138] H.-Y. Xu, T.-N. Shi, L.-C. Wu, and S.-Y. Qi, "Discoloration of methyl orange in the presence of schorl and H 2 O 2: kinetics and mechanism," *Water, Air, Soil Pollut.*, vol. 224, pp. 1–11, 2013.

[139] P. M. Y. Ansari, R. M. Muthukrishnan, R. I. Khan, C. Vedhi, K. Sakthipandi, and S. M. A. Kader, "Green synthesis of copper oxide nanoparticles using Amaranthus dubius leaf extract for sensor and photocatalytic applications," *Chem. Phys. Impact*, vol. 7, p. 100374, 2023.

[140] J. Iqbal *et al.*, "Facile synthesis of Zn doped CuO hierarchical nanostructures: Structural, optical and antibacterial properties," *Aip Adv.*, vol. 5, no. 12, 2015.

[141] D. B. Manikandan *et al.*, "Biofabrication of ecofriendly copper oxide nanoparticles using Ocimum americanum aqueous leaf extract: analysis of in vitro antibacterial, anticancer, and photocatalytic activities," *Environ. Sci. Pollut. Res.*, vol. 28, no. 26,

pp. 33927–33941, 2021, doi: 10.1007/s11356-020-12108-w.

[142] P. Mohammed Yusuf Ansari, R. M. Muthukrishnan, R. Imran Khan, C. Vedhi, K. Sakthipandi, and S. M. Abdul Kader, “Green synthesis of copper oxide nanoparticles using Amaranthus dubius leaf extract for sensor and photocatalytic applications,” *Chem. Phys. Impact*, vol. 7, no. October, p. 100374, 2023, doi: 10.1016/j.chphi.2023.100374.

[143] L. Vimala Devi *et al.*, “Synthesis, defect characterization and photocatalytic degradation efficiency of Tb doped CuO nanoparticles,” *Adv. Powder Technol.*, vol. 28, no. 11, pp. 3026–3038, 2017, doi: 10.1016/j.apt.2017.09.013.

APPENDICES

Appendix 1: Optimization of dopant concentration

Photocatalytic degradation of Methylene Blue with 80 mg of photocatalyst, 5 ppm initial conc. of MB, pH 11, $A_0 = 0.637$, and exposure time to sunlight = 1 hr

Conc. of dopants (% w/w)	**Trials**	**N-CuO NPs**	**Zn-CuO NPs**
		Abs (A_t)	**Abs (A_t)**
1%	1	0.038	0.017
	2	0.037	0.016
	3	0.039	0.018
	A_{av}	0.038	0.017
	%D	94.6% $\pm$0.001	97.5%$\pm$0.001
3%	1	0.013	0.017
	2	0.012	0.017
	3	0.008	0.015
	A_{av}	0.011	0.016
	%D	**98.4% $\pm$0.00265**	**97.7%$\pm$0.00115**
6%	1	0.033	0.054
	2	0.035	0.052
	3	0.039	0.048
	A_{av}	0.036	0.051
	%D	94.8% $\pm$0.00306	92.6%$\pm$0.00306
10%	1	0.034	0.039
	2	0.038	0.038
	3	0.031	0.033
	A_{av}	0.034	0.037
	%D	95.1% $\pm$0.00351	94.6%$\pm$0.00321

%D = percent of photocatalytic degradation efficiency

The values are the triplicate means of the degradation efficiency ± standard deviation.

Appendix 2: Effect of pH

Photocatalytic degradation of MB with 5 ppm initial conc. MB, 80 mg of nano photocatalyst, A_0 = 0.637 and exposure time = 1 hr

pH	Trials	Pure CuO NPs	N-CuO NPs	Zn-CuO NPs	N-Zn-CuO NPs
		Abs	Abs	Abs	Abs
2	1	0.570	0.555	0.523	0.478
	2	0.567	0.563	0.527	0.478
	3	0.576	0.557	0.518	0.480
	A_{av}	0.571	0.558	0.523	0.477
	%D*	10.36%±0.00458	12.40%±0.0041	17.9%±0.0045	25.1%±0.00115
3	1	0.530	0.513	0.476	0.426
	2	0.531	0.514	0.475	0.424
	3	0.531	0.513	0.475	0.4245
	A_{av}	0.531	0.513	0.475	0.4245
	%D	16.55%±0.00057	19.47%±0.0005	25.29%±0.055	33.35%±0.0011
4	1	0.489	0.462	0.432	0.372
	2	0.489	0.465	0.430	0.372
	3	0.488	0.463	0.431	0.371
	A_{av}	0.489	0.464	0.431	0.372
	%D	23.24%±0.00057	27.12%±0.0047	32.2%±0.001	41.56%±0.0057
5	1	0.445	0.421	0.383	0.326
	2	0.446	0.417	0.380	0.326
	3	0.446	0.416	0.384	0.327
	A_{av}	0.445	0.419	0.382	0.326
	%D	30.01%±0.00057	34.15%±0.0026	39.89%±0.002	48.74%±0.0057
6	1	0.397	0.366	0.338	0.269
	2	0.399	0.365	0.335	0.271
	3	0.398	0.365	0.340	0.267
	A_{av}	0.399	0.365	0.338	0.269
	%D	37.29%±0.001	42.59%±0.0005	46.83%±0.002	57.63%±0.002
7	1	0.345	0.307	0.281	0.220
	2	0.343	0.306	0.282	0.218
	3	0.345	0.305	0.281	0.218
	A_{av}	0.344	0.306	0.281	0.219
	%D	45.92%±0.00115	51.94%±0.001	55.84%±0.0005	65.51%±0.0011
8	1	0.288	0.251	0.159	0.161
	2	0.289	0.250	0.160	0.162
	3	0.288	0.252	0.162	0.160
	A_{av}	0.288	0.250	0.161	0.161
	%D	54.75%±0.00057	60.66%±0.001	64.86%±0.0015	74.64%±0.001
9	1	0.221	0.184	0.161	0.108
	2	0.220	0.181	0.162	0.107
	3	0.222	0.179	0.160	0.105
	A_{av}	0.221	0.181	0.161	0.107
	%D	65.18%±0.001	71.44%±0.0025	74.71%±0.001	83.05%±0.0015

10	1	0.153	0.122	0.102	0.049
	2	0.153	0.121	0.102	0.047
	3	0.155	0.120	0.101	0.048
	A_{av}	0.153	0.121	0.102	0.048
	%D	75.84%±0.00115	80.95%±0.001	83.96%±0.0005	92.56%±0.001
11	1	0.097	0.062	0.049	0.019
	2	0.098	0.063	0.048	0.016
	3	0.096	0.062	0.050	0.019
	A_{av}	0.097	0.062	0.049	0.018
	%D	84.64%±0.001	90.17%±0.0005	92.27%±0.0015	97.06%±0.0017
12	1	0.055	0.069	0.035	0.026
	2	0.055	0.067	0.034	0.025
	3	0.058	0.070	0.036	0.026
	A_{av}	0.056	0.069	0.036	0.026
	%D	91.19%±0.00173	89.06%±0.0015	94.27%±0.001	95.81%±0.0005
13	1	0.093	0.106	0.081	0.065
	2	0.092	0.106	0.082	0.065
	3	0.092	0.106	0.080	0.069
	A_{av}	0.092	0.106	0.081	0.066
	%D	85.43%±0.00057	83.21%±0.001	87.21%±0.001	89.57%±0.0023
14	1	0.138	0.159	0.123	0.113
	2	0.137	0.158	0.123	0.113
	3	0.135	0.158	0.125	0.114
	A_{av}	0.137	0.158	0.124	0.113
	%D	78.39%±0.00152	75.13%±0.0057	80.49%±0.0011	82.22%±0.0005

%D = percent of photocatalytic degradation efficiency

The values are the triplicate means of the degradation efficiency ± standard deviation.

Appendix 3: Effect of photocatalytic dosage

Photocatalytic degradation of MB with 5 ppm initial conc. MB, with an optimized pH of 11 for pure N-CuO NPs and N-Zn-CuO NPs and 12 for pure CuO NPs and Zn-CuO NPs; A_0 = 0.637, and exposure time = 1 hr

Photo-catalyst dosage (mg)	**Trials**	**p-CuO NPs**	**N-CuO NPs**	**Zn-CuO NPs**	**N-Zn-CuO NPs**
		Absorbance ($A_{t = 1hr}$)	**Absorbance ($A_{t = 1hr}$)**	**Absorbance ($A_{t =1 hr}$)**	**Absorbance ($A_{t =1 hr}$)**
10	**1**	0.044	0.036	0.029	0.022
	2	0.048	0.037	0.031	0.020
	3	0.046	0.036	0.027	0.021
	A_{av}	0.046	0.036	0.029	0.020
	%D	92.76%±0.002	94.31%±0.00057	95.32%±0.00057	96.84%±0.001
40	**1**	0.034	0.027	0.020	0.011
	2	0.034	0.025	0.021	0.013
	3	0.030	0.025	0.021	0.009
	A_{av}	0.033	0.026	0.020	0.011
	%D	94.72%±0.002	95.81%±0.00011	96.74%±0.00057	98.21%±0.002
80	**1**	0.023	0.016	0.011	0.004
	2	0.023	0.015	0.010	0.004
	3	0.024	0.017	0.012	0.003
	A_{av}	0.023	0.016	0.011	0.004
	%D	93.88%±0.0005	97.47%±0.0021	98.33%±0.00112	99.36%±0.0005
120	**1**	0.014	0.005	0.002	0.0001
	2	0.013	0.006	0.003	0.0001
	3	0.012	0.006	0.002	0.0001
	A_{av}	0.013	0.006	0.002	0.0001
	%D	97.83%±0.001	98.92%±0.00057	**99.57%±0.0005**	**99.97%±0.0001**
160	**1**	0.003	0.002	0.006	0.004
	2	0.003	0.001	0.006	0.005
	3	0.004	0.001	0.005	0.004
	A_{av}	0.003	0.001	0.006	0.004
	%D	**99.47%±0.0005**	**99.84%±0.0005**	98.94%±0.0005	99.29%±0.0005
200	1	0.007	0.007	0.012	0.01
	2	0.010	0.007	0.013	0.02
	3	0.009	0.006	0.014	0.01
	A_{av}	0.009	0.007	0.013	0.01
	%D	98.55%±0.0015	98.86%±0.00057	97.92%±0.001	98.32%±0.0057

The values are the triplicate means of the degradation efficiency ± standard deviation.

Appendix 4: Effect of initial concentration of MB

Photocatalytic degradation of Methylene Blue at an optimal photocatalyst dosage of 160 mg for the pure CuO NPs and N-CuO NPs and 120 mg for the Zn-CuO NPs and N-Zn-CuO NPs and at an optimal pH of 11 for the N-CuO NPs and N-Zn-CuO NPs and at a pH of 12 for the pure CuO NPs & Zn-CuO NPs, respectively, with an exposure time of 1hr.

Initial conc. of MB (ppm)	**A_0**	**Trials**	**Pure CuO NPs**	**N-CuO NPs**	**Zn-CuO NPs**	**N-Zn-CuO NPs**
			Absorbance ($A_{t = 1hr}$)	**Absorbance ($A_{t = 1hr}$)**	**Absorbance ($A_{t = 1hr}$)**	**Absorbance ($A_{t = 1hr}$)**
1	0.034	1	0.0001	0.0002	0.00002	0.00001
		2	0.0002	0.0001	0.000201	0.00001
		3	0.0002	0.0001	0.00002	0.00001
		A_{av}	0.0002	0.0002	0.000201	0.00002
		%D	99.24%±0.0005	99.37%±0.000	99.41%±0.000	99.92%±0.0005
5	0.637	1	0.006	0.004	0.005	0.001
		2	0.005	0.003	0.003	0.001
		3	0.005	0.005	0.003	0.002
		A_{av}	0.006	0.005	0.004	0.001
		%D	99.11%±0.0015	99.21%±0.005	99.29%±0.001	99.71%±0.005
10	1.106	1	0.011	0.010	0.009	0.005
		2	0.009	0.008	0.008	0.007
		3	0.010	0.008	0.009	0.006
		A_{av}	0.010	0.009	0.009	0.006
		%D	99.07%±0.0043	99.13%±0.003	99.18%±0.001	99.42%±0.003
15	1.761	1	0.016	0.017	0.013	0.011
		2	0.018	0.016	0.018	0.013
		3	0.017	0.016	0.016	0.013
		A_{av}	0.017	0.016	0.015	0.012
		%D	99.03±0.0058	99.05%±0.003	99.11%±0.004	99.29%±0.001
20	2.230	1	0.027	0.025	0.023	0.019
		2	0.016	0.026	0.025	0.018
		3	0.026	0.023	0.023	0.017
		A_{av}	0.027	0.025	0.024	0.019
		%D	98.79%±0.003	98.86%±0.005	98.92%±0.002	99.14%±0.005
25	2.692	1	0.126	0.102	0.100	0.049
		2	0.129	0.100	0.103	0.046
		3	0.128	0.101	0.101	0.045
		A_{av}	0.128	0.102	0.101	0.047
		%D	95.23%±0.0058	96.19%±0.001	96.23%±0.005	98.23%±0.001
30	3.025	1	0.268	0.223	0.223	0.186
		2	0.267	0.228	0.223	0.187
		3	0.267	0.226	0.234	0.187
		A_{av}	0.268	0.225	0.223	0.185
		%D	91.11%±0.001	92.54%±0.005	92.61%±0.001	93.86%±0.001

Appendix 5: Effect of reaction time

To investigate the effect of reaction time on both dark reactions (stirring time in a dark room) and light reactions (exposure to direct sunlight) and to determine the optimal reaction time required for the complete photocatalytic degradation of methylene blue (MB) using biosynthesized pure CuO NPs, N-CuO NPs, Zn-CuO NPs, and N-Zn-CuO NPs, 5 mL aliquots of the reaction mixture were withdrawn at 10-minute intervals during both the adsorption reaction in the dark and the photocatalysis reaction in sunlight. All other photocatalytic parameters were held constant at the determined optimal values for each photocatalyst, as listed in the appendices above. The observed data were recorded and calculated as follows.

Nanocatalyst			**Pure CuO NPs**	**N-CuO NPs**	**Zn-CuO NPs**	**N-Zn-CuO NPs**
Optimized Parameters			pH = 12, dose* = 160 mg, [MB] = 20 ppm, A_0 = 2.230	pH = 11, dose = 160 mg, [MB] = 20 ppm, A_0 = 2.230	pH = 12, dose = 120 mg, [MB] = 20 ppm, A_0 = 2.230	pH = 11, dose = 120 mg, [MB] = 20 ppm, A_0 = 2.230
Exposure time (min)		**Trial**	**Absorbance at time t. (A_t)**	**Absorbance at time t. (A_t)**	**Absorbance at time t. (A_t)**	**Absorbance at time t. (A_t)**
Dark reaction (adsorption process)	**-20'**	1	1.999	1.94	1.907	1.824
		2	1.997	1.938	1.910	1.823
		3	1.999	1.938	1.911	1.820
		A_{av}	1.999	1.938	1.909	1.822
		%D	10.35±0.00115	13.18%±0.00115	14.38±0.002081	18.29±0.002081
	-10'	1	1.741	1.642	1.589	1.485
		2	1.741	1.642	1.591	1.486
		3	1.743	1.648	1.592	1.487
		A_{av}	1.742	1.644	1.590	1.486
		%D	21.89±0.00115	26.27%±0.00346	28.68±0.001527	33.32±0.001
	0'	1	1.473	1.384	1.312	1.205
		2	1.475	1.388	1.313	1.204
		3	1.471	1.394	1.313	1.205
		A_{av}	1.473	1.388	1.313	1.205
		%D	33.94±0.002	37.76%±0.00503	41.12±0.000577	45.95±0.000577
Light reaction	**10'**	1	0.816	0.7	0.661	0.529
		2	0.818	0.7	0.660	0.528
		3	0.819	0.702	0.661	0.526
		A_{av}	0.817	0.7	0.661	0.528
		%D	63.35%±0.00152	68.60%±0.00115	70.38%±0.00057	76.29%±0.00152
	20'	1	0.424	0.338	0.274	0.193
		2	0.426	0.334	0.274	0.193
		3	0.426	0.338	0.274	0.194
		A_{av}	0.426	0.338	0.274	0.193
		%D	97.89%±0.00115	84.84%±0.00231	87.68%±0.00001	91.32%±0.00057

Nanocatalyst			**Pure CuO NPs**	**N-CuO NPs**	**Zn-CuO NPs**	**N-Zn-CuO NPs**
Optimized Parameters			pH = 12, NCD = 160 mg, 20 ppm, A_0 = 2.230	pH = 11, NCD = 160 mg, 10 ppm, A_0 = 1.106	pH = 12, NCD = 120 mg, 20 ppm, A_0 = 2.230	pH = 11, NCD = 120 mg, 20 ppm, A_0 = 2.230
Exposure time (min)		**Trial**	**Absorbance at time t. (A_t)**	**Absorbance at time t. (A_t)**	**Absorbance at time t. (A_t)**	**Absorbance at time t. (A_t)**
Light reaction (photocatalysis process)	**30'**	1	0.094	0.046	0.038	0.004
		2	0.093	0.046	0.039	0.005
		3	0.095	0.044	0.038	0.005
		A_{av}	0.094	0.046	0.038	0.005
		%D	95.76%±0.001	97.93%±0.00115	98.26%±0.00577	99.75%±0.00577
	40'	1	0.08	0.042	0.033	0.0053
		2	0.081	0.044	0.033	0.0052
		3	0.081	0.042	0.032	0.0053
		A_{av}	0.080	0.042	0.033	0.0053
		%D	96.38%±0.00577	98.11%±0.00115	98.51%±0.00577	99.76%±0.00005
	50'	1	0.055	0.032	0.006	0.0051
		2	0.058	0.03	0.006	0.0051
		3	0.058	0.03	0.005	0.0052
		A_{av}	0.057	0.03	0.006	0.0051
		%D	97.41%±0.00173	98.65%±0.00115	99.73%±0.00057	99.77%±0.00005
	60'	1	0.042	0.016	0.0051	0.004
		2	0.043	0.016	0.0051	0.004
		3	0.042	0.014	0.0052	0.004
		A_{av}	0.043	0.016	0.0051	0.004
		%D	98.06%±0.00057	99.28%±0.00057	99.77%±0.00005	99.82%±0.00001

The values are the triplicate means of the degradation efficiency ± standard deviation.

Appendix 6: Calibration Curve Data

Initial conc. of MB (ppm)	Triplicate	Abs (A_0)	Average Absorbance (Av A_0)	Standard deviation (SD)
1	1	0.032	0.034	±0.00179
	2	0.036		
	3	0.035		
5	1	0.638	0.637	±0.00208
	2	0.635		
	3	0.639		
10	1	1.107	1.106	±0.0058
	2	1.106		
	3	1.106		
15	1	1.762	1.761	±0.00173
	2	1.762		
	3	1.759		
20	1	2.231	2.230	±0.00153
	2	2.229		
	3	2.232		
25	1	2.695	2.692	±0.00306
	2	2.691		
	3	2.689		
30	1	3.025	3.025	±0.0058
	2	3.026		
	3	3.025		
Molar absorptivity ε = Slope/l = 0.1035 M^{-1} cm^{-1}			**0.1035 M^{-1} cm^{-1}**	
At/εl			**Ct**	

The values are presented as the triplicate mean of the initial concentration ± standard deviation of the absorbance.

Appendix 7: Kinetic data

To investigate the photocatalytic degradation rate of MB dye on the surface of the biosynthesized pure CuO NPs, N-CuO NPs, Zn-CuO NPs, and N-Zn-CuO NPs under sunlight, the kinetic data presented in Appendix 7 were analysed based on the observed experimental data and plotted according to pseudo-zero-order, pseudo-first-order, pseudo-second-order, and BMG kinetic models.

Kinetics study Models					**Zero-Order**		**First-Order**	**Second -Order**	**BMG Model**
Nano catalyst	Time (t) (min)	Abs at time t. (A_t)	C_0 (ppm)	C_t (ppm)	$C_o - C_t$	$\frac{C_0}{C_t}$	$\ln\frac{C_0}{C_t}$	$\frac{1}{C_t} - \frac{1}{C_0}$	$\frac{t}{1-\frac{C_t}{C_0}}$
Pure CuO NPs	10	0.059	20	0.570	19.430	35.085	3.558	1.704	10.293
	20	0.047	20	0.454	19.546	44.042	3.785	2.152	20.465
	30	0.041	20	0.396	19.604	50.488	3.922	2.474	30.606
	40	0.036	20	0.348	19.652	57.500	4.052	2.825	40.708
	50	0.022	20	0.212	19.787	94.091	4.544	4.654	50.537
	60	0.021	20	0.203	19.797	98.571	4.591	4.878	60.615
N-CuO NPs	10	0.712	20	6.879	13.120	2.907	1.067	0.095	15.243
	20	0.3381	20	3.266	16.733	6.122	1.812	0.256	23.904
	30	0.046	20	0.444	19.555	45.000	3.806	2.200	30.682
	40	0.042	20	0.406	19.594	49.286	3.897	2.414	40.828
	50	0.031	20	0.299	19.700	66.774	4.201	3.2887	50.760
	60	0.016	20	0.154	19.845	129.375	4.863	6.418	60.467
Zn-CuO NPs	10	0.038	20	0.367	19.633	54.474	3.997	2.674	10.187
	20	0.03	20	0.289	19.710	69.000	4.234	3.400	20.294
	30	0.021	20	0.203	19.797	98.571	4.590	4.878	30.307
	40	0.011	20	0.106	19.894	188.18	5.237	9.359	40.214
	50	0.006	20	0.058	19.942	345.00	5.843	17.200	50.145
	60	0.005	20	0.048	19.952	414	6.0258	20.65	60.145
N-Zn CuO NPs	10	0.027	20	0.261	19.739	76.666	4.3395	3.7833	10.132
	20	0.015	20	0.145	19.855	138	4.9272	6.85	20.146
	30	0.012	20	0.116	19.884	172.5	5.1504	8.575	30.175
	40	0.01	20	0.097	19.903	207	5.3327	10.3	40.194
	50	0.005	20	0.048	19.952	414	6.0258	20.65	50.121
	60	0.004	20	0.039	19.961	517.5	6.2490	25.825	60.116

Appendix 8: Nanocatalyst Reusability

Reusability of all the biosynthesized nanocatalysts for the photocatalytic degradation of MB under optimum conditions

Nanocatalyst		**Pure CuO NPs**	**N-CuO NPs**	**Zn-CuO NPs**	**N-Zn-CuO NPs**
Optimized Parameters		pH = 12, NCD = 160 mg, 20 ppm, A_0 = 2.230	pH = 11, NCD = 160 mg, 20 ppm, A_0 = 2.230	pH = 12, NCD = 120 mg, 20 ppm, A_0 = 2.230	pH = 11, NCD = 120 mg, 20 ppm, A_0 = 2.230
Number of cycles	**Trials**	**Abs ($A_{t=30\ min}$)**	**Abs ($A_{t=30\ min}$)**	**Abs ($A_{t=30\ min}$)**	**Abs ($A_{t=30\ min}$)**
First	1	0.094	0.023	0.039	0.005
	2	0.094	0.024	0.039	0.005
	3	0.095	0.025	0.036	0.004
	A_{av}	0.094	0.0234	0.038	0.005
	%D	95.76±0.000577	97.88±0.001	98.26±0.00173	99.75±0.000577
Second	1	0.123	0.035	0.065	0.031
	2	0.122	0.038	0.066	0.030
	3	0.124	0.039	0.063	0.028
	A_{av}	0.124	0.037	0.064	0.030
	%D	94.41±0.0001	96.58±0.020816	97.11±0.001528	98.62±0.001528
Third	1	0.172	0.050	0.088	0.058
	2	0.170	0.052	0.089	0.059
	3	0.169	0.051	0.086	0.057
	A_{av}	0.170	0.052	0.088	0.058
	%D	92.35±0.001527	95.25±0.0001	96.01±0.001528	97.36±0.0001
Fourth	1	0.223	0.072	0.113	0.093
	2	0.220	0.074	0.115	0.093
	3	0.220	0.071	0.115	0.093
	A_{av}	0.221	0.072	0.115	0.092
	%D	90.09±0.001732	93.43±0.001527	94.83±0.001155	95.82±0.000577

The values are the triplicate means of the degradation efficiency ± standard deviation.

Appendix 9: Supplementary information from laboratory sessions

Biosynthesis of CuO NPs

Mixture of copper and PA extracts After 2 hr CuO NPs as synthesized

w/w% of Zn and N added to CuO NPs Calcination Biosynthesized NPs

Stirring for 30 min at dark reaction

After 30 min, 5 ml mixture of the solution withdrawer by test tube exposure to sunlight

Absorbance after photocatalytic degradation was measured